Elemental Composition of Surface Sediment as a Sea/Land-Level Indicator in Cascadia Salt Marshes

by

Anthony Giang

B.Sc., Simon Fraser University, 2021

Thesis Submitted in Partial Fulfillment of the
Requirements for the Degree of
Master of Science

in the
Department of Earth Sciences
Faculty of Science

© Anthony Giang 2023
SIMON FRASER UNIVERSITY
Fall 2023

Copyright in this work is held by the author. Please ensure that any reproduction or re-use is done in accordance with the relevant national copyright legislation.

Declaration of Committee

Name:	**Anthony Giang**
Degree:	**Master of Science**
Title:	**Elemental Composition of Surface Sediment as a Sea/Land-Level Indicator in Cascadia Salt Marshes**
Committee:	**Chair:** **Dan Gibson** Professor, Earth Sciences **Jessica Pilarczyk** Supervisor Associate Professor, Earth Sciences **John Clague** Committee Member Professor Emeritus, Earth Sciences **David Huntley** Committee Member Adjunct Professor, Earth Sciences **Daria Nikitina** Examiner Associate Professor, Geology and Astronomy West Chester University

Abstract

This thesis explores the utility of elemental geochemistry obtained through x-ray fluorescence as a sea-level indicator. Elemental data of modern salt marsh sediment from Port Alberni, British Columbia and Willapa Bay, Washington reveal consistent relationships between elemental composition and tidal elevation. Lithogenic (Si, K, Ti, Fe) and biogenic (Sr) elements are most abundant at low elevations where clastic deposition dominates, while organic proxies (Br, incoherent coherent scattering ratio) are most prevalent at high elevations where marsh vegetation is well established. Cluster analysis shows that the vertical zonation patterns of elements within the salt marshes agree with previously determined foraminifera and diatom distributions at Port Alberni and Willapa Bay. This project establishes the first modern elemental training set relating elemental composition to tidal elevation and highlights the applications of elemental geochemistry as a new sea-level indicator.

Keywords: Cascadia; elemental geochemistry; sea-level indicator; x-ray fluorescence; sea-level change

Dedication

To my father, Cuong Giang (江永基)

Acknowledgements

I am extremely grateful to my supervisor Jessica Pilarczyk for all the opportunities I have been given and for all her guidance and support. Her encouragements and insights helped instill faith and confidence in my work.

Thank you to my committee members John Clague and David Huntley for their commitment to my project and for their discussions and ideas that undoubtably improved my thesis.

Thank you to the SFU Earth Sciences Department for supporting me through this program. I am grateful for Matt Plotnikoff, Elilan Ganesathas, Alyssa Hamilton-Messenger, Lorena Munoz, and Gwenn Flowers for all their help behind the scenes navigating the program.

Thank you to everyone in the Coastal Hazard Research Lab for being a part of a warm and welcoming work environment. I am especially grateful for my academic twin Louise Riou for being the most authentic and honest person I could have gone through graduate school with.

Thank you to all my friends and family for their ongoing and seemingly unknowing support.

Table of Contents

Declaration of Committee ii
Abstract iii
Dedication iv
Acknowledgements v
Table of Contents vi
List of Tables viii
List of Figures ix
List of Acronyms xii
Preface xiii

Chapter 1. Background 1
1.1. Introduction 1
1.2. Cascadia Subduction Zone 2
1.2.1. Recognizing Past Earthquakes in the Geologic Record 2
1.2.2. Distribution of Paleoseismic Records along the CSZ 3
1.3. Coseismic Subsidence and Relative Sea Level Change 5
1.4. Goals and Objectives 6
1.5. Thesis Overview 7

Chapter 2. X-ray Fluorescence (XRF): Background, Methodologies, and Considerations 9
2.1. XRF Theory 9
2.1.1. X-ray Interactions 9
2.1.2. Incident X-ray Generation 11
2.2. Conventional XRF vs. XRF-CS 12

Chapter 3. Elemental Composition of Surface Sediment as a Sea/Land-Level Indicator in Cascadia Salt Marshes 13
3.1. Abstract 13
3.2. Introduction 14
3.3. Study Area 16
3.3.1. Cascadia Subduction Zone 16
3.3.2. Port Alberni, British Columbia, Canada 19
3.3.3. Willapa Bay, Washington, USA 20
3.4. Methods 23
3.4.1. Surface Sediment Sample Collection 23
3.4.2. X-ray Fluorescence (XRF) Analysis 24
3.4.3. Statistical Analysis 26
3.5. Results 28
3.5.1. General Geochemical Trends within Cascadia Salt Marshes 28
3.5.2. Geochemical Composition of Port Alberni Transects 30
Port Alberni Transect 1 (PA1) 30
Port Alberni Transect 2 (PA2) 31

Port Alberni Transect 3 (PA3) 32
3.5.3. Geochemical Composition of Willapa Bay Transects 37
Smith Creek Transect 1 (SC1) 37
Bone River Transect 1 (BON1) 38
Bone River Transect 2 (BON2) 38
Niawiakum River Transect 1 (NIA1) 39
Niawiakum River Transect 2 (NIA2) 40
Naselle River Transect 1 (NAS1) 41
Naselle River Transect 2 (NAS2) 41
3.5.4. Comparison between Elemental and Microfossil Clusters 51
3.5.5. Regional – Port Alberni and Willapa Bay 51
3.6. Discussion 56
3.6.1. Vertical Zonation of Elements within Cascadia Salt Marshes 56
3.6.2. Drivers of Elemental Variability 57
Inorganics 58
Organics 58
3.6.3. Elemental Geochemistry as a Sea-Level Indicator 59
Comparison with other Geochemical Indicators 60
3.6.4. The Future of Elemental Geochemistry as a Sea-level Indicator 62
3.7. Conclusion 62

Chapter 4. Conclusion 64
4.1. Summary 64
4.2. Research Contributions 65

References 66

Appendix A. Supplemental files for Chapter 3 85

List of Tables

Table 3-1 – Summary of transects (location, stations, and sampled environment) from Port Alberni (Riou, 2023) and Willapa Bay (Hong et al. 2021) 23

Table 3-2 – Summary of PAM cluster analysis with average silhouette widths of each clustered scenario 29

Table 3-3 – Summary of Adjusted Rand Index (ARI) values comparing similarities between observed environmental zones, geochemical clusters, and microfossil clusters 29

Table 3-4 – Summary of PCA results (cumulative variance [%]) for principal components (PC) explained by elemental variables 30

List of Figures

Figure 3-1 Location of field sites in Port Alberni, Canada and Willapa Bay, USA relative to the Cascadia Subduction Zone. **(A)** Broadscale tectonics associated with the Cascadia Subduction Zone. **(B)** Map of Barkley Sound and the Alberni Inlet connecting the Port Alberni field site to the Pacific Ocean. **(C)** Location of Port Alberni, British Columbia and **(D)** Willapa Bay, Washington with major geomorphological features indicated..... 18

Figure 3-2 Location of Surface Sediment transects at Port Alberni and Willapa Bay. **(A)** Port Alberni with sampling transects marked with yellow lines. **(B)** Smith Creek with sampling transects marked with yellow lines. **(C)** Bone River with sampling transects marked with yellow lines. **(D)** Naselle River with sampling transects marked with yellow lines. **(E)** Niawiakum River with sampling transects marked with yellow lines. 22

Figure 3-3 Example of surface sediment in sequential sample reservoirs (SSR) **(A)** Smith Creek transect 1 (SC1) with station labelled. **(B)** SC1 surface samples prepared and loaded into SSR for XRF analysis on the ITRAX-CS. 25

Figure 3-4 Elemental geochemical data for Port Alberni transect 1 (PA1). **(A)** Elemental abundances (normalized to ICR) along the transect. **(B)** PAM cluster silhouette widths for elemental composition. **(C)** PAM cluster plotted in the dimensions of principal component 1 and principal component 2. **(D)** PCA loading vectors (elemental variables) along principal component 1 and principal component 2..... 34

Figure 3-5 Elemental geochemical data for Port Alberni transect 2 (PA2). **(A)** Elemental abundances (normalized to ICR) along the transect. **(B)** PAM cluster silhouette widths for elemental composition. **(C)** PAM cluster plotted in the dimensions of principal component 1 and principal component 2. **(D)** PCA loading vectors (elemental variables) along principal component 1 and principal component 2..... 35

Figure 3-6 Elemental geochemical data for Port Alberni transect 3 (PA3). **(A)** Elemental abundances (normalized to ICR) along the transect. **(B)** PAM cluster silhouette widths for elemental composition. **(C)** PAM cluster plotted in the dimensions of principal component 1 and principal component 2. **(D)** PCA loading vectors (elemental variables) along principal component 1 and principal component 2..... 36

Figure 3-7 Comparison between elemental geochemistry PAM clustering and foraminifera PAM clustering for Port Alberni transects (Riou, 2023). **(A)** Port Alberni transect 1. **(B)** Port Alberni transect 2. **(C)** Port Alberni transect 3. 37

Figure 3-8 Elemental geochemical data for Smith Creek transect 1 (SC1). **(A)** Elemental abundances (normalized to ICR) along the transect. **(B)** PAM cluster silhouette widths for elemental composition. **(C)** PAM cluster plotted in the dimensions of principal component 1 and principal component 2. **(D)** PCA loading vectors (elemental variables) along principal component 1 and principal component 2..... 43

Figure 3-9 Elemental geochemical data for Bone River transect 1 (BON1). **(A)** Elemental abundances (normalized to ICR) along the transect. **(B)** PAM cluster silhouette widths for elemental composition. **(C)** PAM cluster plotted in the dimensions of principal component 1 and principal component 2. **(D)** PCA loading vectors (elemental variables) along principal component 1 and principal component 2..... 44

Figure 3-10 Elemental geochemical data for Bone River transect 2 (BON2). **(A)** Elemental abundances (normalized to ICR) along the transect. **(B)** PAM cluster silhouette widths for elemental composition. **(C)** PAM cluster plotted in the dimensions of principal component 1 and principal component 2. **(D)** PCA loading vectors (elemental variables) along principal component 1 and principal component 2..... 45

Figure 3-11 Elemental geochemical data for Niawiakum River transect 1 (NIA1). **(A)** Elemental abundances (normalized to ICR) along the transect. **(B)** PAM cluster silhouette widths for elemental composition. **(C)** PAM cluster plotted in the dimensions of principal component 1 and principal component 2. **(D)** PCA loading vectors (elemental variables) along principal component 1 and principal component 2..... 46

Figure 3-12 Elemental geochemical data for Niawiakum River transect 2 (NIA2). **(A)** Elemental abundances (normalized to ICR) along the transect. **(B)** PAM cluster silhouette widths for elemental composition. **(C)** PAM cluster plotted in the dimensions of principal component 1 and principal component 2. **(D)** PCA loading vectors (elemental variables) along principal component 1 and principal component 2..... 47

Figure 3-13 Elemental geochemical data for Naselle River transect 1 (NAS1). **(A)** Elemental abundances (normalized to ICR) along the transect. **(B)** PAM cluster silhouette widths for elemental composition. **(C)** PAM cluster plotted in the dimensions of principal component 1 and principal component 2. **(D)** PCA loading vectors (elemental variables) along principal component 1 and principal component 2..... 48

Figure 3-14 Elemental geochemical data for Naselle River transect 2 (NAS2). **(A)** Elemental abundances (normalized to ICR) along the transect. **(B)** PAM cluster silhouette widths for elemental composition. **(C)** PAM cluster plotted in the dimensions of principal component 1 and principal component 2. **(D)** PCA loading vectors (elemental variables) along principal component 1 and principal component 2..... 49

Figure 3-15 Comparison between elemental geochemistry PAM clusters and diatom hierarchical clustering at Willapa Bay. Clustered diatom data obtained from Hong et al. (2019). **(A)** Smith Creek transect 1. **(B)** Bone River transect 1. **(C)** Bone River transect 2. **(D)** Niawiakum River transect 1. **(E)** Niawiakum River transect 2. **(F)** Naselle River transect 1. **(G)** Naselle River transect 2..... 50

Figure 3-16 Local and Regional comparison of elemental geochemistry. **(A)** Local Port Alberni PAM clusters. **(B)** Local Port Alberni PCA loading vectors along principal component 1 and principal component 2. **(C)** Local Willapa Bay PAM clusters. **(D)** Local Willapa Bay PCA loading vectors along principal component 1 and principal component 2. **(E)** Regional Port Alberni and Willapa Bay PAM cluster. **(F)** Regional Port Alberni and Willapa Bay PCA loading vectors..... 54

Figure 3-17 Boxplots of normalized elemental counts against observed environmental zones as described by salt marsh vegetation for Port Alberni and Willapa Bay. For each boxplot, the dark horizon bar represents the medium, the solid box represents the interquartile range, the vertical lines represent the minimum and maximum values, and the dots beyond the whiskers represent outliers. 55

Figure 3-18 Conceptual model and summary of idealized vertical zonation patterns of foraminifera, testate amoebae, diatoms, and elemental geochemistry at Port Alberni and Willapa Bay. 57

List of Acronyms

SFU	Simon Fraser University
LAC	Library and Archives Canada
CSZ	Cascadia Subduction Zone
OSL	Optically Stimulated Luminescence
RSL	Relative Sea Level
XRF	X-ray Fluorescence
XRF-CS	X-ray Fluorescence Core Scanning
PAM	Partitioning around Medoids
PCA	Principal Component Analysis
PC	Principal Component
BTF	Bayesian Transfer Function
BC	British Columbia, Canada
WA	Washington, USA
PA	Port Alberni, British Columbia, Canada
NOAA	National Oceanic and Atmospheric Administration
RTK-GNSS	Real-time Kinematic Positioning Global Navigation Satellite System
RTK-GPS	Real-time Kinematic Global Positioning System
MTL	Mean Tide Level
SWLI	Standardized Water Level Index
NAVD88	North American Vertical Datum of 1988
SSR	Sequential Sample Reservoir
ARI	Adjusted Rand Index
ICR	Incoherent Coherent Scattering Ratio
LOI	Loss-on-Ignition
RE	Rock-Eval Pyrolysis
MLC	Multivariate Linear Calibration Model
ICP-MS	Inductively Coupled Plasma Mass Spectrometry

“Breathing in, I have arrived.

Breathing out, I am home”

Chapter 1.

Background

1.1. Introduction

Many of the world's largest and most densely populated cities are located along coastlines where communities are at risk from coastal hazards such as sea-level rise, coastal erosion, and tropical cyclones. Coastal areas surrounding the Pacific Ocean are additionally susceptible to large subduction zone earthquakes and their associated tsunamis because of the extensive network of subduction interfaces along the perimeter of the Pacific Ocean, known as the Pacific Ring of Fire (e.g., Clague et al., 2000). Subduction zones are known to generate some of the largest megathrust earthquakes and subsequent tsunamis, which are capable of inundating coastlines around the Pacific Ocean up to several kilometers inland (e.g., Atwater et al., 2011). Recent megathrust earthquakes occurring along the Pacific Ring of Fire include the 2004 Sumatra – Andaman earthquake, which generated tsunami waves that reached heights in excess of 22 m, devastating coastlines in 14 countries and resulting in over 230,000 causalities (Rabinovich et al., 2015).

Reconstructing the frequency and magnitude of past megathrust earthquakes is crucial for bolstering resiliency for local communities and for cautioning coastal communities further afield about the potential for cascading hazards resulting from both near- and far-field tsunamis (e.g., Atwater et al., 1995; Clague et al., 2000; Goff et al., 2020; Nelson et al., 2021). The recurrence interval of large earthquakes along subduction zones is often on the order of hundreds to thousands of years, such that historical records do not always encompass the full spectrum of these hazards, which in turn hinders the proper assessment of risk (e.g., Rubin et al., 2017; Sawai et al., 2012). Without comprehensive or sufficiently long historical records, patterns of recurrence and magnitude of past earthquakes cannot be properly assessed, and in turn, the potential impacts of future earthquakes and tsunamis remain speculative. Fortunately, the geologic record enables the reconstruction of much longer records of earthquakes to better constrain the frequency and magnitude of events occurring over complete

earthquake cycles (e.g., Dura et al., 2015; Goldfinger et al., 2012; Hutchinson & Clague, 2017; Rubin et al., 2017; Sawai et al., 2012).

1.2. Cascadia Subduction Zone

The Cascadia subduction zone (CSZ) is located along the west coast of North America, extending from southern British Columbia to northern California, where the Juan de Fuca plate subducts beneath the North American plate (Figure **3-1**A). Along the subduction zone, the Juan de Fuca plate converges to the northeast at a rate of 35 – 45 mm/yr relative to the stable continental North American plate (e.g., Dragert et al., 1994; McCaffrey et al., 2013; Miller et al., 2001). The CSZ has not experienced a large subduction zone earthquake in over 300 years, limiting our understanding of seismicity and associated hazards for coastlines in this region. The most recent megathrust earthquake to impact the CSZ occurred on January 26, 1700, and the associated tsunami waves inundated both local and far-field coastlines (e.g., Atwater et al., 2011). Indigenous oral histories from the Pacific Northwest document the lived experiences of shaking and flooding associated with the 1700 CSZ event through historical and mythological stories passed through the generations (e.g., Ludwin et al., 2005; McMillan & Hutchinson, 2002). Written Japanese records from the 18th century also capture the 1700 event as an “orphan” tsunami of unknown origin inundating Japanese coastlines (e.g., Satake et al., 1996). Subsequent to the oral and written histories of the 1700 earthquake and tsunami, geologic evidence from coastal regions in Cascadia was discovered, which records sudden environmental changes associated with coseismic subsidence and tsunami deposition (e.g., Atwater, 1987; Atwater et al., 2011; Clague & Bobrowsky, 1994; Hemphill-Haley, 1995).

1.2.1. Recognizing Past Earthquakes in the Geologic Record

Coastal salt marshes are excellent archives of the geologic records produced by megathrust earthquakes in Cascadia (Atwater, 1987; Guilbault et al., 1996; Hawkes et al., 2011; Kemp et al., 2018; Padgett et al., 2022), Chile (e.g., Dura et al., 2015; Garrett et al., 2013, 2015), New Zealand (e.g., Garrett et al., 2023; Hayward et al., 2016), Japan (Garrett et al., 2016; Sawai, Horton, et al., 2004), and Sumatra (Dura et al., 2011; Grand Pre et al., 2012). During interseismic periods (i.e., between earthquakes), ongoing

convergence drags down the seaward edge of the continental plate, resulting in uplift and crustal shortening. During subduction zone ruptures, the seaward edge of the continental margin springs upward, resulting in instantaneous subsidence and crustal extension, known as coseismic subsidence. In salt marshes, coseismic subsidence is often recorded as peat-mud couplets (buried soils), with pre-earthquake intertidal peat suddenly lowered further into the intertidal and subtidal zones and over which mud is subsequently deposited (e.g., Atwater, 1987; Shennan et al., 1996). Tsunami inundation from large earthquakes can also be recorded in salt marsh stratigraphy as a thin marine sand layer between the peat-mud contact (e.g., Clague et al., 2000; Hemphill-Haley, 1995). Within the coastal stratigraphy, the recurrence interval of megathrust earthquakes can therefore be determined by identifying peat-mud couplets and constraining their ages using dating methods such as ^{14}C (e.g., Hutchinson & Clague, 2017; Nelson et al., 2021). Studies adopting these methods have revealed geologic evidence of repeated megathrust earthquakes in Cascadia occurring over the past 300 – 7000 years (e.g., Atwater et al., 1995; Graehl et al., 2015; Hutchinson & Clague, 2017; Shennan et al., 1996; Witter et al., 2003).

1.2.2. Distribution of Paleoseismic Records along the CSZ

Paleoseismic records are not uniformly distributed along the CSZ. Records in northern Cascadia (i.e., southern British Columbia) are sparse in comparison to the wealth of geologic records south of the Canada-U.S. border in Washington, Oregon, and California (e.g., Hutchinson & Clague, 2017; Leonard et al., 2010). Paleoearthquakes identified in the geologic record that have overlapping ages can be correlated spatially along the length of the subduction zone to identify local or full margin events (e.g., Hutchinson & Clague, 2017; Nelson et al., 2021). Reconstructing paleoseismic records and interpreting seismic risk along the Cascadia coastline are dependent on robust and continuous geologic records along the entire length of the CSZ.

Coastal salt marshes are ideal environments for preserving evidence of earthquakes and tsunamis, however there is considerable variation in the distribution of reported geologic evidence along the Cascadia coastline. Salt marshes in central and southern Cascadia are well developed and extensive; whereas those in northern Cascadia are restricted to fewer locations and, where present, the stratigraphic sequence is often shorter and constrained by rocky headlands (e.g., Clague et al., 2000;

Guilbault et al., 1996). The variation in salt marsh development and distribution along Cascadia predominantly are the result of deglaciation and relative sea level (RSL) change during the Holocene (e.g., Dura et al., 2016b; Engelhart et al., 2015). The preservation of paleoseismic records in Cascadia is enhanced by the spatial distribution of well-developed salt marshes, which in turn is controlled by the regional RSL history. Central and southern Cascadia experienced gradual RSL rise during the mid-late Holocene due to its location beyond the perimeter of the North American ice sheets (e.g., Dura et al., 2016b). During the last glaciation, loading by ice sheets caused mantle migration towards the periphery resulting in uplift within the proglacial forebulge. Subsequently, deglaciation resulted in the mantle returning to previously ice loaded centers, and the collapse of the proglacial forebulge. This collapse caused gradual land subsidence and corresponding gradual RSL rise in central and southern Cascadia, which, in turn, created accommodation space and promoted sediment accumulation, and the formation of well-established coastal salt marshes. In contrast, northern Cascadia was covered by the Cordilleran Ice Sheet during the last glaciation, which resulted in glacioisostatic subsidence (Clague & Ward, 2011). As the Cordilleran Ice Sheet retreated during deglaciation, RSL fell as a result of glacial unloading and isostatic uplift. The RSL fall experienced in northern Cascadia limited accommodation space and starved coastlines of sediment, resulting in thin and discontinuous coastal marsh sequences (e.g., Dura et al., 2016b; Hutchinson & Clague, 2017).

In spite of the challenges associated with the scarcity of salt marshes in northern Cascadia, evidence for earthquakes and tsunamis have still been identified there (e.g., Benson et al., 1997; Clague et al., 1999; Clague & Bobrowsky, 1994; Guilbault et al., 1995, 1996). The relative sparsity of long-term earthquake and tsunami records in this region limits our ability to accurately make correlations with potential counterparts in central and southern Cascadia. Limited geologic evidence from northern Cascadia also hinders the accuracy of dynamic rupture models because there is only limited ground-truthed geological evidence available for data-model integration (e.g., Wang et al., 2013). As a result, the rupture pattern of the 1700 CE Cascadia earthquake (i.e., full trench rupture vs. multi-segment rupture) remains unclear and a source of debate in the literature (e.g., Hutchinson & Clague, 2017; Leonard et al., 2010; Wang et al., 2013).

1.3. Coseismic Subsidence and Relative Sea Level Change

Coseismic subsidence associated with large megathrust earthquakes can be quantified by reconstructing relative sea-level change because instantaneous land subsidence is reflected in instantaneous sea-level rise (Dura et al., 2016a; Hawkes et al., 2011; Pilarczyk et al., 2014). Within salt marsh environments, repeated tidal inundation creates distinct sub-environmental zones that are controlled by the frequency and duration of tidal inundation. The frequency and duration of tidal inundation are in turn, controlled by elevation gradient relative to sea-level, whereby lower elevations are inundated more frequently than higher elevations. This results in consistent depositional patterns along the intertidal gradient and forms the foundation for reconstructing relative sea-level change in salt marsh environments (e.g., Barlow et al., 2013).

Reconstructing sea-level change relies on the use of sea-level indicators, which are physical, biological, or chemical proxies that have a consistent and quantifiable relationship with tidal elevation (van de Plassche, 1986). Microfossils (i.e., foraminifera, diatoms) are well established sea-level indicators that have been used to reconstruct instantaneous sea-level change across a peat-mud couplet produced by coseismic subsidence (e.g., Atwater & Hemphill-Haley, 1997; Hawkes et al., 2011; Woodroffe & Long, 2010). Microfossil assemblages within salt marsh peat are intimately linked to tidal elevation because periodic tidal inundation creates distinct environmental conditions (e.g., salinity, mud fraction, grain size, tidal elevation) (Scott & Medioli, 1978; Vos & de Wolf, 1993). Microfossil species often have a narrow range of environmental tolerance and will be most abundant within species-optimal environmental conditions. The well-established relationship between microfossil assemblages and tidal elevation within coastal salt marshes has been documented around the world and is often applied to paleodeposits to infer changes in tidal elevation or sea/land-level change over time (e.g., Barnett et al., 2015; Hawkes et al., 2011; Hayward et al., 2016; Horton & Edwards, 2006; Kemp et al., 2012).

Modern training sets are paired sea-level indicator data that describe the relationship between a particular proxy and its closely associated environmental variables (e.g., tidal elevation, salinity, temperature). These training sets are therefore used as modern analogues to interpret the sedimentary record (e.g., Hocking et al., 2017; Hong et al., 2021; S. Williams et al., 2021). Transfer functions are statistical

models that use training sets as modern analogues to reconstruct changes in tidal wetland environments (e.g., Cahill et al., 2016; Kemp et al., 2018; Sachs et al., 1977). The accuracy of a transfer function, and therefore the reconstruction, rely on a robust modern training set that captures a complete range of environments that may be encountered in the sedimentary record (e.g., Birks, 1995; Watcham et al., 2013). Modern training sets and transfer functions create a two-step approach for high-resolution sea-level reconstructions that can also be applied to quantify coseismic subsidence from megathrust earthquakes. Since the establishment of a modern training set is the prerequisite for the sea/land-level reconstruction, the variable spatial distribution of modern training sets along the length of the Cascadia coastline limits the locations of the reconstructions. For example, there are well established modern training sets based on foraminiferal distributions in central and southern Cascadia, but in northern Cascadia (i.e., British Columbia) training sets are more limited (e.g., Guilbault et al., 1995; Jonasson & Patterson, 1992; Mathewes & Clague, 1994; Patterson et al., 1999).

1.4. Goals and Objectives

Establishing modern training sets in northern Cascadia will fill spatial gaps in their distribution along the entire length of the Cascadia subduction zone. Current established training sets are based on microfossils such as foraminifera or diatoms. Despite their prevalence in coastal sediments, shortcomings such as preservation potential and poor agreement between modern and fossil assemblages, can limit their utility as a sea/land-level indicator (e.g., Khan et al., 2019; Woodroffe, 2009). These shortcomings warrant development of additional sea-level indicators that can be applied to supplement microfossils or serve as a stand-alone proxy.

This thesis explores the utility of elemental geochemistry through x-ray fluorescence core scanning (XRF-CS) as a sea/land-level indicator and establishes a modern elemental training set for northern Cascadia. It addresses the question as to whether the elemental geochemistry within salt marshes displays similar vertical zonation patterns to the well-established microfossil assemblages. This project builds on previous work at Port Alberni, British Columbia, Canada and Willapa Bay, Washington, USA where modern training sets for foraminifera and diatoms were developed by Riou (2023) and Hong et al. (2021) respectively (Figure **3-1**). Elemental geochemistry of salt marsh sediment is compared with well-established sea-level indicators to assess the

potential for future sea/land-level reconstructions. Developing a new geochemistry-based sea/land-level indicator may allow transfer functions to be more flexible and robust. Investigating salt marshes from northern Cascadia, where dynamic rupture models suggest additional geologic evidence is needed, fills important spatial gaps along the CSZ and will lead to an improved understanding of plate boundary processes occurring long the entire subduction zone.

This thesis is founded on the following objectives:

1) Does the elemental geochemistry of bulk salt marsh sediment show similar vertical patterns to previously established microfossil datasets?

2) What are the processes controlling elemental distribution along the elevation gradient of the salt marsh?

3) Generate the first elemental geochemistry modern training set describing the relationship between elemental abundances and tidal elevation within a salt marsh.

1.5. Thesis Overview

This thesis is organized as a “sandwich style” thesis, which augments a stand-alone journal article. Chapter 1 is an introduction that provides background on CSZ paleoseismology.

Chapter 2 is a methodological section which delves into the considerations and background of XRF-CS methodologies and post-processing techniques.

Chapter 3 is the main part of the thesis and is written as a stand-alone journal article that investigates the use of elemental composition of salt marsh surface sediments and their potential as sea/land-level indicators in Cascadia. The manuscript, formatted for *Geophysics, Geochemistry, Geosystems*, is led by myself and co-authored by Jessica Pilarczyk (Department of Earth Sciences, Simon Fraser University), Isabel Hong (Department of Geography and the Environment, Villanova University), Louise Riou (Department of Earth Sciences, Simon Fraser University), David Huntley (Geologic Survey of Canada), Roger MacLeod (Geologic Survey of Canada), Owen Ward

(Department of Statistics and Actuarial Science, Simon Fraser University), John Clague (Department of Earth Sciences, Simon Fraser University), and Peter Bobrowsky (Geologic Survey of Canada).

Jessica Pilarczyk proposed the idea of exploring elemental geochemistry as a sea-level indicator and provided the ITRAX Core Scanner used for this project. Isabel Hong provided surface sediment samples from Willapa Bay, Washington, and the associated diatom modern training set. Louise Riou provided surface sediment samples from Port Alberni, British Columbia, and the associated foraminiferal modern training set. David Huntley and Roger MacLeod assisted with field work and provided detailed elevation measurements and tide gauge data for Port Alberni. Owen Ward provided guidance on statistical approaches for comparing XRF and microfossil data. John Clague, David Huntley, and Peter Bobrowsky assisted with field logistics, advice related to fieldwork and data collection at the Port Alberni field site, and shared insights based on their lengthy research in the region. In my role as primary author, I obtained field data, completed all XRF analyses on surface sediment training sets from both Port Alberni and Willapa Bay, post-processed all XRF data, and performed statistical analyses on both the microfossil training sets and all XRF data generated as part of this work. I also wrote the manuscript, created all figures, and assembled data tables available through SFU Summit Research Repository.

Chapter 4, the final section of the thesis, summarizes the study, highlights the main research contributions of the work, and presents recommendations for future studies to further establish elemental geochemistry and XRF as a proxy sea-level indicator. The “sandwich style” organization results in content that is reiterated to help with the cohesiveness and flow of the thesis.

Chapter 2.

X-ray Fluorescence (XRF): Background, Methodologies, and Considerations

2.1. XRF Theory

XRF is an analytical approach that has been applied in geologic investigations due to its ability to determine the elemental composition of a wide range of geologic materials. It offers a powerful analytical tool that has yet to be applied to investigate sea/land-level change associated with subduction zone earthquakes.

2.1.1. X-ray Interactions

In XRF analysis, samples are irradiated with x-rays and emit fluorescence photons with energies related to the elemental composition of a particular material. When an x-ray encounters an atom, three main interactions may occur: fluorescence, incoherent (Compton) scattering, and coherent (Rayleigh) scattering. X-rays are either absorbed (resulting in fluorescence), scattered (Compton or Rayleigh), or pass through the material (no interaction) (Jenkins, 1999). The processes involved in these interactions can be explained using the Bohr model of an atom (Bohr, 1913; Svidzinsky et al., 2005). In the Bohr model, a nucleus composed of positive protons and neutral neutrons is surround by electrons grouped into orbitals or shells. The innermost orbital is known as the K-shell, and electrons in this orbital have the largest binding energies within the atom. Outside the K-shell are the L-shell and M-shell, each with electrons that have successively lower binding energies. In XRF analysis, all photon energies are detected regardless of which x-ray interaction or electron orbital generated the photon.

When an atom at ground state (i.e., lowest energy electron configuration) is irradiated, x-rays with sufficiently large energies (larger than the binding energy of the electron) will eject the electron from the innermost K-shell, creating a vacancy in the electron orbital and leaving the atom in an excited state. An electron in the L-shell (higher energy orbital) will transfer to a vacancy in the K-shell, emitting a fluorescent x-ray photon. The x-ray photon has an energy equal to the energy difference between the

atom's L-shell and K-shell, which is an atom's characteristic fluorescence emission and is unique for each element. An atom will produce more than one characteristic fluorescent emission because there are many combinations of electron transitions that may occur (e.g., M-Shell to K-Shell or L-Shell to K-Shell). Therefore, every element has its own characteristic fluorescence emission energies that are related to the energy of the orbitals where an electron transition occurs (Jenkins, 1999).

Scattering occurs when an incident x-ray is redirected or changes direction due to an interaction with an electron. Incoherent scattering occurs when the x-ray loses energy to the electron, while coherent scattering involves no change in x-ray energy (Fernández, 1992). Lighter elements have lower electron binding energies than heavier elements because there are fewer protons in the nucleus to hold the negative electrons in the orbitals. Therefore, it requires less energy to eject an electron from a light element (e.g., C, N, O) than from a heavy element. The energy difference between the incident x-ray and the electron binding energy (i.e., how tightly the electron is held in the orbital) controls whether the x-ray is scattered through incoherent or coherent processes. Incoherent scatter is more prevalent with light elements (i.e., low atomic number elements) because of their low binding energies, while coherent scatter is more common with heavier elements (i.e., high atomic number elements) because of higher binding energies (Fernández, 1992). For geologic applications, x-ray scattering provides insights into the average atomic number of the elemental composition (e.g., Chawchai et al., 2016; Woodward & Gadd, 2019). Organic materials are primarily composed of organic forming elements such as hydrogen (H), carbon (C), nitrogen (N), and oxygen (O), which are relatively light elements. Clastic sediments are generally comprised of heavier lithogenic elements such as silicon (Si), titanium (Ti), and potassium (K). Therefore, organic-rich sediment has high incoherent scattering and low coherent scattering, while clastic sediment has the opposite.

While in theory, XRF can distinguish all elements based on their characteristic fluorescence emissions, there are some practical considerations that complicate the analysis. XRF is incapable of detecting low atomic number elements ($Z<11$, e.g., H, C, N, O) because the energy of fluorescence emission is too low (self-absorption) or the photon is absorbed before reaching the detector (Beckhoff et al., 2006). Although XRF cannot detect light elements based on characteristic fluorescence emissions, it can be

used to indirectly measure with incoherent and coherent scattering (e.g., Chawchai et al., 2016; Fernández, 1992; Woodward & Gadd, 2019).

2.1.2. Incident X-ray Generation

X-rays are generated within an x-ray tube under a potential difference (i.e., voltage), where electrons are accelerated from a negative cathode towards a positive target anode. When a target anode is bombarded with incident electrons, there are two processes that will generate an x-ray. The first process, characteristic x-ray production, is similar to x-ray fluorescence where an incident electron ejects an inner electron from the target atom in the anode. Subsequently, an electron from a higher energy orbital will fall to fill the vacancy which generates a characteristic and discrete x-ray photon that is related to the energy difference between the target atom's electron orbitals. Therefore, characteristic x-ray production can be varied by using different target anodes to generate specific x-ray energies (Jenkins, 1999). Common target anode elements include tungsten (W), chromium (Cr), molybdenum (Mo), and rhodium (Rh) (Croudace et al., 2006).

The second process is known as 'bremsstrahlung', or braking radiation, which produces a continuous x-ray energy spectrum (Jenkins, 1999). When incident electrons pass by the nucleus of an atom, they decelerate and change direction, which converts the kinetic energy of the electron into an x-ray photon. The energy of the x-ray generated through braking radiation is a continuous spectrum because an electron can experience any amount of "braking" depending on its proximity to the nucleus. Aside from changing the target anode, x-ray characteristics can also be controlled by the current and voltage applied to generate the potential difference across the x-ray tube. The number of electrons generated is dictated by the current, while the energy of each electron is controlled by the voltage, which affects the braking radiation and continuous x-ray spectrum generated. The current and voltage can be set to excite a wide range of elements or tailored to increase the resolution of an element of interest. In this project, x-rays were generated at 55 mA and 30 kV on a Mo x-ray tube, which has been shown to excite the largest range of common geologic elements (e.g., Jones et al., 2019; Löwemark et al., 2019).

2.2. Conventional XRF vs. XRF-CS

X-ray fluorescence core scanning (XRF-CS) offers many advantages over conventional XRF, such as rapid analysis, low operational costs, and high resolution when compared (Croudace et al., 2006). The drawbacks of XRF-CS are that the accuracy and precision of elemental analysis are slightly less than those obtained using conventional geochemical methods (e.g., Tjallingii et al., 2007). The fundamental instrumentation for both conventional XRF and XRF-CS includes an x-ray source that generates incident x-rays to irradiate samples and a detector that captures fluorescence emissions from the sample. The main difference between conventional XRF and XRF-CS approaches is in the sample preparation, which dictates the advantages and disadvantages of both methods.

Conventional XRF methods require rigorous sample preparation that involves discrete subsampling of cores and is therefore a destructive process. Common approaches involve drying, grinding, and pelletizing sediment samples, which homogenize materials and sets a standard configuration of sample dimensions (e.g., Injuk et al., 2006). Sample preparation in conventional XRF methods reduces analytical error caused by ‘specimen effects’, which are differences resulting from sample heterogeneity and irregular surface topography or geometry (e.g., Weltje & Tjallingii, 2008). In XRF-CS, the ‘specimen effect’ is poorly constrained because split sediment cores often display downcore variations of density, water content, surface topography, and grain size (e.g., Weltje & Tjallingii, 2008). Various statistical approaches have been developed to normalize or transformation XRF-CS data to minimize the influence of the specimen effect and has been shown to generate comparable results to conventional geochemical approaches (e.g., Gregory et al., 2019; Mondal et al., 2021; Weltje et al., 2015; Weltje & Tjallingii, 2008). XRF-CS offers extremely rapid and high-resolution analysis when compared to the conventional methods, and associated disadvantages can be accounted for through rigorous statistical methods.

Chapter 3.

Elemental Composition of Surface Sediment as a Sea/Land-Level Indicator in Cascadia Salt Marshes

3.1. Abstract

Many high-resolution sea-level reconstructions rely on physical, biological, and chemical indicators that possess a relationship with elevation within a salt marsh, and therefore, tidal duration. We explore the utility of elemental geochemistry obtained through x-ray fluorescence as a sea/land-level indicator by investigating the elemental composition of surface salt marsh sediments along ten transects from Port Alberni, British Columbia, Canada and Willapa Bay, Washington, USA. Bulk surface sediment samples from a total of 141 stations along the ten transects were analysed for their elemental composition using an ITRAX Core Scanner. Partitioning Around Medoids (PAM) cluster analysis on the elemental data distinguished between tidal flat, low marsh, and high marsh zones at both Port Alberni and Willapa Bay, similar to previously published microfossil datasets on the same surface sediment samples. Principle Component Analysis (PCA) points to the variation in organic verses inorganic content of the sediment, a function of tidal elevation at both marshes, as the main driver of elemental geochemistry-derived zones within the salt marshes. Approximately 70% of the elemental variability within both salt marshes is controlled by inorganic content described by lithogenic (Si, K, Ti, Fe) and biogenic elements (Sr) as opposed to organic content described by organic proxies (Br, incoherent coherent scattering ratio). The modern elemental composition of bulk salt marsh sediment shows a promising relationship with tidal elevation at two Cascadia salt marshes spaced ~290 km apart and highlights the potential of this proxy for sea- and land-level reconstructions in Cascadia.

Keywords: Sea-level change; ITRAX Core Scanner; elemental geochemistry; surface distributions; x-ray fluorescence, PAM-cluster analysis, principal component analysis

3.2. Introduction

Sea-level reconstructions using salt marsh sediments are an important addition to modern instrumental records because they reveal decadal- to millennial-scale records into the timing and rates of sea-level change (Barlow et al., 2013). Holocene sea-level reconstructions often rely on indicators derived from in-situ salt marsh sediments that have a consistent and quantifiable relationship to tidal elevation (van de Plassche, 1986). A wide range of sea-level proxies have been used to reconstruct the position of former coastlines. They include physical (e.g., sedimentological, geomorphological; Evelpidou et al., 2012; Hein et al., 2013; Little et al., 2009), biological (e.g., vegetation, foraminifera, diatoms; Scott & Medioli, 1978; Zong & Horton, 1999), and chemical (e.g., stable carbon isotopes; Kemp et al., 2019; Khan et al., 2019) indicators. Employing sea-level indicators to reconstruct Holocene sea-level change is based on the assumption that modern distributions of a particular indicator do not change through time, and can be used as an analogue to estimate past sea-level change from the sedimentary record (e.g., Barlow et al., 2013). In this way, reconstructing past sea-level change relies on a robust understanding of the modern relationship among a particular indicator, tidal elevation, and environmental variables (e.g., Hong et al., 2021; Kemp et al., 2012; Sawai et al., 2022).

Intertidal microfossils (foraminifera, diatoms) are among the most common proxies used to reconstruct past sea levels owing to their high abundance in marsh sediment and their ecological niches that are linked to tidal elevation (Dura et al., 2016a; Horton & Edwards, 2006; Pilarczyk et al., 2014; Scott & Medioli, 1978). In salt marshes, the distribution of microfossil assemblages is controlled by the frequency and duration of tidal inundation, which is mainly a function of elevation (Horton & Edwards, 2006; Scott & Medioli, 1978; Zong & Horton, 1999). The modern relationship between microfossil assemblages and elevation along a coastline can be applied to interpret sedimentary records to estimate paleomarsh elevation, and to reconstruct sea-level change over the Holocene (e.g., Barlow et al., 2013; Barnett et al., 2015; Kemp et al., 2013; Stéphan et al., 2015; Williams et al., 2023; Woodroffe & Long, 2010).

Microfossil-based sea-level reconstructions may also reveal abrupt changes in paleomarsh elevation resulting from sudden land-level change, for example, coseismic subsidence/uplift associated with large subduction zone earthquakes (e.g., Dura et al.,

2016a; Pilarczyk et al., 2014). Detailed records of evidence for coseismic subsidence derived from assemblages of intertidal diatoms and foraminifera have provided important insight into the frequency, magnitude, and spatial extent of subduction zone earthquakes in Cascadia (e.g., Guilbault et al., 1995; Kelsey et al., 2002; Kemp et al., 2018; Padgett et al., 2022), Alaska (e.g., Briggs et al., 2014; Shennan et al., 2018; Shennan & Hamilton, 2006), Chile (e.g., Brader et al., 2021; Dura et al., 2017; Garrett et al., 2015), New Zealand (e.g., Clark et al., 2015; Cochran et al., 2007; Hayward et al., 2016), Japan (Garrett et al., 2016; Sawai et al., 2004a,b) and Sumatra (e.g., Grand Pre et al., 2012), as well as other locations.

In addition to microfossil-based sea- and land-level reconstructions, geochemical proxies, such as stable carbon isotopes ($\delta^{13}C$, C/N) and total organic carbon (TOC), have been explored for their potential as indicators of sea-level position (e.g., Kemp et al., 2010, 2017; Khan et al., 2019; Lamb et al., 2006). These geochemical proxies have also been successfully used as priors, which are complementary proxies that help to constrain the estimated paleo-elevation based on additional environmental variables, in sea-level reconstructions that utilize a Bayesian transfer function (BTF; e.g., Cahill et al., 2016; Kemp et al., 2018).

While elemental geochemistry obtained through x-ray fluorescence (XRF) has been successfully used to understand and reconstruct paleoenvironments in peats and other organic-rich environments (e.g., Longman et al., 2019; Turner et al., 2015; Unkel et al., 2010), its utility as a potential sea-level indicator has been underutilized. Investigating the potential for additional sea-level indicators and associated priors may lead to more robust sea- and land-level reconstructions, as even well-established proxies such as microfossils do not always work as expected at all locations due to environmental variables and the occasional discrepancy between modern and fossil assemblages (e.g., Woodward & Gadd, 2019).

XRF is an analytical technique used to determine the elemental composition of a given material and can detect a wide range of elements from Al to U. The advent of x-ray fluorescence core scanning (XRF-CS) allowed for rapid, non-destructive, continuous, and high-resolution analysis of a wide range of geologic materials (Croudace et al., 2006). XRF-CS has been readily adopted into paleoenvironmental and paleoclimatic reconstructions because of its ability to resolve subtle changes in the elemental

composition of a sediment core at a resolution up to 100 µm. The elemental composition of sediment cores has been used to interpret long-term climatic records such as changes in hydrologic cycles, depositional processes, and glacial histories, (e.g., Chawchai et al., 2015; Gregory et al., 2021; Kaboth-Bahr et al., 2019; Kylander et al., 2011; Mushet et al., 2022; Steele et al., 2023), as well as rapid and instantaneous events such as storms and tsunamis (e.g., Ishizawa et al., 2019; Moreira et al., 2017; Oliva et al., 2018; Paris et al., 2021; H. Williams et al., 2022). However, the application of elemental geochemistry, obtained through XRF-CS, as a potential sea-level indictor used in millennial-scale sea- and land-level reconstructions has not been fully explored.

In this study, we address the need for providing additional sea-level indicators by assessing the utility of elemental geochemistry determined through XRF-CS. An ITRAX Core Scanner is used to investigate the elemental composition of 141 sediment samples along ten surface transects at two salt marshes, one in Port Alberni, British Columbia, Canada, and the other in Willapa Bay, Washington, USA. We describe the distribution of elements within the salt marshes and compare their distributions with previously published microfossil datasets (Hong et al., 2021; Riou, 2023) to explore the utility of elemental geochemistry as a sea-level indicator.

3.3. Study Area

3.3.1. Cascadia Subduction Zone

The Cascadia subduction zone (CSZ), located on the west coast of North America, extends ~1,000 km from southern British Columbia (Canada) to northern California (USA), where the Juan de Fuca plate converges to the northeast at a rate of 35–45 mm/year relative to the North American plate (Miller et al., 2001; Riddihough, 1984; K. Wang et al., 1997) (Figure **3-1)**.

The CSZ is known to generate large subduction zone earthquakes and associated tsunamis, including a very large event in 1700 CE according to Indigenous oral records (e.g., Ludwin et al., 2005; McMillan & Hutchinson, 2002), historical records from coastal Japan (e.g., Atwater et al., 2011; Satake et al., 1996), and geologic records from Cascadia tidal marshes (e.g., Atwater, 1987). Sea/land-level reconstructions from Cascadia salt marshes, in particular, have since revealed geologic evidence for about 20

such earthquakes occurring in the past 7000 years (e.g., Atwater et al., 1995; Goldfinger et al., 2012; Hutchinson & Clague, 2017; Nelson et al., 2021).

Coastal marshes at Port Alberni (British Columbia, Canada) and Willapa Bay (Washington, USA) record evidence of past Cascadia earthquakes and tsunamis (e.g., Atwater, 1987; Clague et al., 1994; Hemphill-Haley, 1995; Tanigawa et al., 2022) and were selected for this study because their microfossil distributions were previously studied by Riou (2023) and Hong et al. (2019). The two study sites are ~290 km apart and represent different regional settings along the 1,000 km long subduction zone. Port Alberni was impacted by the historical 1964 Alaska tsunami, and previous studies have described evidence for multiple prehistoric tsunamis over the past ~1,000 years (e.g., Clague et al., 1994; Clague & Bobrowsky, 1994; Goff et al., 2020; Shennan et al., 2014; Tanigawa et al., 2022). Similarly, marshes in Willapa Bay are known to contain evidence for coseismic subsidence and tsunamis accompanying multiple prehistoric earthquakes that span the last ~3,500 years (e.g., Atwater, 1987; Hemphill-Haley, 1995). Further earthquake reconstructions from these locations may provide important insight into Cascadia plate boundary processes that will enhance knowledge of seismic risk for coastal communities bordering the Pacific Ocean.

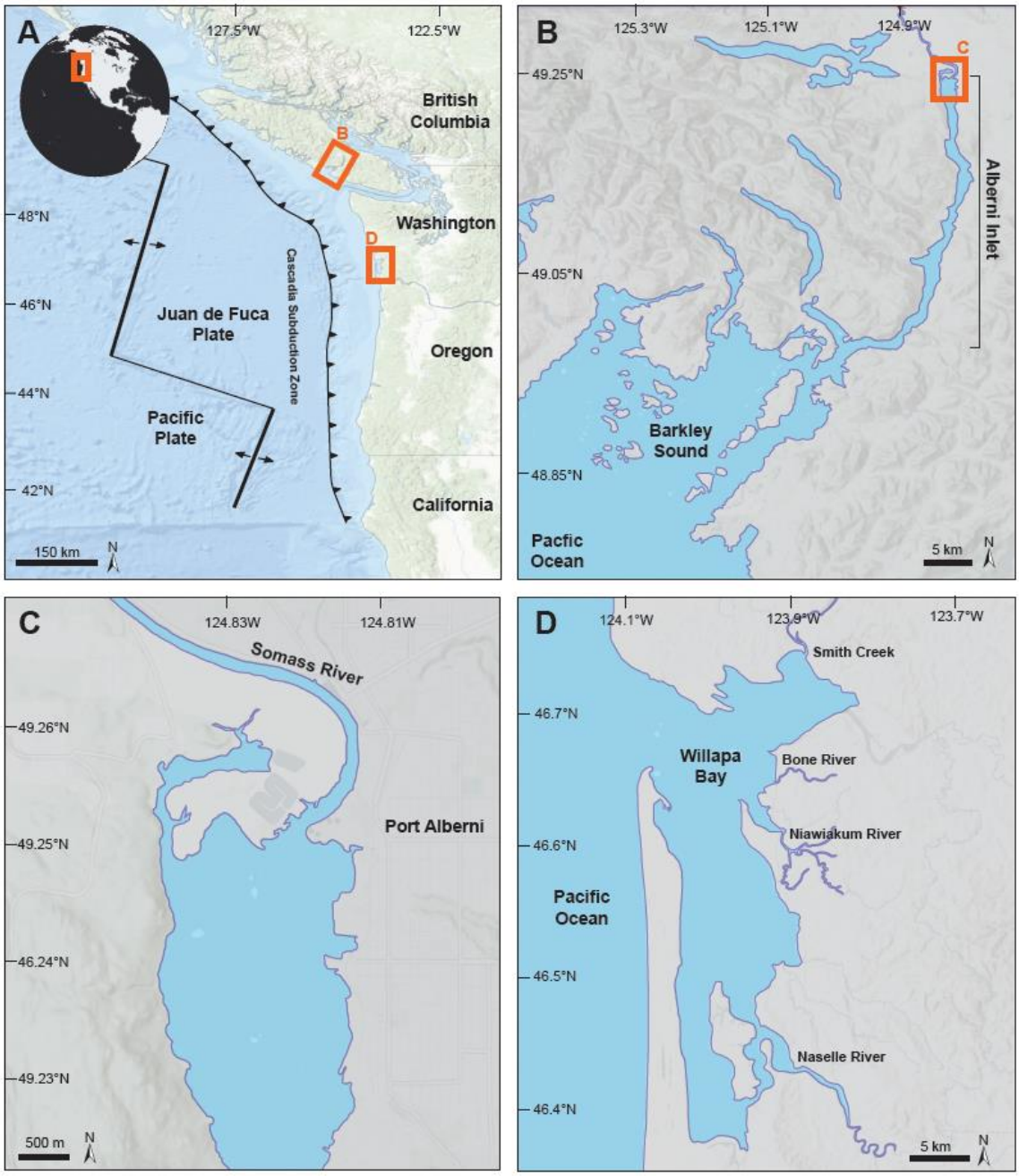

Figure 3-1 Location of field sites in Port Alberni, Canada and Willapa Bay, USA relative to the Cascadia Subduction Zone. **(A)** Broadscale tectonics associated with the Cascadia Subduction Zone. **(B)** Map of Barkley Sound and the Alberni Inlet connecting the Port Alberni field site to the Pacific Ocean. **(C)** Location of Port Alberni, British Columbia and **(D)** Willapa Bay, Washington with major geomorphological features indicated.

3.3.2. Port Alberni, British Columbia, Canada

Although located close to the geographical center of Vancouver Island, 180 km from the Cascadia ocean trench, Port Alberni is a coastal city connected to the Pacific Ocean via the Alberni Inlet. The Alberni Inlet is a 38-km-long, narrow (~ 500 – 2500 m), drowned glacial valley that connects Port Alberni to the Barkley Sound and the open Pacific Ocean. The surrounding bedrock geology of Port Alberni and the inlet is primarily composed of Late Triassic Karmutsen basalt and Quatsino limestone of the Wrangellia Terrane (DeBari et al., 1999; Massey & Friday, 1988). The Somass River flows into the head of Alberni Inlet, which is fringed by small salt marshes because of the broad tidal flats and dampened-wave energy characteristic of this area.

The Port Alberni salt marsh examined as part of this study is located at the confluence of the Somass River and the Alberni Inlet. At this location, the river crosses the eastern edge of the marsh and a large tidal channel separates the marsh from the mountainous inlet to the west. The tidal range at this location is 2.59 m (difference between mean higher high water and mean lower low water) (Fisheries and Oceans Canada [DFO], 2023). The Port Alberni salt marsh is part of the traditional territory of the Tseshaht First Nation and was historically used as a site for obtaining medicinal plants (Tseshaht First Nation, n.d.). The east side of the salt marsh has been anthropogenically altered by the establishment of the city's wastewater treatment plant in the 1950s and the historical logging industry that began in earnest in the 1860s and has since decreased (Alberni Valley Museum, 2011).

Despite being close to anthropogenically-influenced areas, the Port Alberni salt marsh is among the few large and easily accessible salt marshes in northern Cascadia. The marsh at this location is not as laterally extensive or well-developed as those in Willapa Bay (up to 200 m wide at Port Alberni vs. up to 1000 m wide at Willapa Bay); however, vascular vegetation differentiates distinct environmental zones within the marsh that is similar to the vegetation zonation at other coastal marshes in Cascadia (e.g., Hawkes et al., 2010; Hong et al., 2021; Milker et al., 2015; Riou, 2023).

Riou (2023) documents five environmental zones within the Port Alberni marsh based on vegetation: subtidal, tidal flat, low marsh, high marsh, and wooded uplands. The subtidal zone seaward of the marsh is characterized by sediment-infilled deep rocky

tidal channels that lack vascular vegetation. The tidal flat proximal to the marsh is 5 – 40 m wide and is dominated by clastic mud with trace amounts of seagrass (*Zostera* sp). The low marsh is characterized by peaty mud and denser stands of salt marsh vegetation including rushes (*Juncus* sp.) and sedges (*Carex lyngbei*). By contrast, the high marsh generally contains saltgrass (*Distichlis spicata*) with lower amounts of silverweed (*Potentilla pacifica*), perennial herbaceous plants (*Symphyotrichum subspicatum*, *Cirsium arvense*), sedges (*Scirpus americanus*), and wild rose (*Rosa nutkana*). The wooded upland environment is entirely outside the upper limit of tides and is dominated by coniferous and deciduous trees that are not saltwater tolerant (Pojar & MacKinnon, 1994; Riou et al. 2023).

3.3.3. Willapa Bay, Washington, USA

Willapa Bay is a drowned river valley that is protected from the Pacific Ocean by a 26-km-long barrier spit composed of sediment derived from the Columbia River (Emmett et al., 2000; Engelhart et al., 2015). The local geology is primarily composed of unconsolidated Quaternary sediments, Neogene Columbia River basalts, and Miocene Astoria sedimentary formations. The marshes at Willapa Bay are approximately 140 km from the Cascadia ocean trench and have been subjected to coseismic subsidence during large prehistoric earthquakes (e.g., Atwater, 1987; Atwater & Hemphill-Haley, 1997; Hemphill-Haley, 1995). The tidal channels crossing Willapa Bay are protected from waves by the barrier spit, resulting in low-energy environments that favour salt marsh development. Tides at Willapa Bay are mixed semidiurnal with a range that varies from north to south: in northern Willapa Bay (Smith Creek, Bone River, Niawiakum River), the tidal range is 2.8 m, while in southern Willapa Bay (Naselle River), the tidal range is 3.3 m (National Oceanic and Atmospheric Administration [NOAA], 2023).

The distribution of macroplant vegetation within Willapa Bay has been used to distinguish five different environmental zones according to Hong et al. (2021): subtidal, tidal flat, low marsh, high marsh, and wooded upland. The subtidal zone is dominated by deep tidal channels that are devoid of vascular vegetation, while the tidal flat is predominately composed of mud with sparse amounts of seagrass (*Zostera* sp). The low marsh is dominated by cordgrass (*Spartina alterniflora*), pickleweed (*Salicornia virginica*), marsh janumea (*Jaumea carnosa*), sea milkwort (*Glaux maritima*), and arrowgrass (*Triglochin maritima*); the high marsh is dominated by sedges (*Carex*

lyngbyei), tufted hairgrass (*Deschampsia caespitosa*), saltgrass (*Distichlis spicata*), rushes (*Juncus balticus*), and silverweed (*Potentilla pacifica*). The wooded upland is markedly different from the marsh in terms of vegetation type and density and is characterized by freshwater plants such as Sitka spruce (*Picea sitchensis*) and deciduous trees such as crabapple (*Pyrus fusca*).

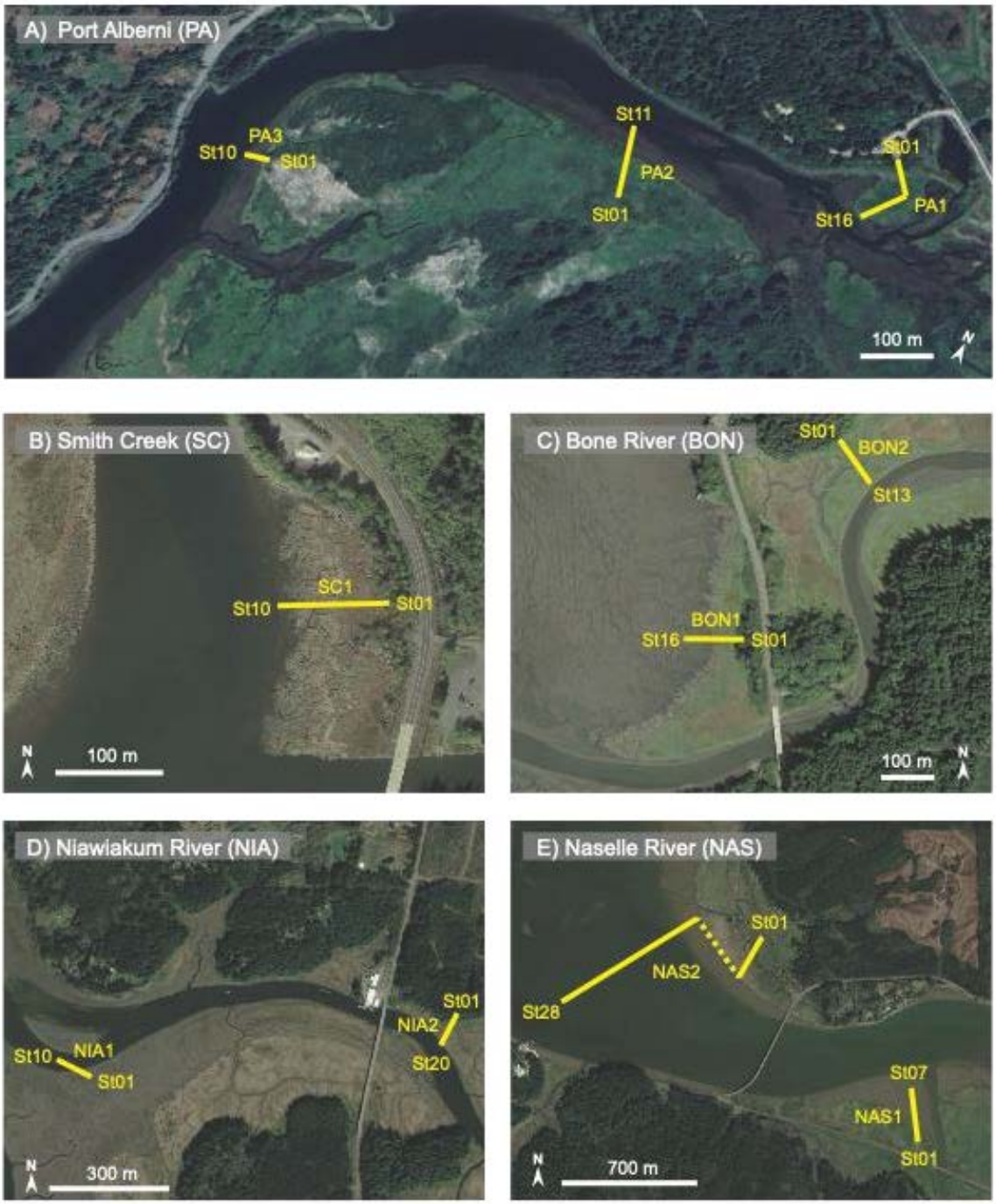

Figure 3-2 Location of Surface Sediment transects at Port Alberni and Willapa Bay. **(A)** Port Alberni with sampling transects marked with yellow lines. **(B)** Smith Creek with sampling transects marked with yellow lines. **(C)** Bone River with sampling transects marked with yellow lines. **(D)** Naselle River with sampling transects marked with yellow lines. **(E)** Niawiakum River with sampling transects marked with yellow lines.

3.4. Methods

3.4.1. Surface Sediment Sample Collection

A total of 10 marsh transects were sampled: Port Alberni (3 transects, 37 stations) and Willapa Bay (7 transects, 104 stations). The transects captured different marsh zones delineated by macroplants (Figure **3-2**; subtidal, tidal flat, low marsh, high marsh, upland). Surface sediment samples used for XRF analysis were collected by Riou (2023) at Port Alberni and Hong et al. (2021) at Willapa Bay. They reported on the modern distributions of foraminifera/testate amoebae and diatom assemblages. At both locations, surface sediments (~20 cm^3 of the upper 2 cm of sediment) were sampled at consistent vertical intervals (approximately every 10 – 20 cm in elevation change), except where vegetation or tidal elevation abruptly changed, in which case additional stations were added.

At Port Alberni, the elevation of each station was measured using a Spectra SP80 Real Time Kinematic-Global Navigation Satellite System (RTK-GNSS) referenced to the Port Alberni benchmark 59C9001 and related to chart datum (Riou, 2023). The elevations of each sample station were referenced to mean tide level (MTL) using hourly water level observations from 2011–2022 provided by Fisheries and Oceans Canada (Fisheries and Oceans Canada [DFO], 2023). At Willapa Bay, elevations for each station were obtained using a Leica GS-15 Real Time Kinematic-Global Positioning System (RTK-GPS) and a total station referenced to the North American Vertical Datum (NAVD88). Measured elevations were referenced to MTL using the VDatum transformation software (Hong et al. 2021). Tidal elevations from both field sites were converted to a standardized water level index (SWLI), which allows for comparison between sites that have different tidal ranges (mean tidal level [MTL] has a SWLI value of 100)

Table 3-1 – Summary of transects (location, stations, and sampled environment) from Port Alberni (Riou, 2023) and Willapa Bay (Hong et al. 2021)

Transect ID	Total number of stations	Environmental gradient sampled
Port Alberni 1	16	Tidal Flat to High Marsh
Port Alberni 2	11	Tidal Flat to High Marsh

Port Alberni 3	10	Tidal Flat to High Marsh
Smith Creek 1	10	Tidal Flat to High Marsh
Bone River 1	16	Tidal Flat to High Marsh
Bone River 2	13	High Marsh
Niawiakum River 1	10	Subtidal to Tidal Flat
Niawiakum River 2	20	Tidal Flat to High Marsh
Naselle River 1	7	Low Marsh to High Marsh
Naselle River 2	28	Tidal Flat to Upland

3.4.2. X-ray Fluorescence (XRF) Analysis

The elemental composition of each surface sediment sample collected by Riou (2023) and Hong et al. (2021) was analyzed using an ITRAX XRF Core Scanner at Simon Fraser University. Because the XRF-CS was designed for the analysis of split cores, sequential sample reservoirs (SSRs), holding devices that can accommodate 25 discrete surface samples, were used to house individual samples for XRF analysis (e.g., Gregory et al., 2017; Kovacs et al., 2017; Patterson et al., 2020; Steele et al., 2018). Prior to analysis, approximately 5 cm^3 of surface sediment from all 141 stations at Port Alberni and Willapa Bay were first prepped and then loaded into the SSRs following the methods of Gregory et al. (2017) (Figure **3-3**). Prior to loading sediment into the SSRs, samples were dried at 50°C in a drying oven and ground into a fine powder using a mortar and pestle before minimal amounts of deionized water were added to create a homogenized moist paste texture.

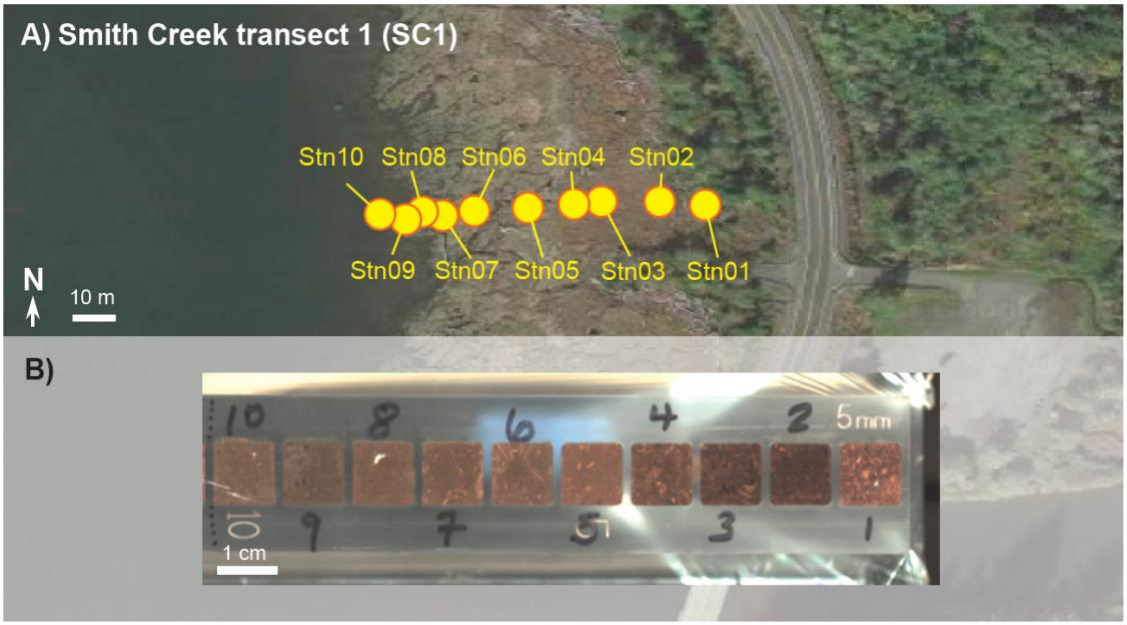

Figure 3-3 Example of surface sediment in sequential sample reservoirs (SSR) **(A)** Smith Creek transect 1 (SC1) with station labelled. **(B)** SC1 surface samples prepared and loaded into SSR for XRF analysis on the ITRAX-CS.

A molybdenum (Mo) x-ray tube was used to obtain XRF measurements for all surface samples on the ITRAX-CS using the following parameters: 30 kV, 55 mA, 10 second count time per analyzed interval. SSRs were scanned at a resolution of 0.1 mm, resulting in 100 measurements per sample. Within each sample reservoir, the uppermost and bottommost 1 mm of measurements (a total of 20 measurements per surface sample) were removed during post-processing so that only the middle 80 measurements were used in analysis. These “edge” measurements, where there is a sudden topographic change between the wall of the SSR and the sample surface can be unreliable because the detector may not be at the optimal measurement position due to subtle topographic changes as it passes over the SSR during analysis (Gregory et al., 2017).

Of the 23 elements detected by the ITRAX-CS, only eight with the highest counts per second (Fe, Ca, Ti, Br, K, Mn, Sr, Si) were considered in order to avoid interpreting elements with low counts per second as variations may reflect specimen or matrix effects (e.g., Chagué-Goff et al., 2016). In addition to individual elements, the incoherent/coherent scattering ratio (ICR) of each sample measurement was also measured. Incoherent (Compton / inelastic) scattering results when a high energy incident photon (x-ray) collides with and ejects an electron from an atomic nucleus,

resulting in a transfer of energy and a decrease in the energy of a photon (Fernández, 1992). Coherent (Rayleigh / elastic) scattering occurs when an incident photon (x-ray) interacts with an atom, but does not have sufficient energy to eject the electron from the orbital, leading to no change in photon energy (Fernández, 1992).

Whether a photon experiences incoherent or coherent scattering is related to the binding energy of a target electron, which tends to be less for lower atomic number elements (Croudace et al., 2006; Fernández, 1992). Incoherent scattering has lower energy than that of the x-ray tube, while coherent scatter has the same energy. Prior to statistical analysis, elemental counts were normalized to the ICR to correct for variations in sediment moisture, organic content, and instrumental effects (e.g., Chagué-Goff et al., 2016; Gregory et al., 2019; Kaboth-Bahr et al., 2019; Oliva et al., 2018). For each station, the mean of all 80 ICR-normalized elemental values was determined to simplify the dataset and account for sample heterogeneity (e.g., Gregory et al., 2017).

3.4.3. Statistical Analysis

Statistical methods (i.e., PAM cluster analysis, Adjusted Rand Index, and Principal Component Analysis) were applied to post-processed XRF data to investigate the relationship between elemental geochemistry and tidal frequency. All statistical analyses were performed using the R software (R Core Team, 2021), including the packages tidyverse, cluster, factoextra, and ggpubr.

Cluster analysis is commonly used in sea-level studies to determine how microfossil assemblages vary with tidal elevation (e.g., Engelhart et al., 2013; Walker et al., 2020; Zong & Horton, 1998). The Adjusted Rand Index (ARI) builds on results from cluster analysis by comparing two distinct clusters and quantifying the similarity between elemental geochemistry and microfossil composition (e.g., Heil et al., 2019; Snelder & Booker, 2013). Principal Component Analysis (PCA) is a method to reduce the dimensionality of multivariate datasets in order to simplify general trends and has been applied in XRF-CS studies to identify processes driving elemental variation (e.g., Kaboth-Bahr et al., 2019; López Pérez et al., 2019; Peti et al., 2019).

To assess the applicability of elemental geochemistry as a sea/land-level indicator, normalized and averaged XRF data were first clustered to reveal groupings

within the data and then compared to the clustered microfossil data of Riou et al. (2023) and Hong et al. (2021). Partitioning Around Medoids (PAM) cluster analysis was used to identify geochemical clusters (Kaufman & Rousseeuw, 1990; e.g., Engelhart et al., 2013; Khan et al., 2019; Pilarczyk et al., 2020; Walker et al., 2020). PAM cluster analysis is a variation of k-means clustering, in which groups are identified based on a representative medoid (a datapoint from the dataset) and other data points are assigned to the closest medoid based on similarity (Kaufman & Rousseeuw, 1990). Unlike k-means clustering that uses a centroid (virtual datapoint), PAM analysis uses a medoid (actual datapoint from the dataset) and is therefore less sensitive to outliers within the dataset (MacQueen, 1967). Silhouette plots were used to graphically represent PAM clustering results by assigning each sample a silhouette width value between -1 and 1, where values close to 1 indicate the sample is appropriately assigned to the cluster, and values close to -1 are not appropriately assigned to their respective cluster (Rousseeuw, 1987). To determine the optimal number of clusters, multiple scenarios were considered using one to six clusters. The clustering scenario with the largest overall average silhouette width was used for comparison with microfossil datasets.

Following PAM cluster analysis, the Adjusted Rand Index (ARI), a measure of similarity between two clustered datasets (Hubert & Arabie, 1985), was used to compare microfossil and geochemical clusters. We applied the ARI to quantify the similarity between the observed clusters (i.e., environmental zones as described by vascular vegetation) and the geochemical or microfossil clusters. For the observed clusters, each station is assigned a value based on its zone of collection (tidal flat assigned value of 1, low marsh 2, etc.), while geochemical and microfossil clusters are assigned on the basis of the clustering results. ARI values of 1 indicate strong agreement, values of 0 indicate random agreement, and values of -1 indicate strong disagreement (Hubert & Arabie, 1985).

Principal Component Analysis (PCA) was applied to the entire geochemical dataset to reduce the dimensionality and provide insight into the elemental variables driving data separation. Prior to PCA analysis, the elemental dataset was scaled such that all variables had a mean of zero and a standard deviation of one. The principal components (PCs) were axes that describe the most variation within the data, which helps to simplify large complex datasets while retaining patterns and trends (e.g., Kaboth-Bahr et al., 2019; Peti et al., 2019). The cumulative variation in variance for all

transects was determined for up to four principal components, which, in turn, explained the cumulative variance captured as additional principal components were added (e.g., Hong et al. 2021). The cumulative variation provided insights into the amount of information from the original dataset that was retained when the dimensionality was reduced. The elemental variable vectors assisted in determining which elements influenced the separation along the principal components (e.g., Hong et al., 2021).

3.5. Results

3.5.1. General Geochemical Trends within Cascadia Salt Marshes

We collected 141 samples from 10 transects at two sites: the Port Alberni and Willapa Bay salt marshes. Transects were selected so that stations encompassed the full intertidal gradient from the tidal flat to the high marsh. The two exceptions to this sampling strategy are NIA1, which spans the subtidal and tidal flat environments, and BON2, which is limited to samples from the high marsh only.

In total 23 elements were detected by XRF analysis, of which 8 (Fe, Ca, Ti, Br, K, Mn, Sr, Si) exceeded an arbitrary average raw threshold of 15,000 kcps and were therefore used for multivariate analyses (e.g., Chagué-Goff et al., 2016). Although Ca and Mn abundances exceed the kcps threshold, they were not considered for statistical analysis. Ca was omitted because of its anomalously large values in some subtidal and tidal flat stations, which skewed the elemental composition such that PAM analysis would result in an isolated individual cluster for that station. The large Ca concentrations along the transects may be due to the distribution of carbonate shells in the subtidal zone and tidal flat and may not be representative of the bulk sediment composition. Both Fe and Mn are redox sensitive elements, but only Fe was considered because it has the largest abundance of all the elements and is considered less redox-sensitive (and therefore less mobile) compared to Mn (e.g., Davison, 1993).

In general, low elevation samples from the tidal flat are characterized by high abundances of lithogenic (Si, K, Ti, Fe) and biogenic (Sr) elements, while high elevation samples from the high marsh are characterized by high values of Br and ICR. This general trend is most apparent in transects that span the full marsh gradient but does

show minor local variations between Port Alberni and Willapa Bay as documented in sections 3.5.2 and 3.5.3.

Table 3-2 – Summary of PAM cluster analysis with average silhouette widths of each clustered scenario

Transect	Cluster 1	Cluster 2	Cluster 3	Cluster 4	Overall Avg Sil
Port Alberni 1	0.40	0.60	0.48	-	0.51
Port Alberni 2	0.45	0.62	-	-	0.51
Port Alberni 3	0.66	0.23	-	-	0.58
Smith Creek 1	0.68	0.50	-	-	0.56
Bone River 1	0.59	0.49	-	-	0.55
Bone River 2	0.56	0.39	-	-	0.53
Niawiakum River 1	0.40	0	0.34	-	0.34
Niawiakum River 2	0.65	0.60	0.30	-	0.58
Naselle River 1	0.64	0.70	-	-	0.68
Naselle River 2	0.49	0.70	0.25	0.83	0.54
Port Alberni Regional	0.59	0.52	0.53	-	0.56
Willapa Bay Regional	0.43	0.50	0.25	-	0.42
All	0.46	0.38	-	-	0.43

Table 3-3 – Summary of Adjusted Rand Index (ARI) values comparing similarities between observed environmental zones, geochemical clusters, and microfossil clusters

Transect	Adjusted Rand Index (ARI)	
	Elemental Composition - Observed Zones	Microfossils - Observed Zones
Port Alberni 1	0.25	0.57
Port Alberni 2	0.63	0.62
Port Alberni 3	0.37	1
Smith Creek 1	0.22	0.59
Bone River 1	0.45	1
Bone River 2	-	-
Niawiakum River 1	0.40	0.05
Niawiakum River 2	0.1	0.45
Naselle River 1	0.05	1
Naselle River 2	0.44	0.66

Table 3-4 – Summary of PCA results (cumulative variance [%]) for principal components (PC) explained by elemental variables

Transect	Cumulative Variance (%)			
	PC 1	PC 2	PC 3	PC 4
Port Alberni 1	0.82	0.95	0.98	0.99
Port Alberni 2	0.84	0.94	0.97	0.99
Port Alberni 3	0.72	0.97	0.98	0.99
Smith Creek 1	0.85	0.95	0.98	1
Bone River 1	0.80	0.97	0.99	0.99
Bone River 2	0.88	0.96	0.98	0.99
Niawiakum River 1	0.63	0.86	0.93	0.97
Niawiakum River 2	0.89	0.96	0.98	1
Naselle River 1	0.91	0.98	0.99	1
Naselle River 2	0.71	0.93	0.97	0.99
Port Alberni Regional	0.83	0.95	0.97	0.99
Willapa Bay Regional	0.71	0.91	0.95	0.98
ALL	0.72	0.87	0.94	0.97

3.5.2. Geochemical Composition of Port Alberni Transects

Port Alberni Transect 1 (PA1)

Port Alberni transect 1 (Figure **3-4**) extends for 114 m perpendicular to the shoreline and consists of 16 surface sediment samples (i.e., stations) that span the tidal flat, low marsh, and high marsh with an elevation range of 95.6 to 283.6 SWLI (0.95 m to 3.26 m above MTL). In general, lithogenic (Si, K, Ti, Fe) and biogenic (Sr) elements dominate in samples collected from the tidal flat and progressively decreased with increasing elevation and distance landward. By contrast, Br and ICR were most abundant in the high marsh and decreased with decreasing elevation and distance seaward (Figure **3-4**A).

PAM cluster analysis was used to identify geochemical groups of samples along the transect. We modelled a spectrum of clustering scenarios ranging from one to six clusters. For PA1, a three-cluster scenario produced the highest overall average silhouette width of 0.51 (Figure **3-4**BC), as opposed to the two- and four-cluster scenarios that resulted in lower overall average silhouette widths of 0.47 and 0.42, respectively. Cluster A in the three-cluster scenario includes stations from the lowest

elevations in the marsh, within the tidal flat and low marsh areas (Stn01–Stn05). The average silhouette width of Cluster A is 0.40, with stations having an elevation range of 95.9–143.4 SWLI and a mean of 116.3 ± 19.4 SWLI. This is in contrast to Cluster B, which includes stations located from the landward limit of the low marsh to the high marsh zones (Stn06 – Stn12, Stn16). The average silhouette width of this cluster is 0.60, with stations representing an elevation range of 163.5–283.6 SWLI and a mean of 208.5 ± 33.6 SWLI. Cluster C, containing the fewest stations collected from the high marsh (Stn13 – Stn15) had an average silhouette width of 0.48 and an elevation range of 223.5–261.4 SWLI and a mean of 240.3 ± 19.3 SWLI.

PCA shows that the elemental variables drive separation in an orientation that is consistent with the PAM cluster results. The spread of the elemental dataset captured within principal component 1 (PC1) and principal component 2 (PC2) represents the variance of the data that remains after reducing the dataset to two dimensions. PC1 captures 82.4% of the total variance of the dataset, while PC2 accounts for 12.7% of the variance (Figure **3-4**C). Variables driving separation along PC1 include ICR and Br in the positive direction and Si, Sr, Ti, and K in the negative direction (Figure **3-4**D). Separation along PC2 is controlled by Br and Fe. The direction and orientation of these elemental vectors (Figure **3-4**D) are plotted in the same PC-space as the PAM clusters (Figure **3-4**C) and can be compared with one another to determine which elements are driving separation in each cluster. For example, Cluster A is the most negative cluster along the horizontal PC1 axis (Figure **3-4**C) and coincides with elemental vectors Si, Ti, K, Fe, and Sr, which are oriented in the negative PC1 direction (Figure **3-4**D). Cluster C is the most positive cluster along PC1 and coincides with elemental vectors Br and ICR that are oriented in the positive PC1 direction. These results suggest that cluster separation within the geochemical dataset is driven by elemental vectors that are oriented in same direction.

Port Alberni Transect 2 (PA2)

Port Alberni transect 2 (Figure **3-5**) is 125 m in length and consists of 11 surface sediment samples spanning the tidal flat, low marsh, and high marsh environments with an elevation range of 48.7 to 242.1 SWLI (0.4 m to 2.6 m above MTL). Lateral elemental trends at PA2 are similar to those at PA1, with lithogenic (Si, K, Ti, Fe) and biogenic (Sr)

elements most abundant at low elevations and Br and ICR dominant at high elevations (Figure **3-5**A).

PAM cluster analysis on the XRF data from PA2 identified two optimal clusters with an overall average silhouette width of 0.51 (Figure **3-5**BC). Cluster A is characterized by stations from the tidal flat and low marsh environments (Stn01 – Stn07). The average silhouette width of Cluster A is 0.45, with stations having an elevation range of 48.7–163.7 SWLI and a mean of 96.6 ± 39.0 SWLI. Cluster B contains higher elevation stations, all of which were collected from the high marsh environment. Cluster B has an average silhouette width of 0.62 with stations having an elevation range of 195.2–242.1 SWLI and a mean of 220.6 ± 20.6 SWLI.

PC1 explains 83.9% of the total variance, and Br and ICR are driving separation in the positive direction while Si, K, Ti, Fe, and Sr control separation in the negative direction. PC2 accounts for 9.7% of the elemental variance and is most influenced by Fe because its vector is most parallel to PC2 (Figure **3-5**D). The relationship between elemental clusters and elemental variables in PC-space at PA2 is similar to PA1, where the lower elevation cluster is associated with lithogenic (Si, K, Ti, Fe) and biogenic elements (Sr) and the higher elevation cluster is related to Br and ICR.

Port Alberni Transect 3 (PA3)

Port Alberni transect 3 (Figure **3-6**) is 34 m in length and consists of 10 surface sediment samples from the tidal flat, low marsh, and high marsh, with an elevation range of 62.2 to 200.7 SWLI (0.5 m to 2.2 m above MTL). General elemental trends at PA3 are similar to PA1 and PA2, with lithogenic elements (Si, K, Ti, Fe) most prevalent at low elevations and Br and ICR most abundant at high elevations. The exception is Sr, which in PA3 is most abundant at intermediate elevation (i.e., low marsh) rather than at either extreme (i.e., tidal flat or high marsh) (Figure **3-6**A).

PAM cluster analysis identified two optimal clusters with an overall average silhouette width of 0.58 (Figure **3-6**BC). Cluster A includes all lower elevation stations from the tidal flat and low marsh environments (Stn01 – Stn08). The average silhouette width of Cluster A is 0.66, with stations spanning an elevation range of 62.2–145.9 SWLI and a mean of 93.5 ± 31.3 SWLI. Cluster B includes high elevation samples from the high marsh? environment (Stn09–Stn10). The average silhouette width of Cluster B is

0.23 with stations having an elevation range of 176.5–200.7 SWLI and a mean of 188.61 ± 17.1 SWLI.

PC1 explains 72.3% of the total variance and is driven by Br and ICR in the positive direction and Ti, Si, and Sr in the negative direction. Unlike the other two PA transects, K and Fe have a greater contribution to PC2 than PC1, accounting for 24.3% of the variance (Figure **3-6**D).

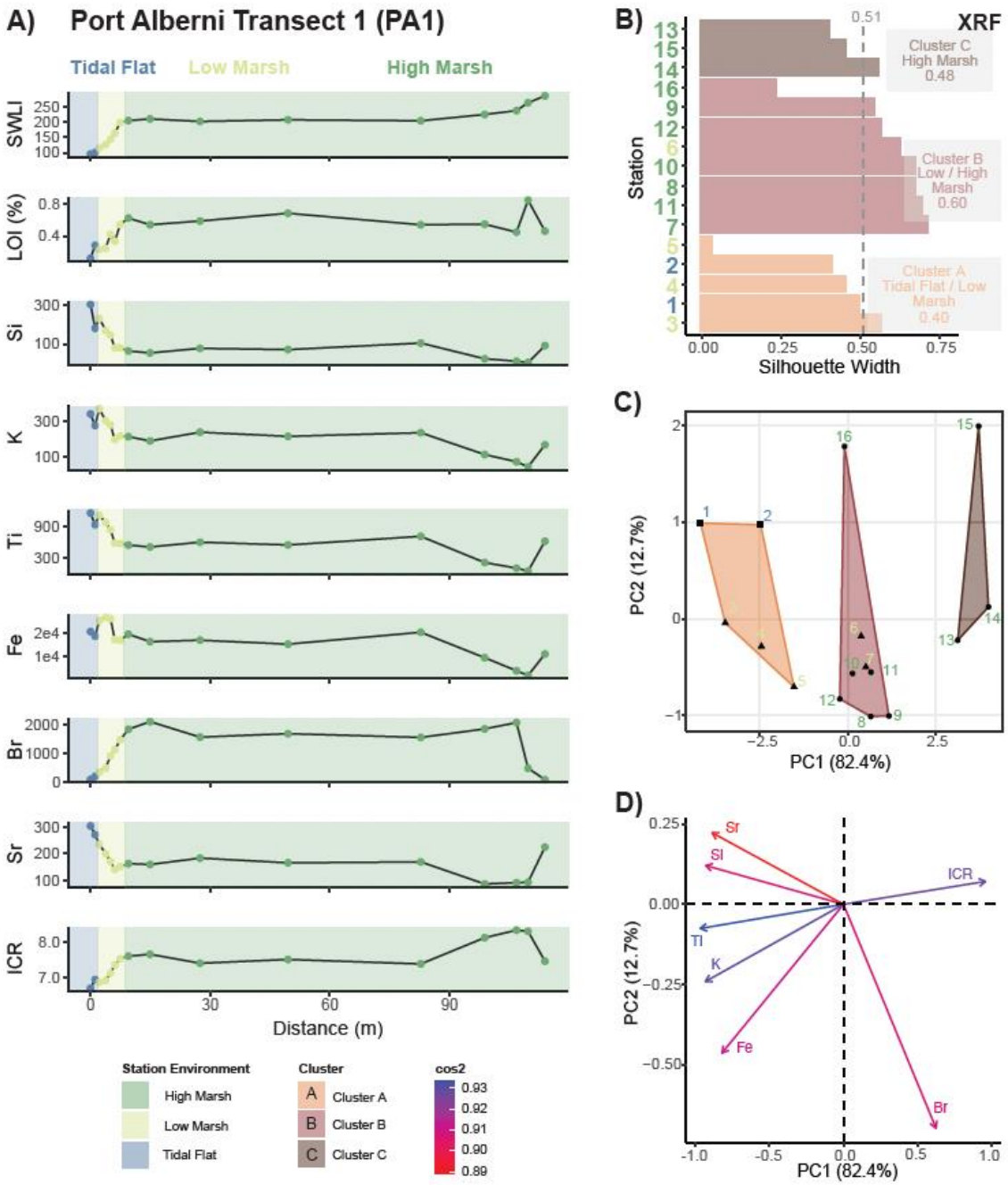

Figure 3-4 Elemental geochemical data for Port Alberni transect 1 (PA1). **(A)** Elemental abundances (normalized to ICR) along the transect. **(B)** PAM cluster silhouette widths for elemental composition. **(C)** PAM cluster plotted in the dimensions of principal component 1 and principal component 2. **(D)** PCA loading vectors (elemental variables) along principal component 1 and principal component 2

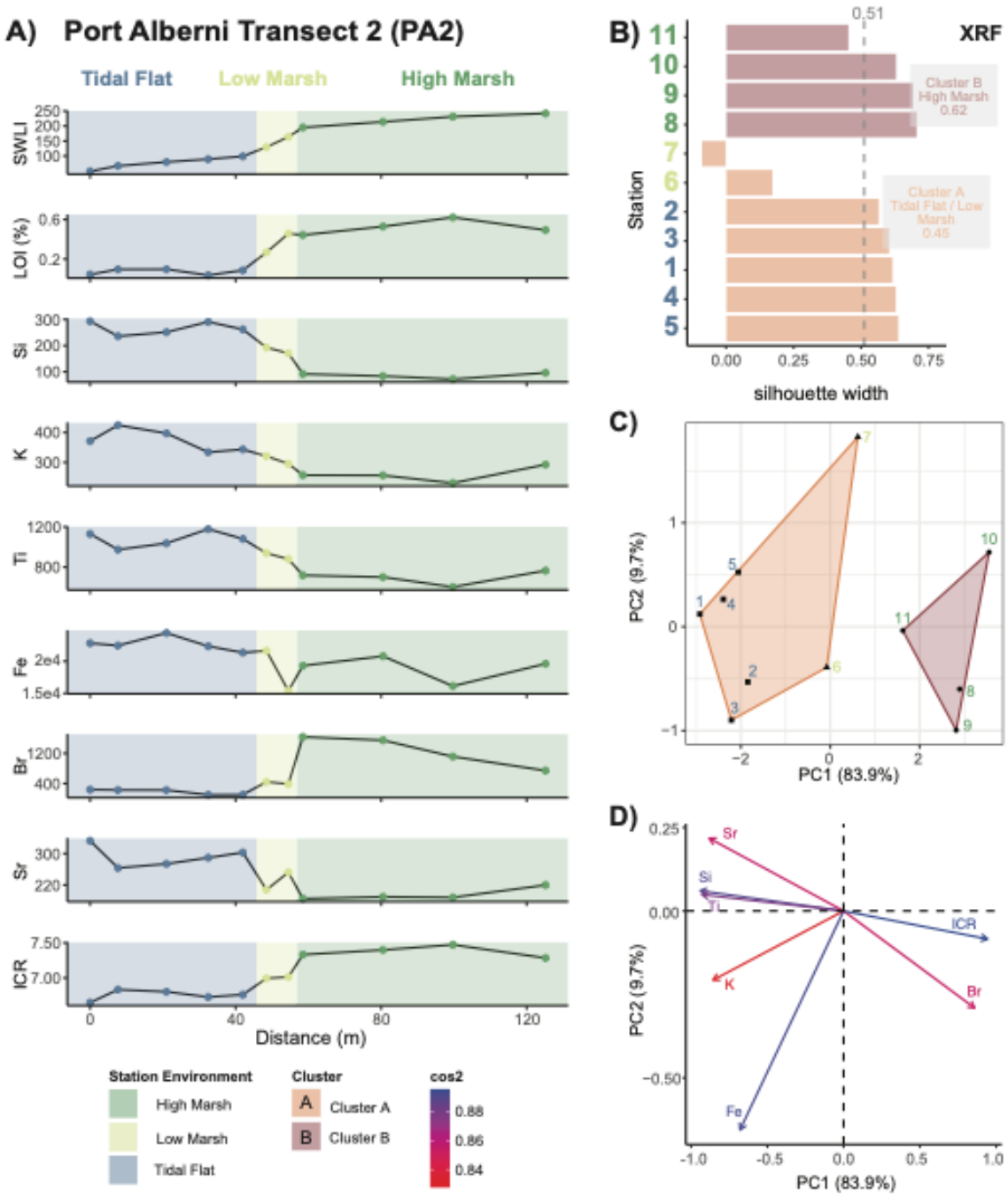

Figure 3-5 Elemental geochemical data for Port Alberni transect 2 (PA2). **(A)** Elemental abundances (normalized to ICR) along the transect. **(B)** PAM cluster silhouette widths for elemental composition. **(C)** PAM cluster plotted in the dimensions of principal component 1 and principal component 2. **(D)** PCA loading vectors (elemental variables) along principal component 1 and principal component 2.

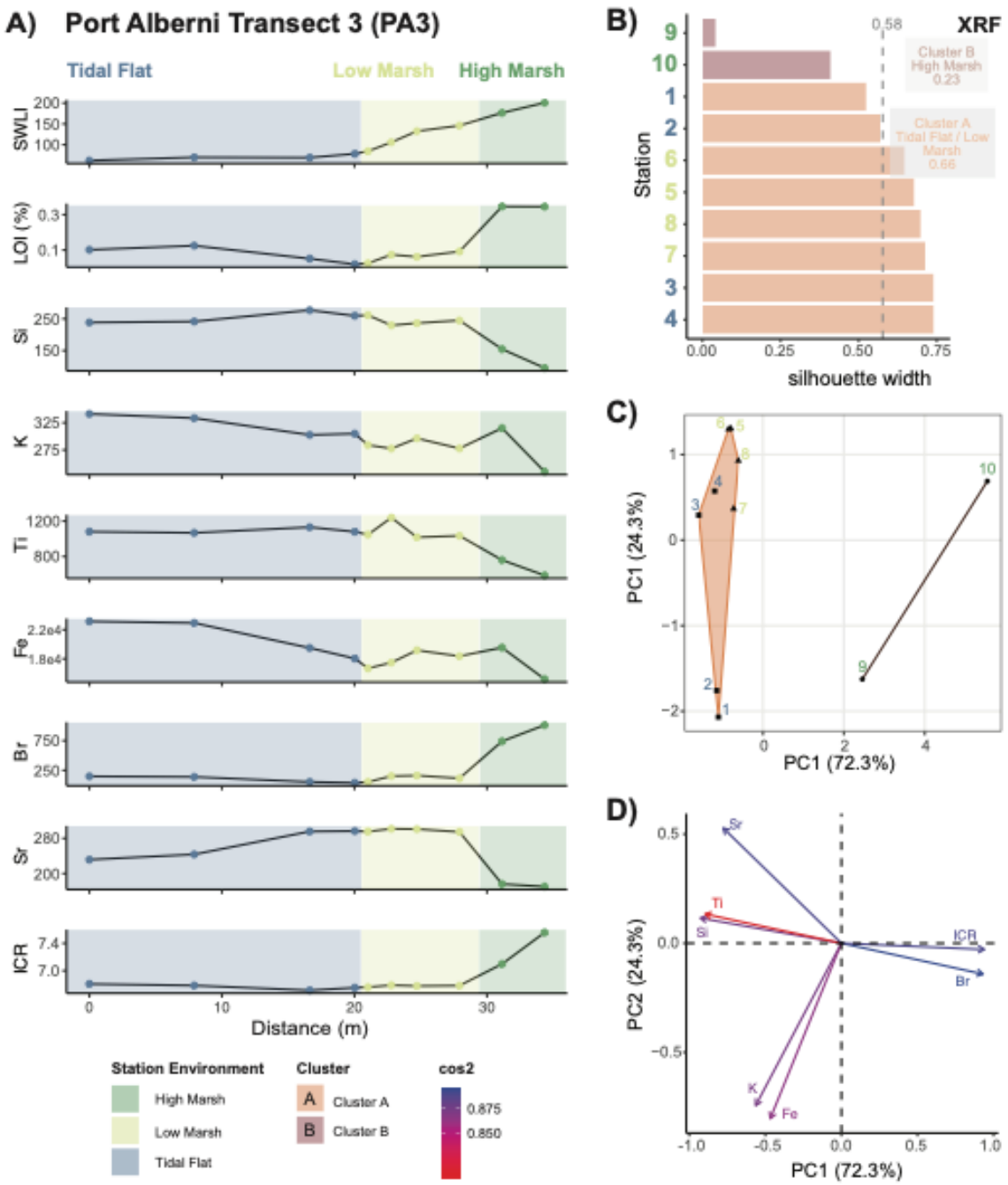

Figure 3-6 Elemental geochemical data for Port Alberni transect 3 (PA3). **(A)** Elemental abundances (normalized to ICR) along the transect. **(B)** PAM cluster silhouette widths for elemental composition. **(C)** PAM cluster plotted in the dimensions of principal component 1 and principal component 2. **(D)** PCA loading vectors (elemental variables) along principal component 1 and principal component 2

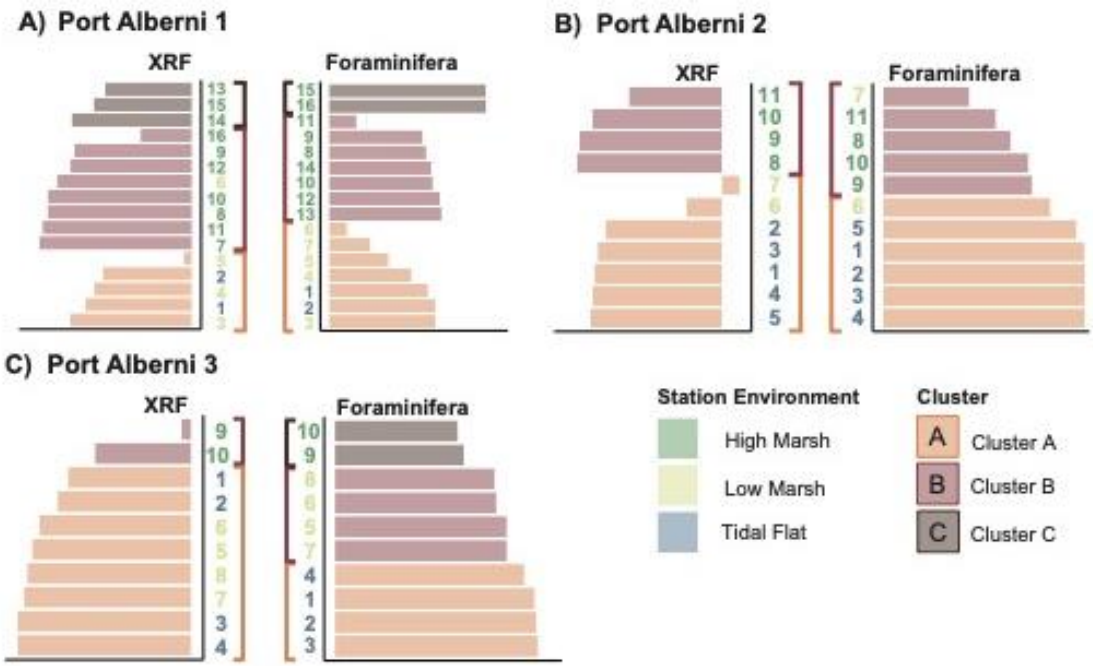

Figure 3-7 Comparison between elemental geochemistry PAM clustering and foraminifera PAM clustering for Port Alberni transects (Riou, 2023). **(A)** Port Alberni transect 1. **(B)** Port Alberni transect 2. **(C)** Port Alberni transect 3.

3.5.3. Geochemical Composition of Willapa Bay Transects

Smith Creek Transect 1 (SC1)

Smith Creek transect 1 (Figure **3-8**) is 107 m long and consists of 10 surface sediment samples from the tidal flat, low marsh, and high marsh, with an elevation range of 86.0 to 224.3 SWLI (-0.18 m to 1.60 m above MTL). Elemental trends at SC1 are similar to those at Port Alberni, with lithogenic (Si, K, Ti, Fe) and biogenic (Sr) elements most abundant at the lowest elevations and least abundant at higher elevations. Br and ICR trends are also consistent with Port Alberni, having the largest values at high elevations and decreasing as elevations lower (Figure **3-8**A).

PAM cluster analysis identified two optimal clusters with an overall average silhouette width of 0.56 (Figure **3-8**BC). Cluster A consists of the lower elevation stations from the tidal flat, low marsh, and the lowest elevation high marsh station (Stn01–Stn07). The average silhouette width of Cluster A is 0.50, representing an elevation range of 86.1–205.7 SWLI and a mean of 149.7 ± 40.2 SWLI. Cluster B contains the three highest elevation stations from the high marsh environment (Stn08–Stn10). The average

silhouette width of Cluster B is 0.68, with and an elevation range of 211.3–224.3 SWLI with a mean of 220.8 ± 8.3 SWLI.

PC1 accounts for 85.3% of the total variance and shows that Br and ICR drive elemental separation in the positive direction, while Si, Ti, K, and Sr are oriented in the negative direction. PC2 accounts for 10.1% of the remaining variance and is strongly controlled by Fe (Figure **3-8**D).

Bone River Transect 1 (BON1)

Bone River transect 1 (Figure **3-9**) is 112 m in length and consists of 16 surface sediment samples that span the tidal flat, low marsh, and high marsh, with an elevation range of 139.3 to 256.3 SWLI (0.50 m to 1.99 m above MTL). Similar to previous transects, the elemental trends at BON1 show lithogenic and biogenic elements most abundant at low elevations and Br and ICR most abundant at high elevations. Unlike previous transects, Fe at BON1 has the highest values at intermediate elevations rather than either extreme (Figure **3-9**A).

PAM cluster analysis identified four optimal clusters with an overall average silhouette width of 0.55 (Figure **3-9**BC). Cluster A contains the lower elevation stations from the tidal flat and low marsh environments (Stn01–Stn10). The average silhouette width of Cluster A is 0.59, representing an elevation range of 139.3–212.9 SWLI and a mean of 170.3 ± 28.1 SWLI. Cluster B contains the highest elevation, low marsh station and all the high marsh stations (Stn11–Stn16). The average silhouette width of Cluster B is 0.49, representing an elevation range of 223.3–256.3 SWLI and a mean of 243.5 ± 13.7 SWLI.

PC1 explains 79.9% of the total variance, with Br, ICR, and Fe driving the positive direction, whereas Si, K, Ti, and Sr account for separation in the negative direction. This transect shows Fe in the positive PC1 direction, but Fe still contributes more to PC2, which accounts for 17.6% of the remaining variance (Figure **3-9**D).

Bone River Transect 2 (BON2)

Bone River transect 2 (Figure **3-10**) is 109 m long and consists of 13 surface sediment samples, all from the high marsh, with an elevation range of 207.1 to 218.1 SWLI (1.4 m to 1.5 m above MTL). Despite the fact that all samples are from the high

marsh environment, BON2 still shows similarity with other transects in terms of elemental distributions. Lithogenic (Si, K, Ti, Fe) and biogenic (Sr) elements are abundant at lower elevations, and Br and ICR are abundant at the higher elevations (Figure **3-10**A).

PAM cluster analysis identified two optimal clusters with an overall average silhouette width of 0.53 (Figure **3-10**BC). Cluster A contains the ten most seaward high marsh samples (Stn01 – Stn10), while Cluster B contains the three most landward high marsh samples (Stn11 – Stn13). The average silhouette width of Cluster A is 0.56, with an elevation range of 207.1–218.1 SWLI and a mean of 208.5 ± 5.3 SWLI. The average silhouette width of Cluster B is 0.39, with an elevation range of 219.9–228.9 SWLI and a mean of 223.4 ± 13.7 SWLI. BON2 clusters show stations are sequentially ordered which demonstrates elemental separation even within the same high marsh environmental zone.

PC1 explains 87.8% of the total variance, with Br and ICR driving separation in the positive direction and Si, K, Ti, Fe, and Sr in the negative direction. PC2 accounts for 8.6% of the remaining elemental variance, with Sr the dominate element driving separation along PC2 (Figure **3-10**D). PCA results from BON1 (Figure **3-9**) show the same elemental variables driving separation in the positive PC1 direction (Si, K, Ti, Fe, Sr) and the negative PC1 direction (Br, ICR) when compared to BON2 despite capturing a more complete elevation gradient.

Niawiakum River Transect 1 (NIA1)

Niawiakum River transect 1 (Figure **3-11**) is 111 m in length and consists of 10 samples from the subtidal zone and tidal flat, with an elevation range from -119.2 to 137.4 SWLI (-2.8 to 0.5 m above MTL). There are no consistent lateral elemental trends at NIA1, which is the only transect with samples from the subtidal zone. Station 3 in NIA1 has consistently lower elemental abundances than other stations along the transect, aside from Sr, for which Station 3 has an abnormally high abundance. NIA1 has very different elemental distributions than all other transects (Figure **3-11**A).

PAM cluster analysis identified three optimal clusters with an overall average silhouette width of 0.34 (Figure **3-11**BC). Cluster A includes two subtidal and three tidal flat stations (Stn01, Stn02, Stn06, Stn09, Stn10). The average silhouette width of Cluster

A is 0.40, representing an elevation range of -119.2–137.4 SWLI and a mean of 19.2 ± 129.1 SWLI. Cluster B contains one subtidal flat station (Stn03) and therefore has an average silhouette width of 0. Cluster C includes the remaining subtidal and three tidal flat stations (Stn04, Stn05, Stn07, Stn08). The average silhouette width of Cluster C is 0.34, representing an elevation range of -29.6–122.3 SWLI and a mean of 52.9 ± 72.9 SWLI.

PCA elemental variables for NIA1 are very different from those of all other transects. PC1 accounts for 62.9% of the total variance, which is the lowest percentage of all other transects. PC1 is driven by Sr in the negative direction and all other elemental variables in the positive direction. PC2 explains 23.6% of the remaining variance, with Si and K driving positive separation and Br and Fe influencing the negative PC2 direction (Figure **3-11**D).

Niawiakum River Transect 2 (NIA2)

Niawiakum River transect 2 (Figure **3-12**) is 87 m in length and consists of 20 surface sediment samples from the tidal flat, low marsh, and high marsh, spanning an elevation range of 38.2 to 239.0 SWLI (-0.80 to 1.8 m above MTL). Spatial elemental trends at NIA2 are consistent with most other transects, showing lithogenic (Si, K, Ti, Fe) and biogenic (Sr) elements as most abundant at low elevations and Br and ICR at high elevations (Figure **3-12**A).

PAM cluster analysis identifies three optimal clusters with an overall average silhouette width of 0.58 (Figure **3-12**BC). Cluster A includes all tidal flat, all low marsh, and the three lowest elevation, high marsh stations (Stn01–Stn10). The average silhouette of Cluster A is 0.65, with an elevation range of 38.2–226.4 SWLI and a mean of 156.9 ± 74.0 SWLI. Cluster B contains the remaining lower elevation, high marsh stations (Stn11 – Stn17). The average silhouette of Cluster B is 0.60, with an elevation range of 227.6–229.8 SWLI and a mean of 230.5 ± 2.1 SWLI. Cluster C contains the three highest elevation stations in the high marsh (Stn18 – Stn20). The average silhouette width of Cluster C is 0.30, representing an elevation range of 231.5–239.1 SWLI and a mean of 235.6 ± 3.8 SWLI.

PC1 explains 89.5% of the total variance, with ICR and Br driving separation in the positive direction and Si, K, Ti, Fe, and Sr in negative PC1 direction. The elements in

the negative PC1 direction also appear closely related, as their vectors are all nearly parallel to each other. PC2 accounts for 6.6% of the remaining elemental variance and is most influenced by Br (Figure **3-12**D).

Naselle River Transect 1 (NAS1)

Naselle River transect 1 (Figure **3-13**) is 407 m long and contains seven surface sediment samples from the low marsh and high marsh with an elevation range of 209.1 to 273.2 SWLI (1.7 to 2.6 m above MTL). NAS1 also shows elemental trends consistent with other transects, with lithogenic and biogenic elements most abundant at low elevations and Br and ICR values largest at high elevations (Figure **3-13**A).

PAM cluster analysis identified two optimal clusters with an overall average silhouette width of 0.68 (Figure **3-13**BC). Cluster A contains the three low marsh stations and the two most seaward high marsh stations (Stn01–Stn05). The average silhouette of Cluster A is 0.70, representing an elevation range of 209.1–269.7 SWLI and a mean of 237.0 ± 30.3 SWLI. Cluster B contains the two most landward high marsh stations (Stn06 – Stn07). The average silhouette width of Cluster B is 0.64, with an elevation range of 268.7 – 273.2 SWLI and a mean of 270.9 ± 3.2 SWLI.

PC1 explains 91.1% of the total variance, with Br and ICR driving separation in the positive direction and Si, Ti, K, Fe, Sr driving it in the negative direction. PC2 accounts for 7% of the remaining elemental variance (Figure **3-13**D).

Naselle River Transect 2 (NAS2)

Naselle River transect 2 (Figure **3-14**) is the longest transect, extending 1057 m and including 28 surface sediment samples from the tidal flat, low marsh, high marsh, and upland, with an elevation range of 39.4 to 269.3 SWLI (-0.93 to 2.57 m above MTL). Like other transects, NAS2 shows lithogenic and biogenic elements abundant at low elevations and Br and ICR more common at high elevations (Figure **3-14**A).

PAM cluster analysis identified four optimal clusters with an overall average silhouette width of 0.58 (Figure **3-14**B). Cluster A includes the ten most seaward tidal flat stations (Stn01–Stn10). The average silhouette width of Cluster A is 0.49 has an elevation range of 39.5–165.2 SWLI and a mean of 117.4 ± 42.9 SWLI. Cluster B contains the remaining tidal flat stations, all low marsh stations, and the lowest elevation

high marsh station (Stn11–Stn20). The average silhouette width of Cluster B 0.70 has an elevation range of 178.9–250.8 SWLI and a mean of 207.4 ± 26.4 SWLI. Cluster C contains six high marsh stations (Stn21–Stn25, Stn27), while Cluster D contains the remaining high marsh station (Stn25) and the sole upland station (Stn28). The average silhouette width of Cluster C is 0.25, with an elevation range of 257.8–265.6 SWLI and a mean of 259.7 ± 3.9 SWLI. The average silhouette width of Cluster D is 0.83, representing an elevation range of 267.3–269.3 SWLI and a mean of 268.3 ± 1.4 SWLI.

PC1 accounts for 70.6% of the total variance, with ICR and Br oriented in the positive direction and Si, K, Ti, Sr, and Fe in the negative direction. PC2 appears to be most influenced by Fe and Sr and accounts for 22.3% of the remaining variance (Figure **3-14**D).

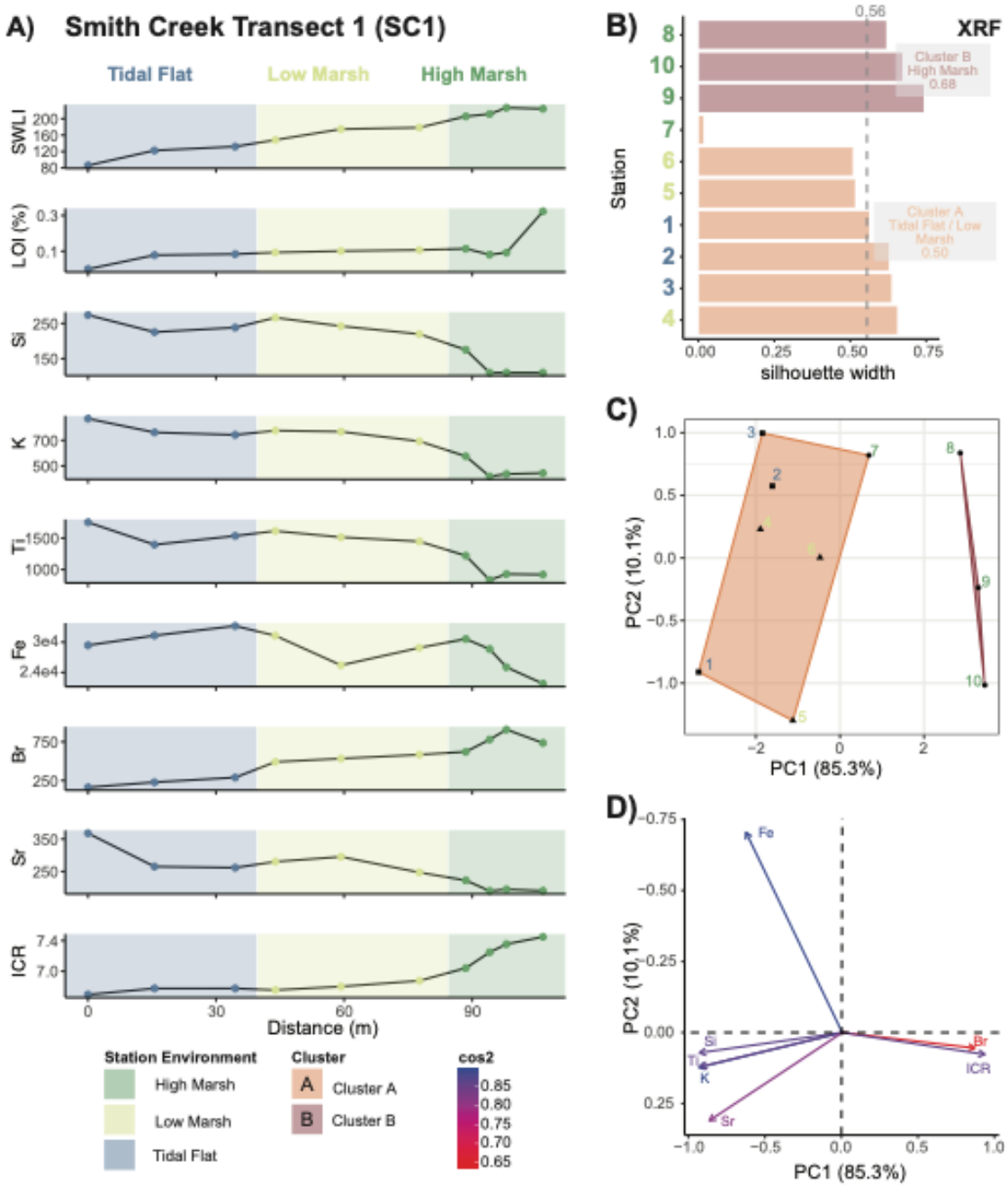

Figure 3-8 Elemental geochemical data for Smith Creek transect 1 (SC1). **(A)** Elemental abundances (normalized to ICR) along the transect. **(B)** PAM cluster silhouette widths for elemental composition. **(C)** PAM cluster plotted in the dimensions of principal component 1 and principal component 2. **(D)** PCA loading vectors (elemental variables) along principal component 1 and principal component 2

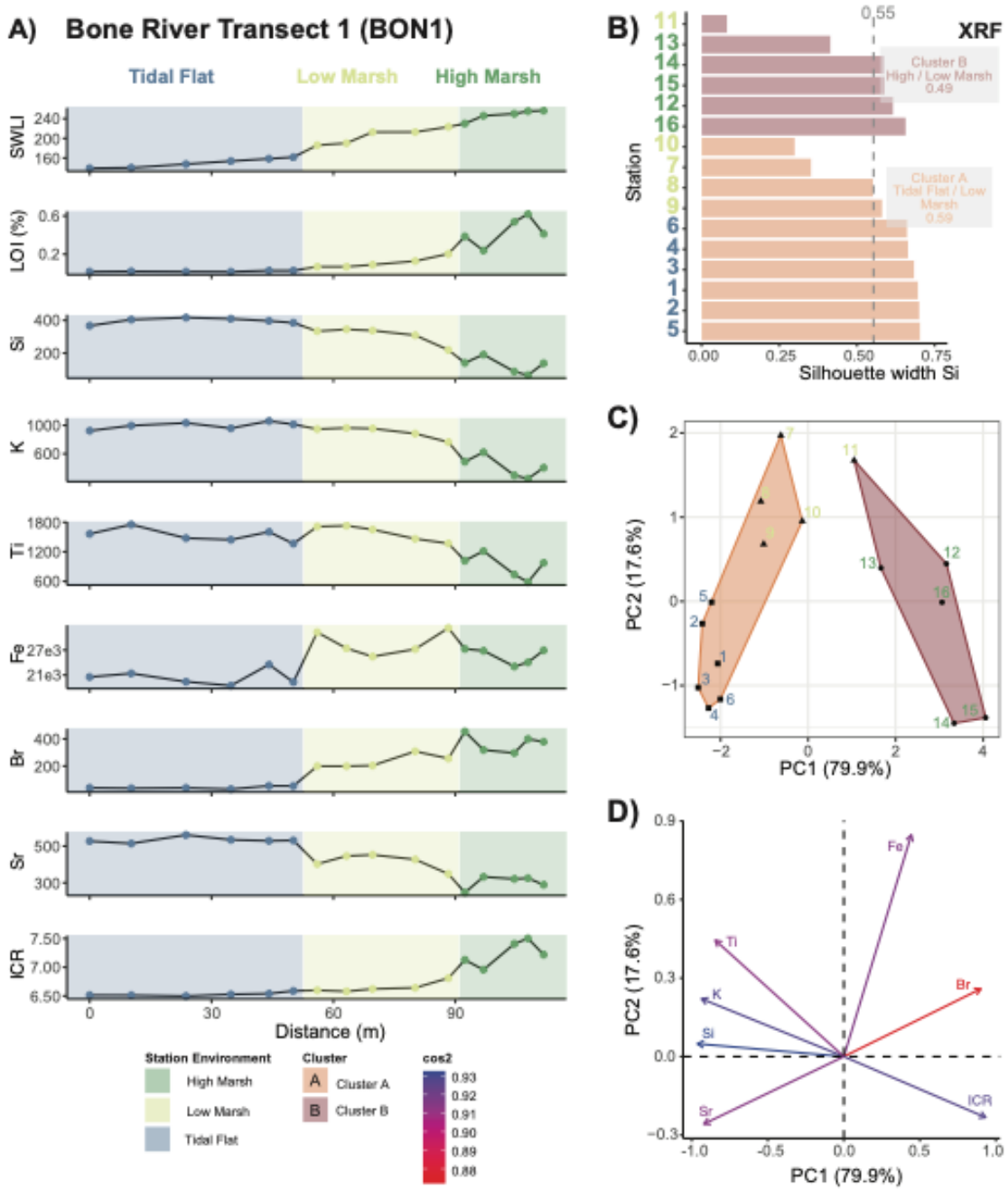

Figure 3-9 Elemental geochemical data for Bone River transect 1 (BON1). **(A)** Elemental abundances (normalized to ICR) along the transect. **(B)** PAM cluster silhouette widths for elemental composition. **(C)** PAM cluster plotted in the dimensions of principal component 1 and principal component 2. **(D)** PCA loading vectors (elemental variables) along principal component 1 and principal component 2

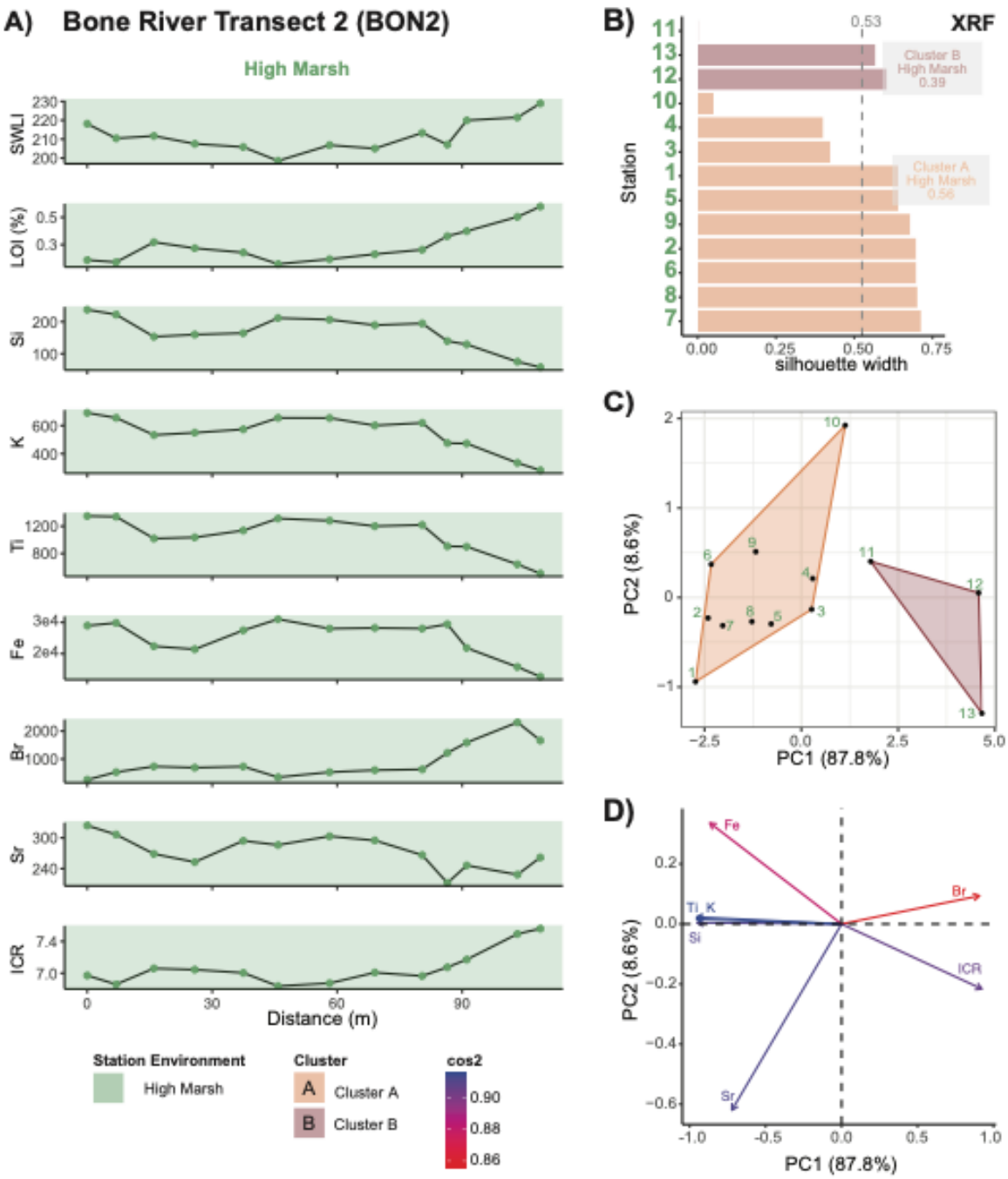

Figure 3-10 Elemental geochemical data for Bone River transect 2 (BON2). **(A)** Elemental abundances (normalized to ICR) along the transect. **(B)** PAM cluster silhouette widths for elemental composition. **(C)** PAM cluster plotted in the dimensions of principal component 1 and principal component 2. **(D)** PCA loading vectors (elemental variables) along principal component 1 and principal component 2

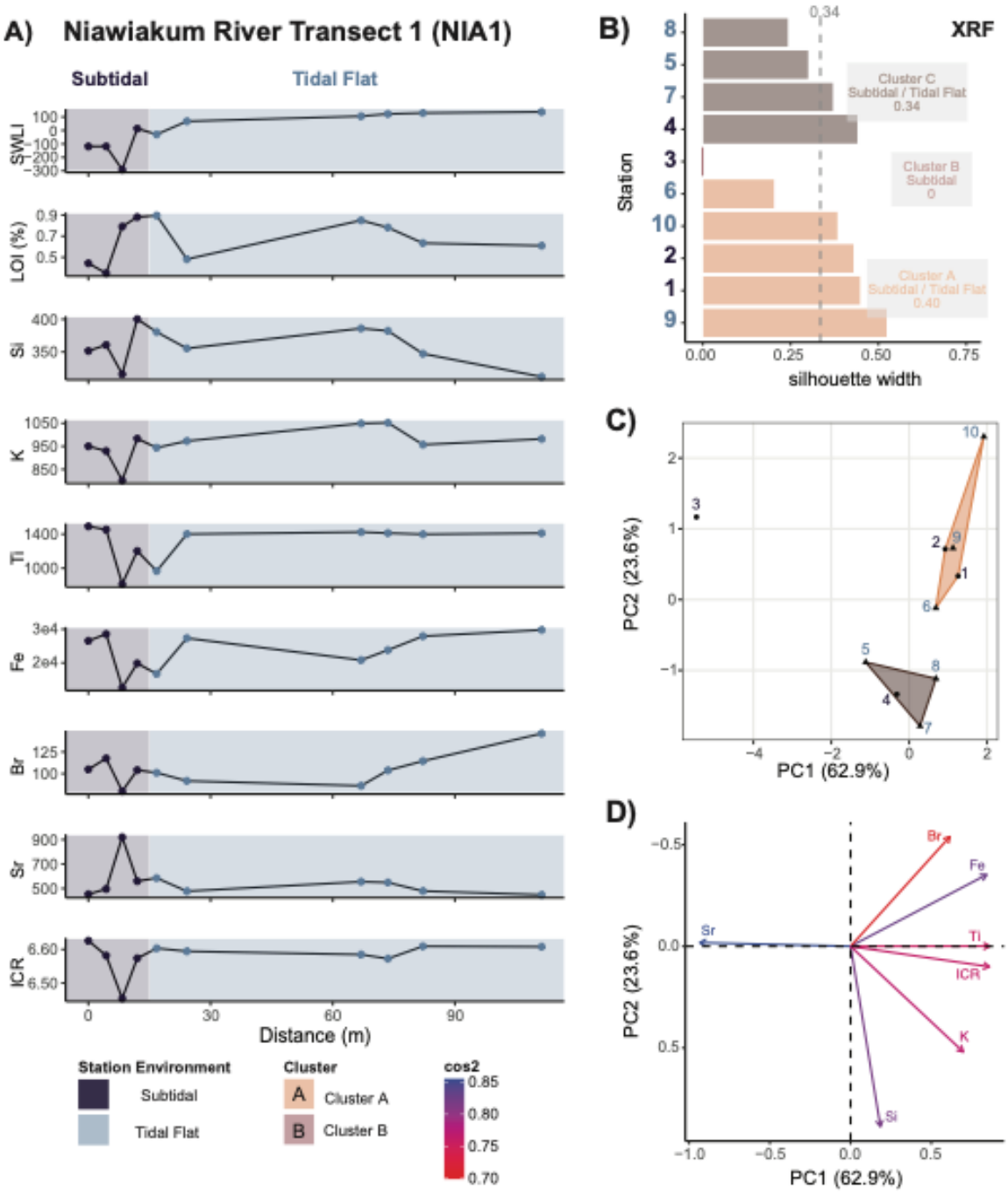

Figure 3-11 Elemental geochemical data for Niawiakum River transect 1 (NIA1). **(A)** Elemental abundances (normalized to ICR) along the transect. **(B)** PAM cluster silhouette widths for elemental composition. **(C)** PAM cluster plotted in the dimensions of principal component 1 and principal component 2. **(D)** PCA loading vectors (elemental variables) along principal component 1 and principal component 2.

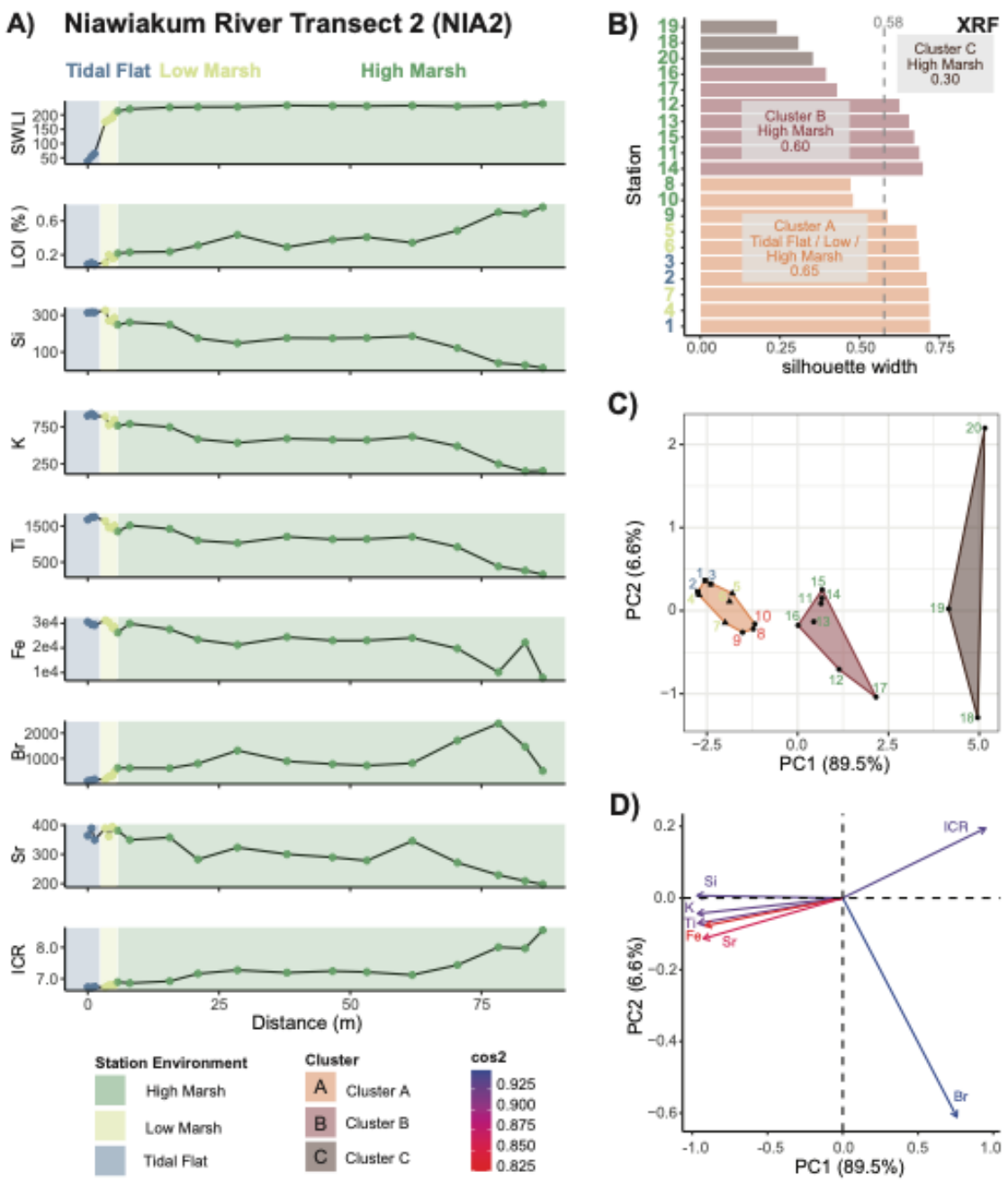

Figure 3-12 Elemental geochemical data for Niawiakum River transect 2 (NIA2). **(A)** Elemental abundances (normalized to ICR) along the transect. **(B)** PAM cluster silhouette widths for elemental composition. **(C)** PAM cluster plotted in the dimensions of principal component 1 and principal component 2. **(D)** PCA loading vectors (elemental variables) along principal component 1 and principal component 2

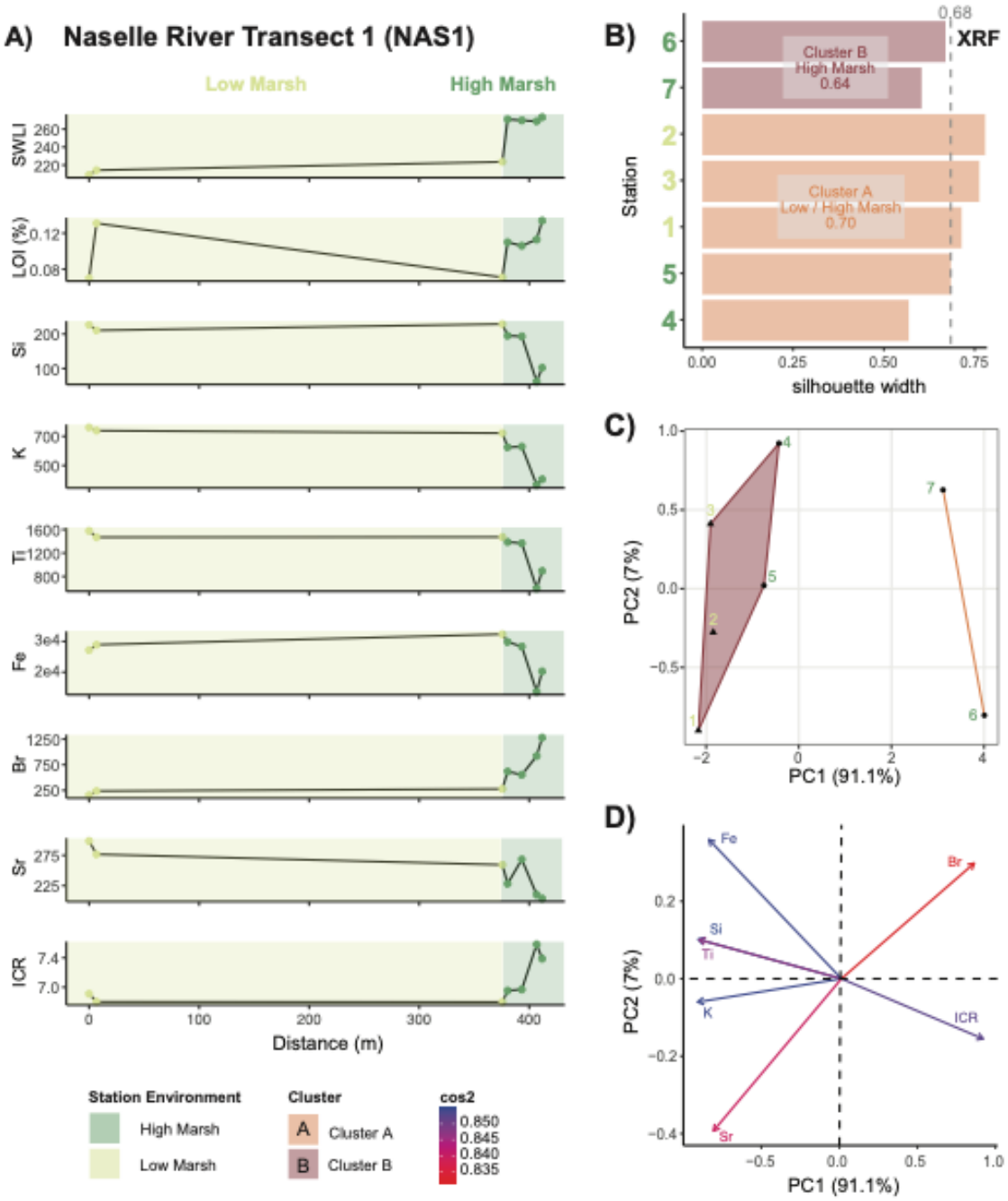

Figure 3-13 Elemental geochemical data for Naselle River transect 1 (NAS1). **(A)** Elemental abundances (normalized to ICR) along the transect. **(B)** PAM cluster silhouette widths for elemental composition. **(C)** PAM cluster plotted in the dimensions of principal component 1 and principal component 2. **(D)** PCA loading vectors (elemental variables) along principal component 1 and principal component 2

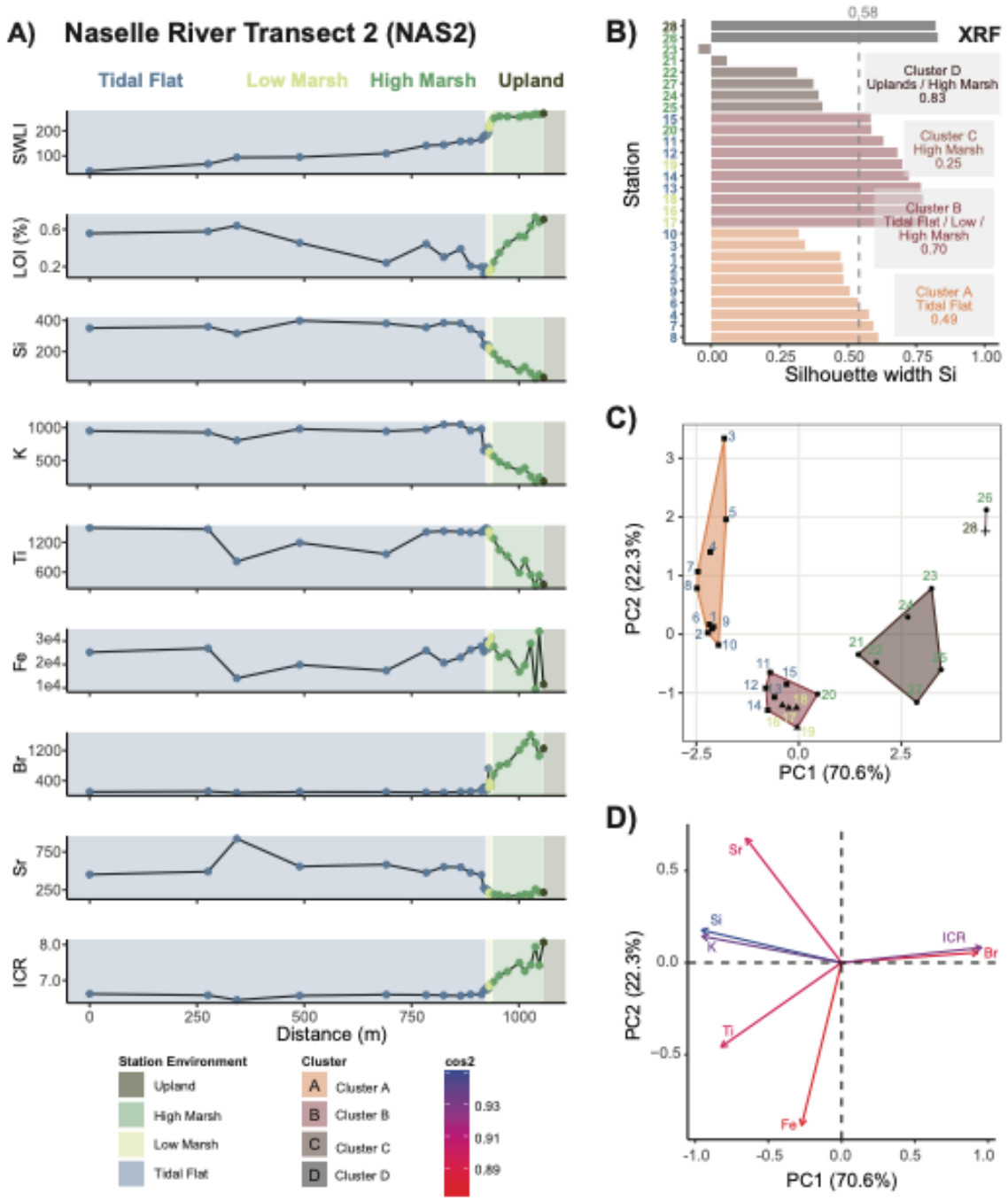

Figure 3-14 Elemental geochemical data for Naselle River transect 2 (NAS2). **(A)** Elemental abundances (normalized to ICR) along the transect. **(B)** PAM cluster silhouette widths for elemental composition. **(C)** PAM cluster plotted in the dimensions of principal component 1 and principal component 2. **(D)** PCA loading vectors (elemental variables) along principal component 1 and principal component 2.

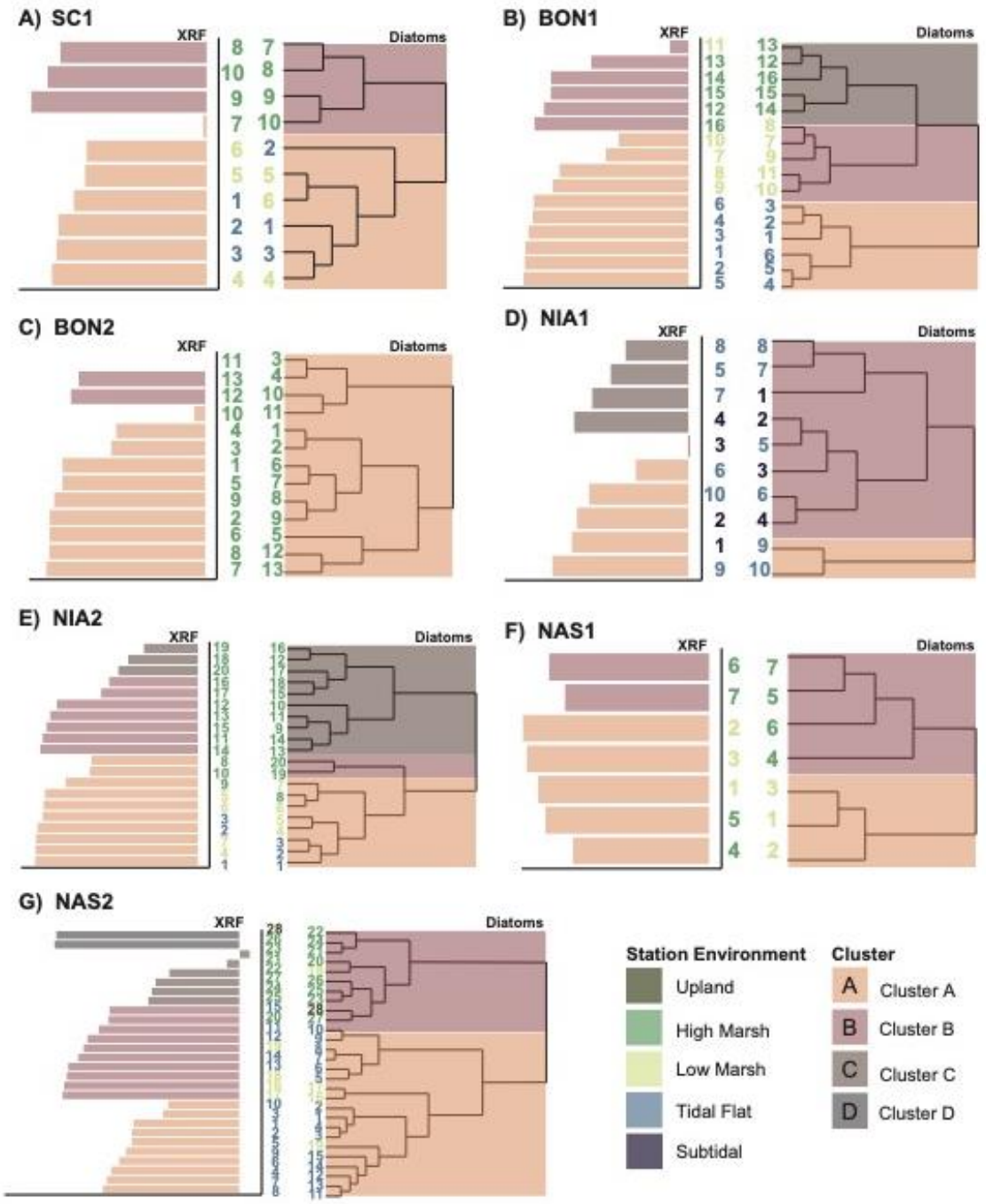

Figure 3-15 Comparison between elemental geochemistry PAM clusters and diatom hierarchical clustering at Willapa Bay. Clustered diatom data obtained from Hong et al. (2019). **(A)** Smith Creek transect 1. **(B)** Bone River transect 1. **(C)** Bone River transect 2. **(D)** Niawiakum River transect 1. **(E)** Niawiakum River transect 2. **(F)** Naselle River transect 1. **(G)** Naselle River transect 2.

3.5.4. Comparison between Elemental and Microfossil Clusters

PAM analysis of the elemental data consistently reveals lower and higher elevation clusters within transects that span the full marsh gradient. Although the geochemical clusters do not exactly reflect environmental delineation indicated by salt marsh vegetation, stations are often grouped in station sequence, which suggests a relationship to tidal elevation. At Port Alberni, foraminifera were clustered using PAM analysis, while at Willapa Bay, diatoms were clustered using a hierarchical approach (Riou, 2023; Hong et al., 2021). The ARI is used to compare how well the geochemical or microfossil clusters match up with environmental zones described by salt marsh vegetation for an individual transect. ARI elemental geochemistry values for all transects show positive values, which suggests agreement between geochemical clusters and environments described by salt marsh vegetation (Table **3-3**). Microfossil ARI values are generally larger than elemental ARI values, except for two transects (PA2, NIA1; Table 3-3). The ARI values demonstrate that elemental composition has comparable vertical zonation patterns to well-established microfossil assemblages when compared with salt marsh vegetation, but microfossils generally outperform elemental composition in recreating environmental zones.

3.5.5. Regional – Port Alberni and Willapa Bay

We assessed both the local (PA and Willapa individually) and regional (PA and Willapa combined) XRF datasets to determine their similarities and differences, given that Port Alberni and Willapa Bay are separated by a distance of ~290 km.

When all three Port Alberni transects (37 stations) were combined (Figure **3-16**AB), PAM analysis revealed three distinct geochemical clusters. Cluster A (19 stations) includes tidal flat stations and low marsh stations, representing an elevation range of 48.7–163.7 SWLI (0.95 – 1.57 m above MTL) with a mean of 98.0 ± 30.9 SWLI. Cluster B (15 stations) includes low marsh and high marsh stations, with an elevation range of 143.4–283.6 SWLI (1.32 – 2.24 m above MTL) and a mean of 204.8 ± 32.6 SWLI. Cluster C (3 stations) comprises high marsh stations, with an elevation range of 223–261.4 SWLI (2.68 – 3.26 m above MTL) with a mean of 240.3 ± 19.3 SWLI. The regional elemental clustering at Port Alberni shows comparable results to the clusters of individual transects. Individual transects at Port Alberni have two or three elemental

clusters that consistently discriminate low elevation tidal flat samples from higher elevation samples of the high marsh environment. The agreement between elemental clusters of individual and regional Port Alberni transects demonstrates the consistency of elemental distributions and abundances with respect to tidal elevation at a larger scale.

Clustering of all Willapa Bay transects (104 stations) also reveals three distinct clusters (Figure **3-16**CD). Cluster A (35 stations) includes lower elevation subtidal, tidal flat, and low marsh stations, with an elevation range of -291.2–212.9 SWLI (-5.03 – 1.43 m above MTL) and a mean of 94.7 ± 103.7 SWLI. Cluster B (45 stations) includes intermediate elevation stations from the tidal flat, low marsh, and high marsh. Cluster B has an elevation range of 122.5–270.8 SWLI (0.29 – 2.61 m above MTL), with a mean of 209.9 ± 30.7 SWLI. Cluster C (24 stations) contains only high marsh and upland stations, with an elevation range of 207.1–273.2 SWLI (1.36 – 2.65 m above MTL) and a mean of 243.6 ± 20.3 SWLI. The Willapa Bay regional data have a similar clustering pattern to individual transects that capture the full elevation gradient of the salt marsh (e.g., NIA2, NAS2). The regional clusters represent three distinct elemental compositions with a relationship to tidal elevation: low, intermediate, and high elevation environments. While BON2 and NIA1 transects did not reveal clear elemental trends, as they did not capture the full elevation gradient, the elemental abundances are still compatible with the regional dataset, and the general trends are maintained. Like at Port Alberni, the regional dataset of Willapa Bay shows that the elemental data of individual transects are compatible at a larger scale, demonstrating consistent elemental distributions and abundances.

Combining all 10 transects from both Port Alberni and Willapa Bay, the clustering of elemental data reveals only two distinct groups (Figure **3-16**EF). Despite the lower number of clusters compared to the Port Alberni and Willapa Bay regional datasets, they still represent a lower and higher elevation cluster. This suggests that combining regional elemental datasets lowers “clustering resolution”. While elemental trends are consistent between Port Alberni and Willapa Bay, the elemental abundances apparently differ enough that combining multiple regional datasets can blur the relationship established between the elemental composition of an individual region with tidal elevation.

The elemental variables plotted in PC-space for the Port Alberni (Figure **3-16**B), Willapa Bay (Figure **3-16**D), and combined regional (Figure **3-16**F) datasets reveal consistent elemental drivers. PC1 accounts for a large percentage (> 70%) of the total elemental variance in the combined dataset. In PC1, lithogenic (Si, K, Ti, Fe) and biogenic (Sr) elements are oriented in the negative direction, while ICR and Br are oriented in the positive direction. Despite the regional consideration of the elemental dataset, PC1 is consistently controlled by the same elements, oriented in the same direction. This suggests that PC1 is capturing the same environmental processes at both Port Alberni and Willapa Bay that are controlling elemental distribution along the tidal gradient.

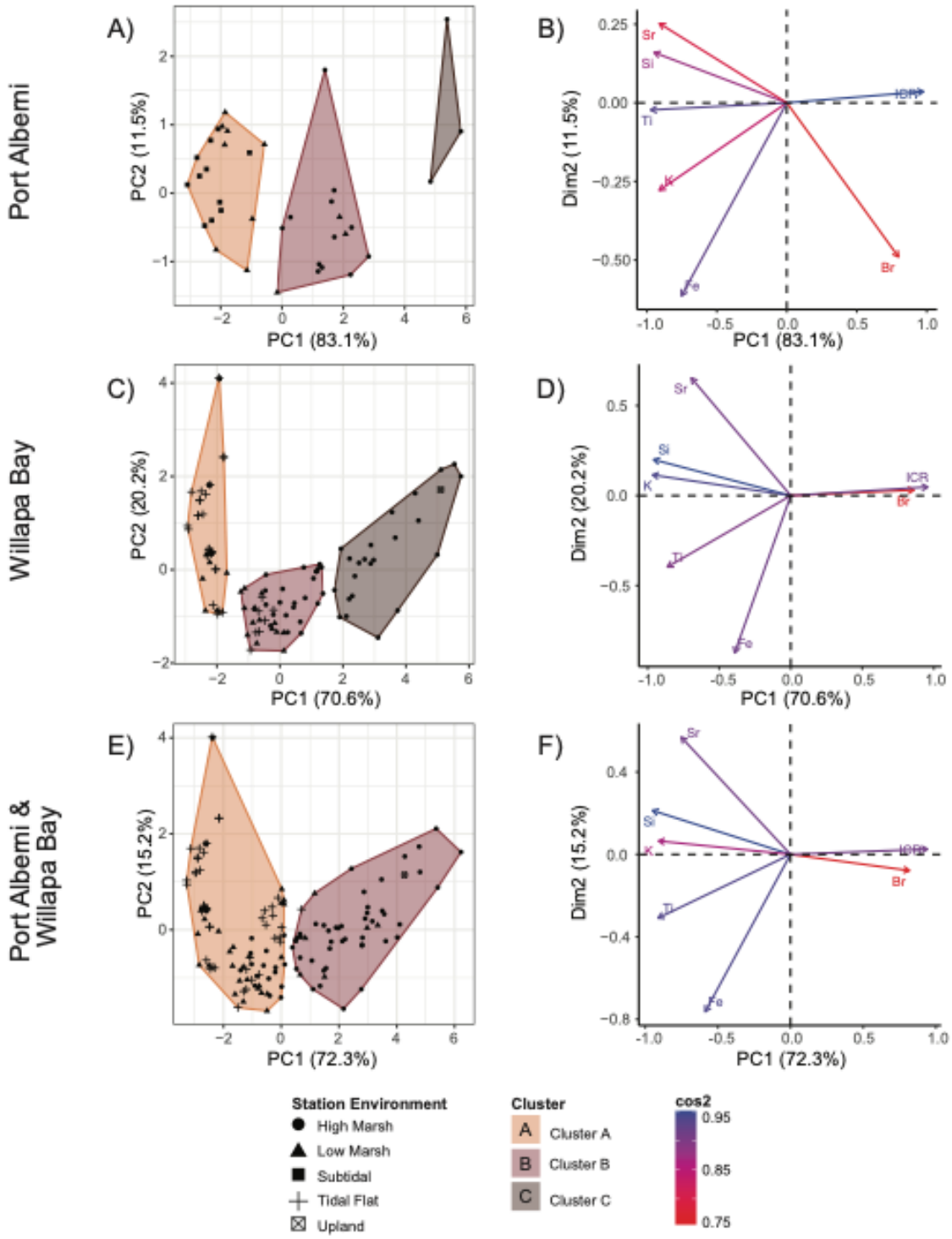

Figure 3-16 Local and Regional comparison of elemental geochemistry. **(A)** Local Port Alberni PAM clusters. **(B)** Local Port Alberni PCA loading vectors along principal component 1 and principal component 2. **(C)** Local Willapa Bay PAM clusters. **(D)** Local Willapa Bay PCA loading vectors along principal component 1 and principal component 2. **(E)** Regional Port Alberni and Willapa Bay PAM cluster. **(F)** Regional Port Alberni and Willapa Bay PCA loading vectors.

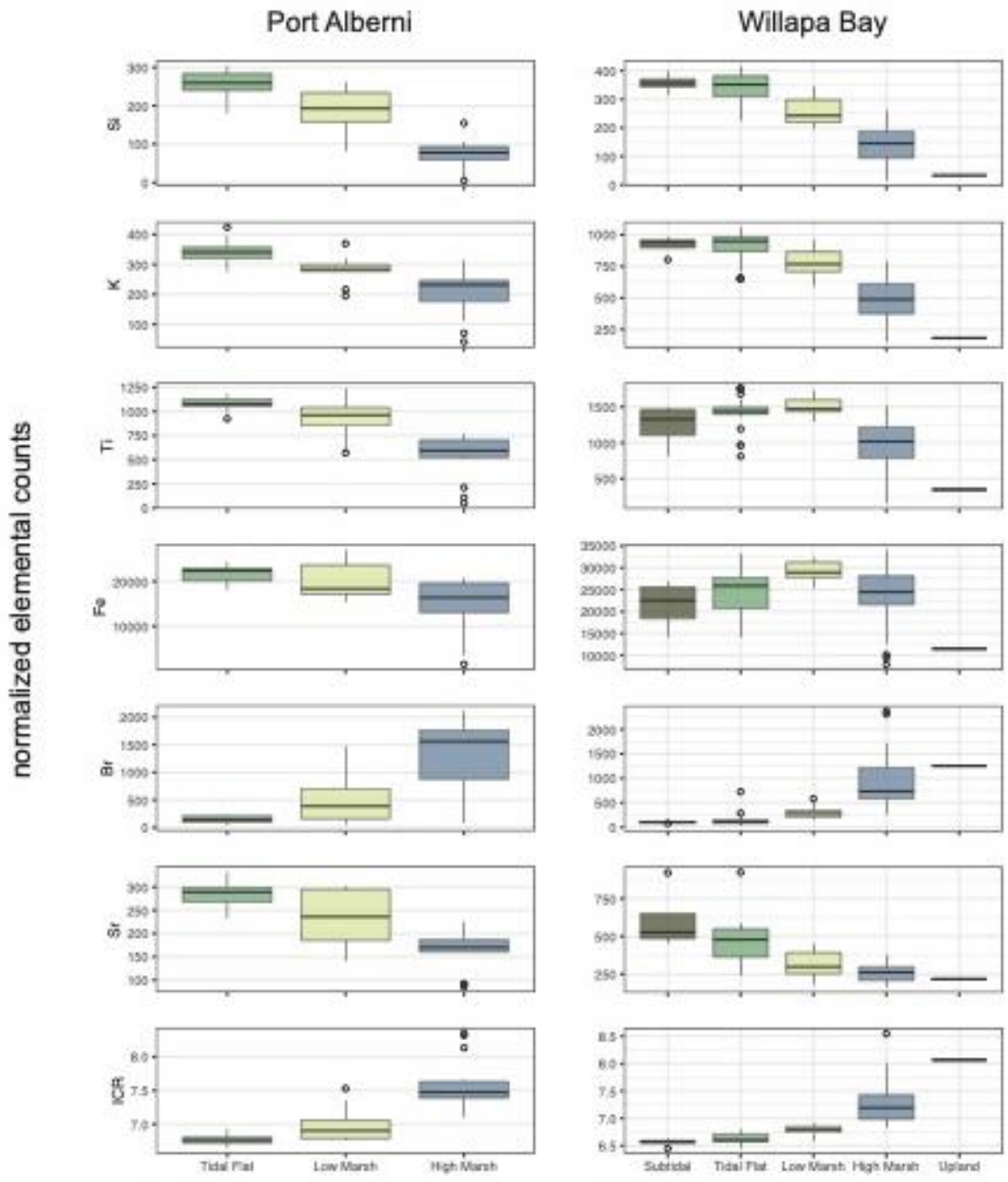

Figure 3-17 Boxplots of normalized elemental counts against observed environmental zones as described by salt marsh vegetation for Port Alberni and Willapa Bay. For each boxplot, the dark horizon bar represents the medium, the solid box represents the interquartile range, the vertical lines represent the minimum and maximum values, and the dots beyond the whiskers represent outliers.

3.6. Discussion

3.6.1. Vertical Zonation of Elements within Cascadia Salt Marshes

Sea-level indicators such as vegetation and microfossils (e.g., foraminifera, diatoms) along the world's coastlines display vertical zonation patterns, with distributions and abundances within the tidal frame related to tidal elevation (e.g., Hong et al., 2021; Rush et al., 2021; S. Williams et al., 2021). Elemental geochemistry of salt marshes from Port Alberni and Willapa Bays share this same relationship.

Within the subtidal and tidal flat zones, vascular plant vegetation is either absent or extremely sparse because its distribution is controlled by salinity tolerances and the frequency and duration of tidal inundation (e.g., Behre, 1986; Macdonald & Barbour, 1977). At these low elevations, microfossil assemblages are dominated by marine species such as calcareous marine foraminifera (e.g., *Ammonia* spp.*)* at Port Alberni and marine diatoms at Willapa Bay (e.g., *Grammatophora Oceanica*) (Hong et al. 2021; Riou, 2023). The elemental geochemistry in the subtidal and tidal flat environments is dominated by lithogenic (Si, Ti, Fe, Ti) and biogenic (Sr) elements that reflect clastic mud deposited in tidal waters.

The highest elevations along the salt marsh gradient are characterized by salt-tolerate plants because less frequent tidal inundation at higher elevations allows for the establishment of dense marsh vegetation. Microfossils at higher elevations include species that are less tolerant of salt water, including *Balticammina psuedomacresens* and *Haplophragmoides* spp. foraminifera at Port Alberni and *Cosmioneis pusilla* and *Luticola mutica* diatoms at Willapa Bay (Hong et al. 2021; Riou, 2023). The elemental composition in the high marsh shows high values of Br and ICR, which reflects the amount of organics derived from salt marsh vegetation.

Similar to other well-established sea-level indicators, elemental geochemistry shows vertical zonation patterns along marsh transects that can be used to distinguish sub-environments. Sub-environments recognized through elemental geochemistry at Port Alberni and Willapa Bay are in agreement with vegetation and microfossil sea-level proxies investigated at these two sites.

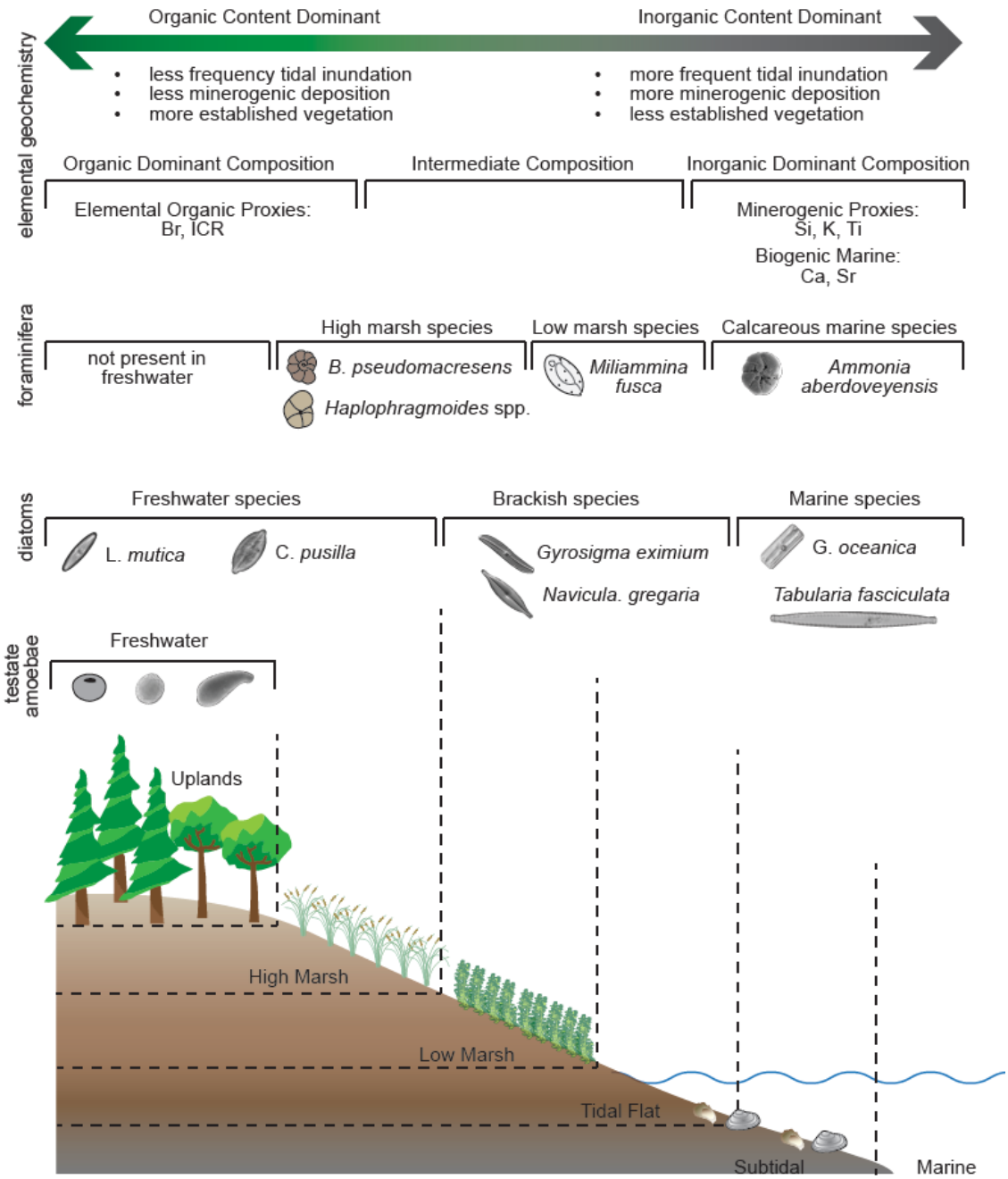

Figure 3-18 Conceptual model and summary of idealized vertical zonation patterns of foraminifera, testate amoebae, diatoms, and elemental geochemistry at Port Alberni and Willapa Bay.

3.6.2. Drivers of Elemental Variability

The separation of stations along PC1 is related to tidal elevation. The elemental variables within PC-space driving this separation reflect the inorganic verses organic content of the bulk sediment. At low tidal elevations, more frequent inundation results in

the deposition of fine-grained inorganic sediment, while at high elevations, less frequent inundation allows for the establishment of vascular vegetation. PC1 also shows potential for distinguishing intermediate compositions between inorganic-dominated lower elevations and organic-dominated higher elevations (e.g., PA1, NIA2, NAS2). This suggest that elemental distribution at both Port Alberni and Willapa Bay reflects these sedimentological characteristics and therefore is controlled by tidal inundation.

Inorganics

Tidal flat stations consistently cluster towards negative PC1, which is consistently driven by lithogenic elements (Si, K, and Ti), suggesting their distributions are controlled by similar sources and processes. These lithogenic elements show similar trends at both Port Alberni and Willapa Bay, where they are most abundant at low elevations (i.e., tidal flat) and least abundant at high elevations (i.e., high marsh). In the intertidal environment, deposition of lithogenic elements is dominated by tidal inundation, and the highest abundances of Si, K, and Ti coincide with low elevations where tidal inundation is most frequent. This is consistent with the local geology of both regions, which comprises basalts, clastic sedimentary rocks, and Quaternary sediments derived from bedrock lithologies. The lithogenic elements are interpreted as detrital or terrigenous sedimentary input related to weathering and erosion (e.g., Longman et al., 2017; Turner et al., 2015; Unkel et al., 2008, 2010). Frequent tidal inundation remobilizes fine-grained detrital sediment from the subtidal basin and carries it into the intertidal environment of the salt marsh. Therefore, high abundance of lithogenic elements at low tidal elevations reflects frequent tidal inundation, remobilization, and deposition of clastic sediment. This is consistent with the lithostratigraphy of salt marshes, where inorganic fine-grained sediment is associated with low tidal elevations (e.g., Atwater, 1987; Shennan, 1986; Shennan et al., 1996).

Organics

High marsh stations consistently cluster towards the positive PC1 axis, which is driven by Br and ICR. Br and ICR have lower values at low elevations (i.e., tidal flat) and higher values at high elevations (i.e., high marsh). The presence of high Br values and ICR at higher elevations suggests their distributions reflect the organic content of the bulk sediment.

Br interpretations in paleoenvironmental studies are challenging in coastal settings. Br^- ions are present at high concentrations within seawater, but do not appear to be abundant at low elevations, where tidal inundation is most frequent, but rather at high elevations where inundation is less frequent. This discrepancy may be the result of Br being created by biogeochemical processes in organic-rich sediment to form organohalogens with peat and other organic soils, transforming soluble and mobile Br^- ions into immobile species (Biester et al., 2005; Keppler et al., 2000). As a result, Br abundance along the Port Alberni and Willapa Bay transects is controlled by the presence of organic matter, which is most common in the high marsh. The source, however, is seawater via tidal inundation and sea-spray. Here, Br is interpreted to reflect organic matter (e.g., Hahn et al., 2014; Olsen et al., 2010; Ziegler et al., 2008), but it has also been interpreted as being associated with coastal storminess and marine incursions (e.g, Chagué-Goff et al., 2016; Oliva et al., 2018).

Incoherent (Compton) and coherent (Rayleigh) scattering ratio (ICR) trends are consistent at Port Alberni and Willapa Bay, with low values at low elevations and high values at high elevations. This reflects the establishment and distribution of organics within the salt marshes, with vegetation gradually increasing landward into the high marsh and uplands. ICR is commonly applied as a “pseudo-proxy” for organic content because, while X-ray scattering is related to low atomic mass elements (e.g., C, H, O) that are dominant in organic sediments, there are other factors such as water content, sediment surface roughness, and sediment density that will influence ICR (e.g., Chagué-Goff et al., 2016; Chawchai et al., 2016; Guyard et al., 2007; Woodward & Gadd, 2019).

3.6.3. Elemental Geochemistry as a Sea-Level Indicator

Elemental geochemistry of bulk sediment is a promising new sea-level indicator, with the potential to be used in tandem with other well-established methods. Transfer functions are empirically derived equations used to estimate paleoenvironmental conditions (e.g., paleo-marsh elevation) based on modern training sets of microfossil data (Sachs et al., 1977). The Bayesian Transfer Function (BTF) offers bespoke sea-level reconstructions by supplementing microfossil data with additional sea-level indicator proxies, known as priors (e.g., Cahill et al., 2016; Kemp et al., 2018; Riou, 2023).

Elemental geochemistry can potentially be applied as a prior in BTFs to supplement and constrain microfossil-based sea-level reconstructions (e.g., Cahill et al., 2016; Kemp et al., 2013; Walker et al., 2023). While elemental composition can distinguish between lower and higher elevation groups within the intertidal range, it is unclear whether the elemental composition can identify between subtidal, intertidal, and supratidal environments. Only one transect (NIA1) contained stations from the subtidal environment, and it only spanned the subtidal to tidal flat zones. Elemental composition was unable to differentiate the boundary between the subtidal and intertidal range. There is only one upland station (supratidal) within the NIA2 transect, and based on elemental composition, it was not separated from adjacent high marsh stations. This suggests that, while elemental composition can consistently differentiate between lower and higher elevations within the intertidal range, it may be less suitable for distinguishing the intertidal ranges of subtidal and supratidal environments. To further constrain and confirm the indicative range of elemental geochemistry in these cases, additional transects that are more representative of, and better capture, the subtidal and upland environments are required.

Elemental geochemistry may face similar shortcomings to stable carbon isotopes, LOI, and Rock-Eval pyrolysis (RE), in which the indicative tidal range is less constrained than it is for microfossil proxies (cannot distinguish between subtidal, intertidal, and supratidal environments). Elemental geochemistry may also face challenges of poor preservation and post-depositional changes in sediments due to biogeochemical processes that can remobilize elements.

Comparison with other Geochemical Indicators

Other geochemical techniques have previously been examined for their potential as sea-level indicators. For example, stable carbon isotopes ($\delta^{13}C$, C/N) have been shown to differentiate between C_3 verses C_4 vegetation (different photosynthetic pathways) and fresh verses marine organic matter (e.g., Kemp et al., 2010; Khan et al., 2019; Lamb et al., 2006; Wilson et al., 2005). Along the Atlantic coast of North America $\delta^{13}C$ and C/N are powerful proxies that can distinguish between intertidal vegetation (consists exclusively of C_4 plants e.g., *Spartina spp*. and *Distichlis spicata)* and supratidal vegetation (exclusively C_3 plants) (e.g., Kemp et al., 2013). This vertical zonation pattern is reliant on the presence and distribution of plant species that can span

a wide elevation range in tidal marshes. $\delta^{13}C$ and C/N are less effective geochemical proxies along the Pacific coast of North America where C_3 plants dominate both intertidal and supratidal environments. Post-depositional organic decomposition is also known to alter $\delta^{13}C$ and C/N values, which can make paleoenvironmental interpretations challenging in the absence of other proxy indicators.

Loss-on-ignition (LOI) and Rock-Eval (RE) pyrolysis are two other well-established methods for estimating the organic content of bulk salt marsh sediment. LOI is an efficient method for estimating organic content; it is calculated as the percent weight different between sediment that has been dried (at 105°C) and sediment that has been ignited (at 475°C – 550°C), and indicates the mass of organics lost through pyrolysis. LOI has become a well-established and widely adopted method in paleoenvironmental reconstructions and sea-level research due to its simplicity in estimating organic and inorganic content in marsh sediments (e.g., Barlow et al., 2014; Barnett et al., 2017; Shennan, 1986; Shennan et al., 1996; Stewart et al., 2017; Zong et al., 2003). RE pyrolysis was initially developed for petroleum exploration, but has increasingly being used in paleoenvironmental studies (e.g., Kemp et al., 2019; Lacey et al., 2015; Lafargue et al., 1998; Newell et al., 2016). In RE pyrolysis, sediment is progressively heated in the absence of oxygen and the concentrations of hydrocarbons and CO_2 are measured over specific temperature intervals, and then used as inputs to calculate and determine the origin of organics in sediments. Both LOI and RE have been applied as sea-level indicators, but have limited utility because estimates of organic content are incapable of distinguishing intertidal environments (mangroves and salt marshes) from supratidal freshwater environments (e.g., Kemp et al., 2017, 2019).

Elemental composition offers an additional geochemical proxy for sea-level research. This project demonstrates consistent local and regional relationships between elemental abundances and tidal elevations at two Cascadia salt marshes separated by ~290 km. The vertical zonation patterns of elemental geochemistry revealed through cluster analysis are consistent and at times superior to well-established microfossil proxies. Compared to stable carbon isotopes, elemental geochemistry may be more consistent and applicable to various coastlines because elemental distributions are a function of bulk sediment composition rather than the presence of C_3 or C_4 salt marsh vegetation. Therefore, elemental geochemistry is less limited by climatic or ecological considerations. The large elemental data output of the XRF-CS also can be used with

rigorous multivariate statistical approaches for investigating relationships with environmental variables that are not possible for other geochemical proxies that do not generate large multivariate datasets(e.g., Kaboth-Bahr et al., 2019; Peti et al., 2019). This leads to greater potential for teasing out minor differences along the elevation gradient that may not be captured by only a few geochemical variables.

3.6.4. The Future of Elemental Geochemistry as a Sea-level Indicator

In this exploratory study, elemental geochemistry has been shown to have potential as a sea-level indicator, as it can create clustering patterns that match well-established microfossil proxies. While the relationship between elemental composition and tidal elevation is consistent at Port Alberni and Willapa Bay, investigating additional marshes along the CSZ is required to refine and strengthen elemental geochemistry as a sea-level indicator. Exploring the utility of elemental geochemistry outside the Cascadia region at other coastlines around the world is also crucial for assessing elemental distributions in different climatic, geomorphologic, and geologic environments. This will further define the applicability of elemental geochemistry as a sea-level indicator around the world. XRF-CS analyzes a much wider suite of elements than those used in this study, each with potential for supplementing the elemental database. Exploring additional elements detectable by XRF-CS (e.g., trace elements: Pb, Rb, Ni) could offer additional proxies to bolster paleo-environmental interpretations, further highlighting the potential of elemental geochemistry in Holocene sea-level research (e.g., Croudace et al., 2019; Hahn et al., 2014; Hennekam et al., 2019). Applying the elemental modern training set to BTFs to reconstruct past sea-level change from the sediment record depends on how well elements are retained in the geologic record. Studying the preservation potential and mobility of elements in the sediment record will be a crucial step in developing elemental geochemistry as a prior to constrain microfossil-based reconstructions or as a stand-alone proxy for reconstructing sea-level change (e.g., Cahill et al., 2016; Kemp et al., 2018).

3.7. Conclusion

In this study, we have explored the utility of XRF-CS and elemental geochemistry as a rapid, high-resolution, and non-destructive method for sea- and land-level

reconstructions. PAM clustering of elemental data consistently reveals low-elevation and high-elevation clusters, suggesting that elemental geochemistry has potential for quantifying tidal elevations. Elemental clusters are also in agreement with foraminifera clusters in Port Alberni and diatom clusters in Willapa Bay, suggesting that elemental geochemistry yields results consistent with their microfossil counterparts and confirms a relationship to tidal elevation. XRF-CS and elemental geochemistry in high-resolution sea- and land-level reconstructions is in its infancy but offers many advantages and unexplored applications as a sea-level indicator.

Chapter 4. Conclusion

4.1. Summary

Seismic hazards associated with the CSZ are difficult to quantify because the recurrence interval of megathrust earthquakes span multi-decadal to centennial periods and there has not been a full margin rupture during historical times. Without modern analogues of CSZ earthquakes, we must rely on stratigraphic evidence preserved in the geologic record to provide insights into magnitudes, rupture patterns, and frequencies of past events as a way of informing our understanding of future earthquakes. Megathrust earthquakes are commonly preserved in the geologic record as episodes of coseismic subsidence that can be quantified by reconstructing RSL change across the coseismic subsidence contact. Common sea-level indicators used to reconstruct RSL change include foraminifera and diatoms that have well-established relationships with tidal elevation. Despite their widespread use, microfossil applications are limited where fossil preservation is poor or modern species are not representative of those found in the fossil record. Establishing additional sea-level indicators in the RSL reconstruction "toolbox" will increase applicability and flexibility of sea/land-level reconstructions along coastlines around the world.

This thesis explores the use of elemental geochemistry obtained through XRF-CS as a new sea-level indicator at salt marshes at Port Alberni, British Columbia and Willapa Bay, Washington. The elemental composition of surface sediments can distinguish between different amounts of inorganic and organic material controlled by the frequency of tidal inundation and tidal elevation. Inorganic content is strongly related to lithogenic (Si, K, Ti, Fe) and biogenic (Sr) elements. Clastic sediment dominates at lower elevations where tidal inundation is more frequent, resulting in more abundant inorganic proxy elements. Organic element proxies (Br, ICR) are most abundant at higher elevations where tidal inundation is less frequent and vegetation most common. PAM cluster analysis demonstrates that elemental geochemistry provides comparable and, in some cases, higher resolution vertical zonation than foraminifera at Port Alberni and diatoms at Willapa Bay. Consistent elemental trends at Port Alberni and Willapa Bay highlight the reproducibility and potential of the XRF-CS approach. They also show that elemental composition is capturing the same trends and processes at two locations

about 290 km apart in Cascadia. Elemental geochemistry also has the benefits and advantages offered by XRF-CS, including rapid and cost-effective analyses that generate large multivariate elemental datasets. Whether elemental geochemistry can be applied to tidal wetland paleo-records as a stand-alone proxy or a supplemental proxy to microfossils remains to be seen and will require further investigation.

4.2. Research Contributions

This thesis demonstrates that elemental geochemistry obtained through XRF analysis shows consistent relationships with tidal elevation, underscoring the value of elemental geochemistry as a sea-level indicator along Cascadia coastlines. I established preliminary methodologies for preparing discrete salt marsh samples for analysis on the ITRAX XRF-CS and developed the first elemental modern training describing the relationship between elemental composition and tidal elevation at Port Alberni, Canada and Willapa Bay, USA, two locations spaced ~290 km apart.

References

Alberni Valley Museum. (2011). *Hisheenqu'as, Living Together: Alberni and the Birth of the BC Forest Industry*.

Atwater, B. F. (1987a). Evidence for Great Holocene Earthquakes along the Outer Coast of Washington State. *Science*, *236*(4804).

Atwater, B. F. (1987b). Evidence for Great Holocene Earthquakes along the Outer Coast of Washington State. *Science*, *236*(4804), 942–944.

Atwater, B. F., & Hemphill-Haley, E. (1997). Recurrence intervals for great earthquakes of the past 3,500 years at northeastern Willapa Bay, Washington / by Brian F. Atwater and Eileen Hemphill-Haley; prepared in cooperation with the Nuclear Regulatory Commission. *U.S. Geological Survey Professional Paper*, *1576*.

Atwater, B. F., Musumi-Rokkaku, S., Satake, K., Tsuji, Y., & Yamaguchi, D. K. (2011). *The Orphan Tsunami of 1700: Japanese Clues to a Parent Earthquake in North America*. University of Washington Press.

Atwater, B. F., Nelson, A. R., Clague, J. J., Carver, G. A., Yamaguchi, D. K., Bobrowsky, P. T., Bourgeois, J., Darienzo, M. E., Grant, W. C., Hemphill-Haley, E., Kelsey, H. M., Jacoby, G. C., Nishenko, S. P., Palmer, S. P., Peterson, C. D., & Reinhart, M. A. (1995). Summary of Coastal Geologic Evidence for past Great Earthquakes at the Cascadia Subduction Zone. *Earthquake Spectra*, *11*(1), 1–18. https://doi.org/10.1193/1.1585800

Barlow, N. L. M., Long, A. J., Saher, M. H., Gehrels, W. R., Garnett, M. H., & Scaife, R. G. (2014). Salt-marsh reconstructions of relative sea-level change in the North Atlantic during the last 2000 years. *Quaternary Science Reviews*, *99*, 1–16. https://doi.org/10.1016/j.quascirev.2014.06.008

Barlow, N. L. M., Shennan, I., Long, A. J., Gehrels, W. R., Saher, M. H., Woodroffe, S. A., & Hillier, C. (2013). Salt marshes as late Holocene tide gauges. *Global and Planetary Change*, *106*, 90–110. https://doi.org/10.1016/j.gloplacha.2013.03.003

Barnett, R. L., Bernatchez, P., Garneau, M., & Juneau, M.-N. (2017). Reconstructing late Holocene relative sea-level changes at the Magdalen Islands (Gulf of St. Lawrence, Canada) using multi-proxy analyses. *Journal of Quaternary Science*, *32*(3), 380–395. https://doi.org/10.1002/jqs.2931

Barnett, R. L., Gehrels, W. R., Charman, D. J., Saher, M. H., & Marshall, W. A. (2015). Late Holocene sea-level change in Arctic Norway. *Quaternary Science Reviews*, *107*, 214–230. https://doi.org/10.1016/j.quascirev.2014.10.027

Beckhoff, B., Kanngießer, B., Langhoff, N., Wedell, R., Wolff, H., & Kanngießer, B. (2006). *Handbook of Practical X-Ray Fluorescence Analysis*. Springer Berlin / Heidelberg. http://ebookcentral.proquest.com/lib/sfu-ebooks/detail.action?docID=302069

Behre, K.-E. (1986). Analysis of botanical macro-remains. In *Sea-level Research: A Manual for the Collection and Evaluation of Data* (pp. 413–433). Geo Books.

Benson, B. E., Grimm, K. A., & Clague, J. J. (1997). Tsunami Deposits beneath Tidal Marshes on Northwestern Vancouver Island, British Columbia. *Quaternary Research*, *48*(2), 192–204. https://doi.org/10.1006/qres.1997.1911

Biester, H., Selimovic, D., Hemmerich, S., & Petri, M. (2005). Halogens in porewater of peat bogs—The role of peat decomposition and dissolved organic matter. *Biogeosciences Discussions*, *2*, 1457–1486.

Birks, H. J. B. (1995). Quantitative Paleoenvironmental Reconstructions. In *Statistical Modelling of Quaternary Science Data* (pp. 161–236).

Bohr, N. (1913). I. On the constitution of atoms and molecules. *The London, Edinburgh, and Dublin Philosophical Magazine and Journal of Science*, *26*(151), 1–25. https://doi.org/10.1080/14786441308634955

Brader, M., Garrett, E., Melnick, D., & Shennan, I. (2021). Sensitivity of tidal marshes as recorders of major megathrust earthquakes: Constraints from the 25 December 2016 Mw 7.6 Chiloé earthquake, Chile. *Journal of Quaternary Science*, *36*(6), 991–1002. https://doi.org/10.1002/jqs.3323

Briggs, R. W., Engelhart, S. E., Nelson, A. R., Dura, T., Kemp, A. C., Haeussler, P. J., Corbett, D. R., Angster, S. J., & Bradley, L.-A. (2014). Uplift and subsidence reveal a nonpersistent megathrust rupture boundary (Sitkinak Island, Alaska). *Geophysical Research Letters*, *41*(7), 2289–2296. https://doi.org/10.1002/2014GL059380

Cahill, N., Kemp, A. C., Horton, B. P., & Parnell, A. C. (2016). A Bayesian hierarchical model for reconstructing relative sea level: From raw data to rates of change. *Climate of the Past*, *12*(2), 525–542. https://doi.org/10.5194/cp-12-525-2016

Chagué-Goff, C., Chan, J. C. H., Goff, J., & Gadd, P. (2016). Late Holocene record of environmental changes, cyclones and tsunamis in a coastal lake, Mangaia, Cook Islands. *Island Arc*, *25*(5), 333–349. https://doi.org/10.1111/iar.12153

Chawchai, S., Chabangborn, A., Fritz, S., Väliranta, M., Mörth, C.-M., Blaauw, M., Reimer, P. J., Krusic, P. J., Löwemark, L., & Wohlfarth, B. (2015). Hydroclimatic shifts in northeast Thailand during the last two millennia – the record of Lake Pa Kho. *Quaternary Science Reviews*, *111*, 62–71. https://doi.org/10.1016/j.quascirev.2015.01.007

Chawchai, S., Kylander, M. E., Chabangborn, A., Löwemark, L., & Wohlfarth, B. (2016). Testing commonly used X-ray fluorescence core scanning-based proxies for organic-rich lake sediments and peat. *Boreas*, *45*(1), 180–189. https://doi.org/10.1111/bor.12145

Clague, J. J., & Bobrowsky, P. T. (1994). Tsunami deposits beneath tidal marshes on Vancouver Island, British Columbia. *Geological Society of America Bulletin*, *106*(10), 1293–1303. https://doi.org/10.1130/0016-7606(1994)106<1293:TDBTMO>2.3.CO;2

Clague, J. J., Bobrowsky, P. T., & Hamilton, T. S. (1994). A Sand Sheet Deposited by the 1964 Alaska Tsunami at Port Alberni, British Columbia. *Estuarine, Coastal and Shelf Science*, *38*(4), 413–421. https://doi.org/10.1006/ecss.1994.1028

Clague, J. J., Bobrowsky, P. T., & Hutchinson, I. (2000). A review of geological records of large tsunamis at Vancouver Island, British Columbia, and implications for hazard. *Quaternary Science Reviews*, *19*(9), 849–863. https://doi.org/10.1016/S0277-3791(99)00101-8

Clague, J. J., Hutchinson, I., Mathewes, R. W., & Patterson, R. T. (1999). Evidence for Late Holocene Tsunamis at Catala Lake, British Columbia. *Journal of Coastal Research*, *15*(1), 45–60.

Clague, J. J., & Ward, B. (2011). Pleistocene glaciation of british columbia. *Developments in Quaternary Science*, *15*, 563–573. https://doi.org/10.1016/B978-0-444-53447-7.00044-1

Clark, K. J., Hayward, B. W., Cochran, U. A., Wallace, L. M., Power, W. L., & Sabaa, A. T. (2015). Evidence for Past Subduction Earthquakes at a Plate Boundary with Widespread Upper Plate Faulting: Southern Hikurangi Margin, New Zealand. *Bulletin of the Seismological Society of America*, *105*(3), 1661–1690. https://doi.org/10.1785/0120140291

Cochran, U., Hannah, M., Harper, M., Van Dissen, R., Berryman, K., & Begg, J. (2007). Detection of large, Holocene earthquakes using diatom analysis of coastal sedimentary sequences, Wellington, New Zealand. *Quaternary Science Reviews*, *26*(7), 1129–1147. https://doi.org/10.1016/j.quascirev.2007.01.008

Croudace, I. W., Rindby, A., & Rothwell, R. G. (2006). ITRAX: Description and evaluation of a new multi-function X-ray core scanner. *Geological Society, London, Special Publications*, *267*(1), 51–63. https://doi.org/10.1144/GSL.SP.2006.267.01.04

Croudace, I. W., Teasdale, P. A., & Cundy, A. B. (2019). 200-year industrial archaeological record preserved in an Isle of Man saltmarsh sediment sequence: Geochemical and radiochronological evidence. *Quaternary International*, *514*, 195–203. https://doi.org/10.1016/j.quaint.2018.09.045

Davison, W. (1993). Iron and manganese in lakes. *Earth-Science Reviews*, *34*(2), 119–163. https://doi.org/10.1016/0012-8252(93)90029-7

DeBari, S. M., Anderson, R. G., & Mortensen, J. K. (1999). *Correlation among lower to upper crustal components in an island arc: The Jurassic Bonanza arc, Vancouver Island, Canada*. *36*.

Dragert, H., Hyndman, R. D., Rogers, G. C., & Wang, K. (1994). Current deformation and the width of the seismogenic zone of the northern Cascadia subduction thrust. *Journal of Geophysical Research: Solid Earth*, *99*(B1), 653–668. https://doi.org/10.1029/93JB02516

Dura, T., Cisternas, M., Horton, B. P., Ely, L. L., Nelson, A. R., Wesson, R. L., & Pilarczyk, J. E. (2015a). Coastal evidence for Holocene subduction-zone earthquakes and tsunamis in central Chile. *Quaternary Science Reviews*, *113*, 93–111. https://doi.org/10.1016/j.quascirev.2014.10.015

Dura, T., Cisternas, M., Horton, B. P., Ely, L. L., Nelson, A. R., Wesson, R. L., & Pilarczyk, J. E. (2015b). Coastal evidence for Holocene subduction-zone earthquakes and tsunamis in central Chile. *Quaternary Science Reviews*, *113*, 93–111. https://doi.org/10.1016/j.quascirev.2014.10.015

Dura, T., Engelhart, S. E., Vacchi, M., Horton, B. P., Kopp, R. E., Peltier, W. R., & Bradley, S. (2016a). The Role of Holocene Relative Sea-Level Change in Preserving Records of Subduction Zone Earthquakes. *Current Climate Change Reports*, *2*(3), 86–100. https://doi.org/10.1007/s40641-016-0041-y

Dura, T., Engelhart, S. E., Vacchi, M., Horton, B. P., Kopp, R. E., Peltier, W. R., & Bradley, S. (2016b). The Role of Holocene Relative Sea-Level Change in Preserving Records of Subduction Zone Earthquakes. *Current Climate Change Reports*, *2*(3), 86–100. https://doi.org/10.1007/s40641-016-0041-y

Dura, T., Hemphill-Haley, E., Sawai, Y., & Horton, B. P. (2016). The application of diatoms to reconstruct the history of subduction zone earthquakes and tsunamis. *Earth-Science Reviews*, *152*, 181–197. https://doi.org/10.1016/j.earscirev.2015.11.017

Dura, T., Horton, B. P., Cisternas, M., Ely, L. L., Hong, I., Nelson, A. R., Wesson, R. L., Pilarczyk, J. E., Parnell, A. C., & Nikitina, D. (2017). Subduction zone slip variability during the last millennium, south-central Chile. *Quaternary Science Reviews*, *175*, 112–137. https://doi.org/10.1016/j.quascirev.2017.08.023

Dura, T., Rubin, C. M., Kelsey, H. M., Horton, B. P., Hawkes, A., Vane, C. H., Daryono, M., Pre, C. G., Ladinsky, T., & Bradley, S. (2011). Stratigraphic record of Holocene coseismic subsidence, Padang, West Sumatra. *Journal of Geophysical Research: Solid Earth*, *116*(B11). https://doi.org/10.1029/2011JB008205

Emmett, R., Llansó, R., Newton, J., Thom, R., Hornberger, M., Morgan, C., Levings, C., Copping, A., Fishman, P., & Llanso, R. (2000). Geographic Signatures of North American West Coast Estuaries. *Estuaries*, *23*(6), 765. https://doi.org/10.2307/1352998

Engelhart, S. E., Horton, B. P., Nelson, A. R., Hawkes, A. D., Witter, R. C., Wang, K., Wang, P.-L., & Vane, C. H. (2013). Testing the use of microfossils to reconstruct great earthquakes at Cascadia. *Geology*, *41*(10), 1067–1070. https://doi.org/10.1130/G34544.1

Engelhart, S. E., Vacchi, M., Horton, B. P., Nelson, A. R., & Kopp, R. E. (2015). A sea-level database for the Pacific coast of central North America. *Quaternary Science Reviews*, *113*, 78–92. https://doi.org/10.1016/j.quascirev.2014.12.001

Evelpidou, N., Kampolis, I., Pirazzoli, P. A., & Vassilopoulos, A. (2012). Global sea-level rise and the disappearance of tidal notches. *Global and Planetary Change*, *92–93*, 248–256. https://doi.org/10.1016/j.gloplacha.2012.05.013

Fernández, J. E. (1992). Rayleigh and compton scattering contributions to x-ray fluorescence intensity. *X-Ray Spectrometry*, *21*(2), 57–68. https://doi.org/10.1002/xrs.1300210204

Fisheries and Oceans Canada (DFO), F. and O. C. (2023). *Tides, currents, and water levels*. Port Alberni - 08575. https://www.tides.gc.ca/en/stations/8575

Garrett, E., Brain, M. J., Hayward, B. W., Newnham, R., Morey, C. J., & Gehrels, W. R. (2023). Resolving Uncertainties in Foraminifera-Based Relative Sea-Level Reconstruction: A Case Study from Southern New Zealand. *Journal of Foraminiferal Research*, *53*(1), 78–89. https://doi.org/10.2113/gsjfr.53.1.78

Garrett, E., Fujiwara, O., Garrett, P., Heyvaert, V. M. A., Shishikura, M., Yokoyama, Y., Hubert-Ferrari, A., Brückner, H., Nakamura, A., & De Batist, M. (2016). A systematic review of geological evidence for Holocene earthquakes and tsunamis along the Nankai-Suruga Trough, Japan. *Earth-Science Reviews*, *159*, 337–357. https://doi.org/10.1016/j.earscirev.2016.06.011

Garrett, E., Shennan, I., Watcham, E. P., & Woodroffe, S. A. (2013). Reconstructing paleoseismic deformation, 1: Modern analogues from the 1960 and 2010 Chilean great earthquakes. *Quaternary Science Reviews*, *75*, 11–21. https://doi.org/10.1016/j.quascirev.2013.04.007

Garrett, E., Shennan, I., Woodroffe, S. A., Cisternas, M., Hocking, E. P., & Gulliver, P. (2015). Reconstructing paleoseismic deformation, 2: 1000 years of great earthquakes at Chucalén, south central Chile. *Quaternary Science Reviews*, *113*, 112–122. https://doi.org/10.1016/j.quascirev.2014.10.010

Goff, J., Bobrowsky, P., Huntley, D., Sawai, Y., & Tanagawa, K. (2020). Palaeotsunamis along Canada's Pacific coast. *Quaternary Science Reviews*, *237*, 106309. https://doi.org/10.1016/j.quascirev.2020.106309

Goldfinger, C., Nelson, C. H., Morey, A. E., Johnson, J. E., Patton, J. R., Karabanov, E. B., Gutierrez-Pastor, J., Eriksson, A. T., Gracia, E., Dunhill, G., Enkin, R. J., Dallimore, A., & Vallier, T. (2012a). Turbidite event history—Methods and implications for Holocene paleoseismicity of the Cascadia subduction zone. In *Professional Paper* (1661-F). U.S. Geological Survey. https://doi.org/10.3133/pp1661F

Goldfinger, C., Nelson, C. H., Morey, A. E., Johnson, J. R., Patton, J., Karabanov, E., Gutierrez-Pastor, J., Eriksson, A. T., Gracia, E., Dunhill, G., Enkin, R. J., Dallimore, A., & Vallier, T. (2012b). Turbidite Event History—Methods and Implications for Holocene Paleoseismicity of the Cascadia Subduction Zone. *U.S. Geological Survey Professional Paper*, *1661-F*(170).

Graehl, N. A., Kelsey, H. M., Witter, R. C., Hemphill-Haley, E., & Engelhart, S. E. (2015). Stratigraphic and microfossil evidence for a 4500-year history of Cascadia subduction zone earthquakes and tsunamis at Yaquina River estuary, Oregon, USA. *GSA Bulletin*, *127*(1–2), 211–226. https://doi.org/10.1130/B31074.1

Grand Pre, C. A., Horton, B. P., Kelsey, H. M., Rubin, C. M., Hawkes, A. D., Daryono, M. R., Rosenberg, G., & Culver, S. J. (2012). Stratigraphic evidence for an early Holocene earthquake in Aceh, Indonesia. *Quaternary Science Reviews*, *54*, 142–151. https://doi.org/10.1016/j.quascirev.2012.03.011

Gregory, B. R. B., Patterson, R. T., Galloway, J. M., & Reinhardt, E. G. (2021). The impact of cyclical, multi-decadal to centennial climate variability on arsenic sequestration in lacustrine sediments. *Palaeogeography, Palaeoclimatology, Palaeoecology*, *565*, 110189. https://doi.org/10.1016/j.palaeo.2020.110189

Gregory, B. R. B., Patterson, R. T., Reinhardt, E. G., Galloway, J. M., & Roe, H. M. (2019). An evaluation of methodologies for calibrating Itrax X-ray fluorescence counts with ICP-MS concentration data for discrete sediment samples. *Chemical Geology*, *521*, 12–27. https://doi.org/10.1016/j.chemgeo.2019.05.008

Gregory, B. R. B., Reinhardt, E. G., Macumber, A. L., Nasser, N. A., Patterson, R. T., Kovacs, S. E., & Galloway, J. M. (2017). Sequential sample reservoirs for Itrax-XRF analysis of discrete samples. *Journal of Paleolimnology*, *57*(3), 287–293. https://doi.org/10.1007/s10933-017-9944-4

Guilbault, J.-P., Clague, J. J., & Lapointe, M. (1995). Amount of subsidence during a late Holocene earthquake—Evidence from fossil tidal marsh foraminifera at Vancouver Island, west coast of Canada. *Palaeogeography, Palaeoclimatology, Palaeoecology*, *118*(1–2), 49–71. https://doi.org/10.1016/0031-0182(94)00135-U

Guilbault, J.-P., Clague, J. J., & Lapointe, M. (1996). Foraminiferal evidence for the amount of coseismic subsidence during a late holocene earthquake on Vancouver Island, West Coast of Canada. *Quaternary Science Reviews*, *15*(8–9), 913–937. https://doi.org/10.1016/S0277-3791(96)00058-3

Guyard, H., Chapron, E., St-Onge, G., Anselmetti, F. S., Arnaud, F., Magand, O., Francus, P., & Mélières, M.-A. (2007). High-altitude varve records of abrupt environmental changes and mining activity over the last 4000 years in the Western French Alps (Lake Bramant, Grandes Rousses Massif). *Quaternary Science Reviews*, *26*(19), 2644–2660. https://doi.org/10.1016/j.quascirev.2007.07.007

Hahn, A., Kliem, P., Oehlerich, M., Ohlendorf, C., Zolitschka, B., & the PASADO Science Team. (2014). Elemental composition of the Laguna Potrok Aike sediment sequence reveals paleoclimatic changes over the past 51 ka in southern Patagonia, Argentina. *Journal of Paleolimnology*, *52*(4), 349–366. https://doi.org/10.1007/s10933-014-9798-y

Hawkes, A. D., Horton, B. P., Nelson, A. R., & Hill, D. F. (2010). The application of intertidal foraminifera to reconstruct coastal subsidence during the giant Cascadia earthquake of AD 1700 in Oregon, USA. *Quaternary International*, *221*(1–2), 116–140. https://doi.org/10.1016/j.quaint.2009.09.019

Hawkes, A. D., Horton, B. P., Nelson, A. R., Vane, C. H., & Sawai, Y. (2011). Coastal subsidence in Oregon, USA, during the giant Cascadia earthquake of AD 1700. *Quaternary Science Reviews*, *30*(3–4), 364–376. https://doi.org/10.1016/j.quascirev.2010.11.017

Hayward, B. W., Grenfell, H. R., Sabaa, A. T., Cochran, U. A., Clark, K. J., Wallace, L., & Palmer, A. S. (2016). Salt-marsh foraminiferal record of 10 large Holocene (last 7500 yr) earthquakes on a subducting plate margin, Hawkes Bay, New Zealand. *GSA Bulletin*, *128*(5–6), 896–915. https://doi.org/10.1130/B31295.1

Heil, J., Häring, V., Marschner, B., & Stumpe, B. (2019). Advantages of fuzzy k-means over k-means clustering in the classification of diffuse reflectance soil spectra: A case study with West African soils. *Geoderma*, *337*, 11–21. https://doi.org/10.1016/j.geoderma.2018.09.004

Hein, C. J., FitzGERALD, D. M., Cleary, W. J., Albernaz, M. B., De MENEZES, J. T., & Klein, A. H. da F. (2013). Evidence for a transgressive barrier within a regressive strandplain system: Implications for complex coastal response to environmental change. *Sedimentology*, *60*(2), 469–502. https://doi.org/10.1111/j.1365-3091.2012.01348.x

Hemphill-Haley, E. (1995). Diatom evidence for earthquake-induced subsidence and tsunami 300 yr ago in southern coastal Washington. *Geological Society of America Bulletin*, *107*(3), 367–378.

Hennekam, R., Sweere, T., Tjallingii, R., de Lange, G. J., & Reichart, G.-J. (2019). Trace metal analysis of sediment cores using a novel X-ray fluorescence core scanning method. *Quaternary International*, *514*, 55–67. https://doi.org/10.1016/j.quaint.2018.10.018

Hocking, E. P., Garrett, E., & Cisternas, M. (2017). Modern diatom assemblages from Chilean tidal marshes and their application for quantifying deformation during past great earthquakes. *Journal of Quaternary Science*, *32*(3), 396–415. https://doi.org/10.1002/jqs.2933

Hong, I., Horton, B. P., Hawkes, A. D., O'Donnell, R. J., Padgett, J. S., Dura, T., & Engelhart, S. E. (2021). Diatoms of the intertidal environments of Willapa Bay, Washington, USA as a sea-level indicator. *Marine Micropaleontology*, *167*, 102033. https://doi.org/10.1016/j.marmicro.2021.102033

Horton, B. P., & Edwards, R. J. (2006). Quantifying Holocene sea-level change using intertidal foraminifera: Lessons from the British Isles. *Cushman Found. Foram. Res. Spec. Publ.*, *40*(1), 97. https://doi.org/10.11137/2006_1_541-542

Hubert, L., & Arabie, P. (1985). Comparing partitions. *Journal of Classification*, *2*(1), 193–218. https://doi.org/10.1007/BF01908075

Hutchinson, I., & Clague, J. (2017a). Were they all giants? Perspectives on late Holocene plate-boundary earthquakes at the northern end of the Cascadia subduction zone. *Quaternary Science Reviews*, *169*, 29–49. https://doi.org/10.1016/j.quascirev.2017.05.015

Hutchinson, I., & Clague, J. (2017b). Were they all giants? Perspectives on late Holocene plate-boundary earthquakes at the northern end of the Cascadia subduction zone. *Quaternary Science Reviews*, *169*, 29–49. https://doi.org/10.1016/j.quascirev.2017.05.015

Injuk, J., Van Grieken, R., Blank, A., Eksperiandova, L., & Buhrke, V. (2006). Specimen Preparation. In *Handbook of Practical X-Ray Fluorescence Analysis* (pp. 411–432). Springer Berlin / Heidelberg.

Ishizawa, T., Goto, K., Yokoyama, Y., & Miyairi, Y. (2019). Non-destructive analyses to determine appropriate stratigraphic level for dating of tsunami deposits. *Marine Geology*, *412*, 19–26. https://doi.org/10.1016/j.margeo.2019.02.009

Jenkins, R. (1999). Production and Properties X-Rays. In *X-Ray Fluorescence Spectrometry* (2nd ed., Vol. 152). https://onlinelibrary.wiley.com/doi/chapter-epub/10.1002/9781118521014.ch1

Jonasson, K. E., & Patterson, R. T. (1992). Preservation Potential of Salt Marsh Foraminifera from the Fraser River Delta, British Columbia. *Micropaleontology*, *38*(3), 289–301. https://doi.org/10.2307/1485793

Jones, A. F., Turner, J. N., Daly, J. S., Francus, P., & Edwards, R. J. (2019). Signal-to-noise ratios, instrument parameters and repeatability of Itrax XRF core scan measurements of floodplain sediments. *Quaternary International*, *514*, 44–54. https://doi.org/10.1016/j.quaint.2018.09.006

Kaboth-Bahr, S., Denis, V., Su, C.-C., O'Regan, M., Gyllencreutz, R., Jakobsson, M., & Löwemark, L. (2019). Deciphering ~45.000 years of Arctic Ocean lithostratigraphic variability through multivariate statistical analysis. *Quaternary International*, *514*, 141–151. https://doi.org/10.1016/j.quaint.2018.11.043

Kaufman, L., & Rousseeuw, P. (1990). Partitioning Around Medoids (Program PAM). In *Finding Groups in Data* (pp. 68–125). John Wiley & Sons, Ltd. https://doi.org/10.1002/9780470316801.ch2

Kelsey, H. M., Witter, R. C., & Hemphill-Haley, E. (2002). Plate-boundary earthquakes and tsunamis of the past 5500 yr, Sixes River estuary, southern Oregon. *GSA Bulletin*, *114*(3), 298–314. https://doi.org/10.1130/0016-7606(2002)114<0298:PBEATO>2.0.CO;2

Kemp, A. C., Cahill, N., Engelhart, S. E., Hawkes, A. D., & Wang, K. (2018a). Revising Estimates of Spatially Variable Subsidence during the A.D. 1700 Cascadia Earthquake Using a Bayesian Foraminiferal Transfer Function. *Bulletin of the Seismological Society of America*, *108*(2), 654–673. https://doi.org/10.1785/0120170269

Kemp, A. C., Cahill, N., Engelhart, S. E., Hawkes, A. D., & Wang, K. (2018b). Revising Estimates of Spatially Variable Subsidence during the A.D. 1700 Cascadia Earthquake Using a Bayesian Foraminiferal Transfer Function. *Bulletin of the Seismological Society of America*, *108*(2), 654–673. https://doi.org/10.1785/0120170269

Kemp, A. C., Horton, B. P., Nikitina, D., Vane, C. H., Potapova, M., Weber-Bruya, E., Culver, S. J., Repkina, T., & Hill, D. F. (2017). The distribution and utility of sea-level indicators in Eurasian sub-Arctic salt marshes (White Sea, Russia). *Boreas*, *46*(3), 562–584. https://doi.org/10.1111/bor.12233

Kemp, A. C., Horton, B. P., Vane, C. H., Bernhardt, C. E., Corbett, D. R., Engelhart, S. E., Anisfeld, S. C., Parnell, A. C., & Cahill, N. (2013). Sea-level change during the last 2500 years in New Jersey, USA. *Quaternary Science Reviews*, *81*, 90–104. https://doi.org/10.1016/j.quascirev.2013.09.024

Kemp, A. C., Horton, B. P., Vann, D. R., Engelhart, S. E., Grand Pre, C. A., Vane, C. H., Nikitina, D., & Anisfeld, S. C. (2012). Quantitative vertical zonation of salt-marsh foraminifera for reconstructing former sea level; an example from New Jersey, USA. *Quaternary Science Reviews*, *54*, 26–39. https://doi.org/10.1016/j.quascirev.2011.09.014

Kemp, A. C., Vane, C. H., Horton, B. P., & Culver, S. J. (2010). Stable carbon isotopes as potential sea-level indicators in salt marshes, North Carolina, USA. *The Holocene*, *20*(4), 623–636. https://doi.org/10.1177/0959683609354302

Kemp, A. C., Vane, C. H., Khan, N. S., Ellison, J. C., Engelhart, S. E., Horton, B. P., Nikitina, D., Smith, S. R., Rodrigues, L. J., & Moyer, R. P. (2019). Testing the Utility of Geochemical Proxies to Reconstruct Holocene Coastal Environments and Relative Sea Level: A Case Study from Hungry Bay, Bermuda. *Open Quaternary*, *5*, 1. https://doi.org/10.5334/oq.49

Keppler, F., Eiden, R., Niedan, V., Pracht, J., & Schöler, H. F. (2000). Halocarbons produced by natural oxidation processes during degradation of organic matter. *Nature*, *403*(6767), Article 6767. https://doi.org/10.1038/35002055

Khan, N. S., Vane, C. H., Engelhart, S. E., Kendrick, C., & Horton, B. P. (2019). The application of δ13C, TOC and C/N geochemistry of mangrove sediments to reconstruct Holocene paleoenvironments and relative sea levels, Puerto Rico. *Marine Geology*, *415*, 105963. https://doi.org/10.1016/j.margeo.2019.105963

Kovacs, S. E., Reinhardt, E. G., Chatters, J. C., Rissolo, D., Schwarcz, H. P., Collins, S. V., Kim, S.-T., Nava Blank, A., & Luna Erreguerena, P. (2017). Calcite raft geochemistry as a hydrological proxy for Holocene aquifer conditions in Hoyo Negro and Ich Balam (Sac Actun Cave System), Quintana Roo, Mexico. *Quaternary Science Reviews*, *175*, 97–111. https://doi.org/10.1016/j.quascirev.2017.09.006

Kylander, M. E., Ampel, L., Wohlfarth, B., & Veres, D. (2011). High-resolution X-ray fluorescence core scanning analysis of Les Echets (France) sedimentary sequence: New insights from chemical proxies. *Journal of Quaternary Science*, *26*(1), 109–117. https://doi.org/10.1002/jqs.1438

Lacey, J. H., Francke, A., Leng, M. J., Vane, C. H., & Wagner, B. (2015). A high-resolution Late Glacial to Holocene record of environmental change in the Mediterranean from Lake Ohrid (Macedonia/Albania). *International Journal of Earth Sciences : Geologische Rundschau*, *104*(6), 1623–1638. https://doi.org/10.1007/s00531-014-1033-6

Lafargue, E., Marquis, F., & Pillot, D. (1998). Rock-Eval 6 Applications in Hydrocarbon Exploration, Production, and Soil Contamination Studies. *Revue de l'Institut Français Du Pétrole*, *53*(4), Article 4. https://doi.org/10.2516/ogst:1998036

Lallier-Verges, E., Perrussel, B. P., Disnar, J.-R., & Baltzer, F. (1998). Relationships between environmental conditions and the diagenetic evolution of organic matter derived from higher plants in a modern mangrove swamp system (Guadeloupe, French West Indies). *Organic Geochemistry*, *29*(5), 1663–1686. https://doi.org/10.1016/S0146-6380(98)00179-X

Lamb, A. L., Wilson, G. P., & Leng, M. J. (2006). A review of coastal palaeoclimate and relative sea-level reconstructions using δ13C and C/N ratios in organic material. *Earth-Science Reviews*, *75*(1), 29–57. https://doi.org/10.1016/j.earscirev.2005.10.003

Leonard, L. J., Currie, C. A., Mazzotti, S., & Hyndman, R. D. (2010). Rupture area and displacement of past Cascadia great earthquakes from coastal coseismic subsidence. *Bulletin of the Geological Society of America*, *122*(11–12), 2079–2096. https://doi.org/10.1130/B30108.1

Little, T. A., Van Dissen, R., Schermer, E., & Carne, R. (2009). Late Holocene surface ruptures on the southern Wairarapa fault, New Zealand: Link between earthquakes and the uplifting of beach ridges on a rocky coast. *Lithosphere*, *1*(1), 4–28. https://doi.org/10.1130/L7.1

Longman, J., Ersek, V., Veres, D., & Salzmann, U. (2017). Detrital events and hydroclimate variability in the Romanian Carpathians during the mid-to-late Holocene. *Quaternary Science Reviews*, *167*, 78–95. https://doi.org/10.1016/j.quascirev.2017.04.029

Longman, J., Veres, D., & Wennrich, V. (2019). Utilisation of XRF core scanning on peat and other highly organic sediments. *Quaternary International*, *514*, 85–96. https://doi.org/10.1016/j.quaint.2018.10.015

López Pérez, A. E., Rey, D., Martins, V., Plaza-Morlote, M., & Rubio, B. (2019). Application of multivariate statistical analyses to Itrax core scanner data for the identification of deep-marine sedimentary facies: A case study in the Galician Continental Margin. *Quaternary International*, *514*, 152–160. https://doi.org/10.1016/j.quaint.2018.06.035

Löwemark, L., Bloemsma, M., Croudace, I., Daly, J. S., Edwards, R. J., Francus, P., Galloway, J. M., Gregory, B. R. B., Steven Huang, J.-J., Jones, A. F., Kylander, M., Löwemark, L., Luo, Y., Maclachlan, S., Ohlendorf, C., Patterson, R. T., Pearce, C., Profe, J., Reinhardt, E. G., … Turner, J. N. (2019). Practical guidelines and recent advances in the Itrax XRF core-scanning procedure. *Quaternary International*, *514*, 16–29. https://doi.org/10.1016/j.quaint.2018.10.044

Ludwin, R. S., Dennis, R., Carver, D., McMillan, A. D., Losey, R., Clague, J., Jonientz-Trisler, C., Bowechop, J., Wray, J., & James, K. (2005). Dating the 1700 Cascadia Earthquake: Great Coastal Earthquakes in Native Stories. *Seismological Research Letters*, *76*(2), 140–148. https://doi.org/10.1785/gssrl.76.2.140

Macdonald, K., & Barbour, M. (1977). Beach and Salt Marsh Vegetation of the North American Pacific Coast. In *Ecology of Halophytes* (pp. 175–233). Elsevier.

MacQueen, J. (1967). SOME METHODS FOR CLASSIFICATION AND ANALYSIS OF MULTIVARIATE OBSERVATIONS. *Proceedings of the Fifth Berkeley Symposium on Mathematical Statistics and Probability*, *1*, 281–297.

Massey, N. W. D., & Friday, S. J. (1988). GEOLOGY OF THE ALBERNI - NANAIMO LAKES AREA, VANCOUVER ISLAND. *British Columbia Ministry of Energy, Mintes and Petroleum Resources*, *1989–1*.

Mathewes, R. W., & Clague, J. J. (1994). Detection of Large Prehistoric Earthquakes in the Pacific Northwest by Microfossil Analysis. *Science*, *264*(5159), 688–691.

McCaffrey, R., King, R. W., Payne, S. J., & Lancaster, M. (2013). Active tectonics of northwestern U.S. inferred from GPS-derived surface velocities. *Journal of Geophysical Research: Solid Earth*, *118*(2), 709–723. https://doi.org/10.1029/2012JB009473

McMillan, A. D., & Hutchinson, I. (2002). When the Mountain Dwarfs Danced: Aboriginal Traditions of Paleoseismic Events along the Cascadia Subduction Zone of Western North America. *Ethnohistory*, *49*(1), 41–68. https://doi.org/10.1215/00141801-49-1-41

Milker, Y., Horton, B. P., Nelson, A. R., Engelhart, S. E., & Witter, R. C. (2015). Variability of intertidal foraminiferal assemblages in a salt marsh, Oregon, USA. *Marine Micropaleontology*, *118*, 1–16. https://doi.org/10.1016/j.marmicro.2015.04.004

Miller, M. M., Johnson, D. J., Rubin, C. M., Dragert, H., Wang, K., Qamar, A., & Goldfinger, C. (2001). GPS-determination of along-strike variation in Cascadia margin kinematics: Implications for relative plate motion, subduction zone coupling, and permanent deformation. *Tectonics*, *20*(2), 161–176. https://doi.org/10.1029/2000TC001224

Mondal, M. N., Horikawa, K., Seki, O., Nejigaki, K., Minami, H., Murayama, M., & Okazaki, Y. (2021). Investigation of Adequate Calibration Methods for X-ray Fluorescence Core Scanning Element Count Data: A Case Study of a Marine Sediment Piston Core from the Gulf of Alaska. *Journal of Marine Science and Engineering*, *9*(5), 540. https://doi.org/10.3390/jmse9050540

Moreira, S., Costa, P. J. M., Andrade, C., Ponte Lira, C., Freitas, M. C., Oliveira, M. A., & Reichart, G.-J. (2017). High resolution geochemical and grain-size analysis of the AD 1755 tsunami deposit: Insights into the inland extent and inundation phases. *Marine Geology*, *390*, 94–105. https://doi.org/10.1016/j.margeo.2017.04.007

Mushet, G. R., Reinhardt, E. G., Whitehouse, R., & Cumming, B. F. (2022). Postglacial hydroclimate in the southern interior of British Columbia (Canada): Lake ecosystem response to the Holocene Thermal Maximum and drivers of mid-to-late Holocene climate variability. *Quaternary Science Reviews*, *276*, 107302. https://doi.org/10.1016/j.quascirev.2021.107302

National Oceanic and Atmospheric Administration (NOAA). (2023). *NOAA Tides & Currents*. Bay Center, Palix River, Willapa Bay, WA - Station ID: 9440846. https://tidesandcurrents.noaa.gov/stationhome.html?id=9440846

Nelson, A. R., DuRoss, C. B., Witter, R. C., Kelsey, H. M., Engelhart, S. E., Mahan, S. A., Gray, H. J., Hawkes, A. D., Horton, B. P., & Padgett, J. S. (2021). A maximum rupture model for the central and southern Cascadia subduction zone—Reassessing ages for coastal evidence of megathrust earthquakes and tsunamis. *Quaternary Science Reviews*, *261*, 106922. https://doi.org/10.1016/j.quascirev.2021.106922

Newell, A. J., Vane, C. H., Sorensen, J. P., Moss-Hayes, V., & Gooddy, D. C. (2016). Long-term Holocene groundwater fluctuations in a chalk catchment: Evidence from Rock-Eval pyrolysis of riparian peats. *Hydrological Processes*, *30*(24), 4556–4567. https://doi.org/10.1002/hyp.10903

Oliva, F., Peros, M. C., Viau, A. E., Reinhardt, E. G., Nixon, F. C., & Morin, A. (2018). A multi-proxy reconstruction of tropical cyclone variability during the past 800 years from Robinson Lake, Nova Scotia, Canada. *Marine Geology*, *406*, 84–97. https://doi.org/10.1016/j.margeo.2018.09.012

Olsen, J., Björck, S., Leng, M. J., Gudmundsdóttir, E. R., Odgaard, B. V., Lutz, C. M., Kendrick, C. P., Andersen, T. J., & Seidenkrantz, M.-S. (2010). Lacustrine evidence of Holocene environmental change from three Faroese lakes: A multiproxy XRF and stable isotope study. *Quaternary Science Reviews*, *29*(19), 2764–2780. https://doi.org/10.1016/j.quascirev.2010.06.029

Padgett, J. S., Engelhart, S. E., Kelsey, H. M., Witter, R. C., & Cahill, N. (2022). Reproducibility and variability of earthquake subsidence estimates from saltmarshes of a Cascadia estuary. *Journal of Quaternary Science*, *37*(7), 1294–1312. https://doi.org/10.1002/jqs.3446

Paris, R., Sabatier, P., Biguenet, M., Bougouin, A., André, G., & Roger, J. (2021). A tsunami deposit at Anse Meunier, Martinique Island: Evidence of the 1755 CE Lisbon tsunami and implication for hazard assessment. *Marine Geology*, *439*, 106561. https://doi.org/10.1016/j.margeo.2021.106561

Patterson, R. T., Guilbault, J.-P., & Clague, J. J. (1999). Taphonomy of tidal marsh foraminifera: Implications of surface sample thickness for high-resolution sea-level studies. *Palaeogeography, Palaeoclimatology, Palaeoecology*, *149*(1), 199–211. https://doi.org/10.1016/S0031-0182(98)00201-6

Patterson, R. T., Mazzella, V., Macumber, A. L., Gregory, B. R. B., Patterson, C. W., Nasser, N. A., Roe, H. M., Galloway, J. M., & Reinhardt, E. G. (2020). A novel protocol for mapping the spatial distribution of storm derived sediment in lakes. *SN Applied Sciences*, *2*(12), 2125. https://doi.org/10.1007/s42452-020-03908-3

Peti, L., Augustinus, P. C., Gadd, P. S., & Davies, S. J. (2019). Towards characterising rhyolitic tephra layers from New Zealand with rapid, non-destructive μ-XRF core scanning. *Quaternary International*, *514*, 161–172. https://doi.org/10.1016/j.quaint.2018.06.039

Pilarczyk, J. E., Dura, T., Horton, B. P., Engelhart, S. E., Kemp, A. C., & Sawai, Y. (2014). Microfossils from coastal environments as indicators of paleo-earthquakes, tsunamis and storms. *Palaeogeography, Palaeoclimatology, Palaeoecology*, *413*, 144–157. https://doi.org/10.1016/j.palaeo.2014.06.033

Pilarczyk, J. E., Sawai, Y., Matsumoto, D., Namegaya, Y., Nishida, N., Ikehara, K., Fujiwara, O., Gouramanis, C., Dura, T., & Horton, B. P. (2020). Constraining sediment provenance for tsunami deposits using distributions of grain size and foraminifera from the Kujukuri coastline and shelf, Japan. *Sedimentology*, *67*(3), 1373–1392. https://doi.org/10.1111/sed.12591

Pojar, J., & MacKinnon, A. (1994). *Plants of the Pacific Northwest Coast: Washington, Oregon, British Columbia & Alaska.* Lone Pine Publishing.

R Core Team. (2021). *R: A Language and Environment for Statistical Computing* [Computer software]. R Foundation for Statistical Computing. https://www.R-project.org/

Rabinovich, A., Geist, E., Fritz, H., & Borrero, J. (2015). Introduction to “Tsunami Science: Ten Years After the 2004 Indian Ocean Tsunami. Volume I.” *Pure & Applied Geophysics*, *172*(3/4), 615–619. https://doi.org/10.1007/s00024-015-1038-5

Riddihough, R. (1984). Recent movements of the Juan de Fuca Plate System. *Journal of Geophysical Research: Solid Earth*, *89*(B8), 6980–6994. https://doi.org/10.1029/JB089iB08p06980

Riou, L. (2023). *A relative sea-level reconstruction in Port Alberni, British Columbia: Implications for Cascadia subduction zone earthqkes, tsunamis, and land-level change*. Simon Fraser University.

Rousseeuw, P. J. (1987). Silhouettes: A graphical aid to the interpretation and validation of cluster analysis. *Journal of Computational and Applied Mathematics*, *20*, 53–65. https://doi.org/10.1016/0377-0427(87)90125-7

Rubin, C. M., Horton, B. P., Sieh, K., Pilarczyk, J. E., Daly, P., Ismail, N., & Parnell, A. C. (2017). Highly variable recurrence of tsunamis in the 7,400 years before the 2004 Indian Ocean tsunami. *Nature Communications*, *8*(May). https://doi.org/10.1038/ncomms16019

Rush, G., McDarby, P., Edwards, R., Milker, Y., Garrett, E., & Gehrels, W. R. (2021). Development of an intertidal foraminifera training set for the North Sea and an assessment of its application for Holocene sea-level reconstructions. *Marine Micropaleontology*, *169*, 102055. https://doi.org/10.1016/j.marmicro.2021.102055

Sachs, H., Iii, T., & Clark, D. (1977). Paleoecological Transfer Functions. *Annual Review of Earth and Planetary Sciences*, *5*, 159–178. https://doi.org/10.1146/annurev.ea.05.050177.001111

Satake, K., Shimazaki, K., Tsuji, Y., & Ueda, K. (1996). Time and size of a giant earthquake in Cascadia inferred from Japanese tsunami records of January 1700. *Nature*, *379*(6562), Article 6562. https://doi.org/10.1038/379246a0

Sawai, Y., Horton, B. P., & Nagumo, T. (2004). The development of a diatom-based transfer function along the Pacific coast of eastern Hokkaido, northern Japan—An aid in paleoseismic studies of the Kuril subduction zone. *Quaternary Science Reviews*, *23*(23–24), 2467–2483. https://doi.org/10.1016/j.quascirev.2004.05.006

Sawai, Y., Namegaya, Y., Okamura, Y., Satake, K., & Shishikura, M. (2012). Challenges of anticipating the 2011 Tohoku earthquake and tsunami using coastal geology. *Geophysical Research Letters*, *39*(21), 1–6. https://doi.org/10.1029/2012GL053692

Sawai, Y., Satake, K., Kamataki, T., Nasu, H., Shishikura, M., Atwater, B. F., Horton, B. P., Kelsey, H. M., Nagumo, T., & Yamaguchi, M. (2004). Transient uplift after a 17th-century earthquake along the Kuril subduction zone. *Science*, *306*(5703), 1918–1920.

Sawai, Y., Tanigawa, K., Shinozaki, T., Bobrowsky, P., Huntley, D., & Goff, J. (2022). Diatom (Bacillariophyceae) assemblages in tidal environments of Vancouver Island, British Columbia, Canada. *Phycological Research*, *70*(1), 3–21. https://doi.org/10.1111/pre.12470

Scott, D. S., & Medioli, F. S. (1978). Vertical zonations of marsh foraminifera as accurate indicators of former sea-levels. *Nature*, *272*(5653), 528–531. https://doi.org/10.1038/272528a0

Shennan, I. (1986). Flandrian sea-level changes in the Fenland. I: The geographical setting and evidence of relative sea-level changes. *Journal of Quaternary Science*, *1*(2), 119–153. https://doi.org/10.1002/jqs.3390010204

Shennan, I., BARLOW, N., COMBELLICK, R., PIERRE, K., & STUART-TAYLOR, O. (2014). Late Holocene paleoseismology of a site in the region of maximum subsidence during the 1964 Mw 9.2 Alaska earthquake: PALEOSEISMOLOGY OF THE 1964 ALASKA EARTHQUAKE. *Journal of Quaternary Science*, *29*(4), 343–350. https://doi.org/10.1002/jqs.2705

Shennan, I., Brader, M. D., Barlow, N. L. M., Davies, F. P., Longley, C., & Tunstall, N. (2018). Late Holocene paleoseismology of Shuyak Island, Alaska. *Quaternary Science Reviews*, *201*, 380–395. https://doi.org/10.1016/j.quascirev.2018.10.028

Shennan, I., & Hamilton, S. (2006). Coseismic and pre-seismic subsidence associated with great earthquakes in Alaska. *Quaternary Science Reviews*, *25*(1), 1–8. https://doi.org/10.1016/j.quascirev.2005.09.002

Shennan, I., Long, A. J., Rutherford, M. M., Green, F. M., Innes, J. B., Lloyd, J. M., Zong, Y., & Walker, K. (1996a). A 5000-year record of large earthquakes and sea-level rise in Washington, USA, revealed by biostratigraphic analysis of intertidal sediments. *Quaternary Science Reviews*, *15*, 1–37. Scopus.

Shennan, I., Long, A. J., Rutherford, M. M., Green, F. M., Innes, J. B., Lloyd, J. M., Zong, Y., & Walker, K. J. (1996b). Tidal marsh stratigraphy, sea-level change and large earthquakes, i: A 5000 year record in washington, U.S.A. *Quaternary Science Reviews*, *15*(10), 1023–1059. https://doi.org/10.1016/S0277-3791(96)00007-8

Snelder, T. H., & J. Booker, D. (2013). Natural Flow Regime Classifications Are Sensitive to Definition Procedures. *River Research and Applications*, *29*(7), 822–838. https://doi.org/10.1002/rra.2581

Steele, R. E., Nasser, N. A., Patterson, R. T., Gregory, B. R. B., Roe, H. M., & Reinhardt, E. G. (2018). An Assessment of Sub-Meter Scale Spatial Variability of Arcellinida (Testate Lobose Amoebae) Assemblages in a Temperate Lake: Implications for Limnological Studies. *Microbial Ecology*, *76*(3), 680–694. https://doi.org/10.1007/s00248-018-1157-5

Steele, R. E., Reinhardt, E. G., Devos, F., Meacham, S., LeMaillot, C., Gabriel, J. J., Rissolo, D., Vera, C. A., Peros, M. C., Kim, S.-T., Marshall, M., & Zhu, J. (2023). Evidence of recent sea-level rise and the formation of a classic Maya canal system inferred from Boca Paila cave sediments, Sian Ka'an biosphere, Mexico. *Quaternary Science Reviews*, *310*, 108117. https://doi.org/10.1016/j.quascirev.2023.108117

Stéphan, P., Goslin, J., Pailler, Y., Manceau, R., Suanez, S., Van Vliet-Lanoë, B., Hénaff, A., & Delacourt, C. (2015). Holocene salt-marsh sedimentary infilling and relative sea-level changes in West Brittany (France) using foraminifera-based transfer functions. *Boreas*, *44*(1), 153–177. https://doi.org/10.1111/bor.12092

Stewart, H., Bradwell, T., Bullard, J., Davies, S. J., Golledge, N., & McCulloch, R. D. (2017). 8000 years of North Atlantic storminess reconstructed from a Scottish peat record: Implications for Holocene atmospheric circulation patterns in Western Europe. *Journal of Quaternary Science*, *32*(8), 1075–1084. https://doi.org/10.1002/jqs.2983

Svidzinsky, A. A., Scully, M. O., & Herschbach, D. R. (2005). Bohr's 1913 molecular model revisited. *Proceedings of the National Academy of Sciences*, *102*(34), 11985–11988. https://doi.org/10.1073/pnas.0505778102

Tanigawa, K., Sawai, Y., Bobrowsky, P., Huntley, D., Goff, J., Shinozaki, T., & Ito, K. (2022). A new chronology for tsunami deposits prior to the 1700 CE Cascadia earthquake from Vancouver Island, Canada. *Scientific Reports*, *12*(1), Article 1. https://doi.org/10.1038/s41598-022-16842-8

Tjallingii, R., Röhl, U., Kölling, M., & Bickert, T. (2007). Influence of the water content on X-ray fluorescence core-scanning measurements in soft marine sediments: XRF CORE SCANNING. *Geochemistry, Geophysics, Geosystems*, *8*(2), n/a-n/a. https://doi.org/10.1029/2006GC001393

Tseshaht First Nation. (n.d.). *Tseshaht First Nation | Traditional Territory*. Tseshaht First Nation. Retrieved October 31, 2023, from https://tseshaht.com/history-culture/traditional-territory/

Turner, J. N., Holmes, N., Davis, S. R., Leng, M. J., Langdon, C., & Scaife, R. G. (2015). A multiproxy (micro-XRF, pollen, chironomid and stable isotope) lake sediment record for the Lateglacial to Holocene transition from Thomastown Bog, Ireland. *Journal of Quaternary Science*, *30*(6), 514–528. https://doi.org/10.1002/jqs.2796

Unkel, I., Björck, S., & Wohlfarth, B. (2008). Deglacial environmental changes on Isla de los Estados (54.4°S), southeastern Tierra del Fuego. *Quaternary Science Reviews*, *27*(15), 1541–1554. https://doi.org/10.1016/j.quascirev.2008.05.004

Unkel, I., Fernandez, M., Björck, S., Ljung, K., & Wohlfarth, B. (2010). Records of environmental changes during the Holocene from Isla de los Estados (54.4°S), southeastern Tierra del Fuego. *Global and Planetary Change*, *74*(3), 99–113. https://doi.org/10.1016/j.gloplacha.2010.07.003

van de Plassche, O. (1986). *Sea-level research: A manual for the collection and evaluation of data*. Norwich : Geo Books.

Vos, P. C., & de Wolf, H. (1993). Diatoms as a tool for reconstructing sedimentary environments in coastal wetlands; methodological aspects. *Hydrobiologia*, *269*(1), 285–296. https://doi.org/10.1007/BF00028027

Walker, J. S., Cahill, N., Khan, N. S., Shaw, T. A., Barber, D., Miller, K. G., Kopp, R. E., & Horton, B. P. (2020). Incorporating temporal and spatial variability of salt-marsh foraminifera into sea-level reconstructions. *Marine Geology*, *429*, 106293. https://doi.org/10.1016/j.margeo.2020.106293

Walker, J. S., Li, T., Shaw, T. A., Cahill, N., Barber, D. C., Brain, M. J., Kopp, R. E., Switzer, A. D., & Horton, B. P. (2023). A 5000-year record of relative sea-level change in New Jersey, USA. *The Holocene*, *33*(2), 167–180. https://doi.org/10.1177/09596836221131696

Wang, K., He, J., & Davis, E. E. (1997). Transform push, oblique subduction resistance, and intraplate stress of the Juan de Fuca Plate. *Journal of Geophysical Research: Solid Earth*, *102*(B1), 661–674. https://doi.org/10.1029/96JB03114

Wang, P. L., Engelhart, S. E., Wang, K., Hawkes, A. D., Horton, B. P., Nelson, A. R., & Witter, R. C. (2013). Heterogeneous rupture in the great Cascadia earthquake of 1700 inferred from coastal subsidence estimates. *Journal of Geophysical Research: Solid Earth*, *118*(5), 2460–2473. https://doi.org/10.1002/jgrb.50101

Wang, P.-L., Engelhart, S. E., Wang, K., Hawkes, A. D., Horton, B. P., Nelson, A. R., & Witter, R. C. (2013). Heterogeneous rupture in the great Cascadia earthquake of 1700 inferred from coastal subsidence estimates. *Journal of Geophysical Research: Solid Earth*, *118*(5), 2460–2473. https://doi.org/10.1002/jgrb.50101

Watcham, E. P., Shennan, I., & Barlow, N. L. M. (2013). Scale considerations in using diatoms as indicators of sea-level change: Lessons from Alaska. *Journal of Quaternary Science*, *28*(2), 165–179. https://doi.org/10.1002/jqs.2592

Weltje, G. J., Bloemsma, M. R., Tjallingii, R., Heslop, D., Röhl, U., & Croudace, I. W. (2015). Prediction of Geochemical Composition from XRF Core Scanner Data: A New Multivariate Approach Including Automatic Selection of Calibration Samples and Quantification of Uncertainties. In I. W. Croudace & R. G. Rothwell (Eds.), *Micro-XRF Studies of Sediment Cores: Applications of a non-destructive tool for the environmental sciences* (pp. 507–534). Springer Netherlands. https://doi.org/10.1007/978-94-017-9849-5_21

Weltje, G. J., & Tjallingii, R. (2008). Calibration of XRF core scanners for quantitative geochemical logging of sediment cores: Theory and application. *Earth and Planetary Science Letters*, *274*(3–4), 423–438. https://doi.org/10.1016/j.epsl.2008.07.054

Williams, H. F. L., Beaubouef, C. E., Liu, K., Culligan, N., & Riedlinger, L. (2022). Testing XRF identification of marine washover sediment beds in a Coastal Lake in Southeastern Texas, USA. *Marine Geology*, *443*, 106705. https://doi.org/10.1016/j.margeo.2021.106705

Williams, S., Garrett, E., Moss, P., Bartlett, R., & Gehrels, R. (2021). Development of a Training Set of Contemporary Salt-Marsh Foraminifera for Late Holocene Sea-Level Reconstructions in southeastern Australia. *Open Quaternary*, *7*(1), 4. https://doi.org/10.5334/oq.93

Williams, S. L., Garrett, E., Moss, P. T., Dangendorf, S., Hibbert, F. D., Atkinson, N. R., Pashley, V., Millar, I. L., Garnett, M. H., Zawadzki, A., & Gehrels, W. R. (2023). Relative sea-level changes in southeastern Australia during the 19th and 20th centuries. *Journal of Quaternary Science*, *1*(n/a). https://doi.org/10.1002/jqs.3528

Wilson, G. P., Lamb, A. L., Leng, M. J., Gonzalez, S., & Huddart, D. (2005). δ13C and C/N as potential coastal palaeoenvironmental indicators in the Mersey Estuary, UK. *Quaternary Science Reviews*, *24*(18), 2015–2029. https://doi.org/10.1016/j.quascirev.2004.11.014

Witter, R. C., Kelsey, H. M., & Hemphill-Haley, E. (2003). Great Cascadia earthquakes and tsunamis of the past 6700 years, Coquille River estuary, southern coastal Oregon. *GSA Bulletin*, *115*(10), 1289–1306. https://doi.org/10.1130/B25189.1

Woodroffe, S. A. (2009). Recognising subtidal foraminiferal assemblages: Implications for quantitative sea-level reconstructions using a foraminifera-based transfer function. *Journal of Quaternary Science*, *24*(3), 215–223. https://doi.org/10.1002/jqs.1230

Woodroffe, S. A., & Long, A. J. (2010). Reconstructing recent relative sea-level changes in West Greenland: Local diatom-based transfer functions are superior to regional models. *Quaternary International*, *221*(1), 91–103. https://doi.org/10.1016/j.quaint.2009.06.005

Woodward, C. A., & Gadd, P. S. (2019). The potential power and pitfalls of using the X-ray fluorescence molybdenum incoherent: Coherent scattering ratio as a proxy for sediment organic content. *Quaternary International*, *514*, 30–43. https://doi.org/10.1016/j.quaint.2018.11.031

Ziegler, M., Jilbert, T., de Lange, G. J., Lourens, L. J., & Reichart, G.-J. (2008). Bromine counts from XRF scanning as an estimate of the marine organic carbon content of sediment cores. *Geochemistry, Geophysics, Geosystems*, *9*(5). https://doi.org/10.1029/2007GC001932

Zong, Y., & Horton, B. P. (1998). Diatom Zones Across Intertidal Flats and Coastal Saltmarshes in Britain. *Diatom Research*, *13*(2), 375–394. https://doi.org/10.1080/0269249X.1998.9705456

Zong, Y., & Horton, B. P. (1999). Diatom-based tidal-level transfer functions as an aid in reconstructing Quaternary history of sea-level movements in the UK. *Journal of Quaternary Science*, *14*(2), 153–167. https://doi.org/10.1002/(SICI)1099-1417(199903)14:2<153::AID-JQS425>3.0.CO;2-6

Zong, Y., Shennan, I., Combellick, R. A., Hamilton, S. L., & Rutherford, M. M. (2003). Microfossil evidence for land movements associated with the AD 1964 Alaska earthquake. *The Holocene*, *13*(1), 7–20. https://doi.org/10.1191/0959683603hl590rp

Appendix A. Supplemental files for Chapter 3

The accompanying spreadsheet (A.Giang_XRF_e.csv) shows the raw data collected from the ITRAX XRF Core Scanner for all ten transects. There are eighty XRF measurements associated with each station sample. The spreadsheet includes the following columns:

Transect, Station, Zone, position..mm., sample.surface, validity, cps, MSE, Al, Si, P, S, Cl, Ar, K, Ca, Ti, Cr, Mn, Fe, Co, Ni, Cu, Zn, As, Br, Rb, Sr, Y, Zr, Pb, Mo.inc, Mo.coh, Dt.

Filename: A.Giang_XRF_e.csv

The accompanying spreadsheet (A.Giang_XRF_m.csv) shows the summarized dataset that was used for all statistical analyses and figures in Chapter 3. This dataset only considers elements relevant for analysis with their values averaged for each station sample. Environmental data corresponding to each station sample is appended to the geochemical data. The spreadsheet includes the following columns:

Transect, Station, Zone, Distance, MTL, SWLI, LOI, Si, S, Cl, K, Ca, Ti, Mn, Fe, Br, Sr, ICR.

Filename: A.Giang_XRF_m.csv

The accompanying R Markdown file (A.Giang_MSc_RCode.Rmd) shows the R code used to summarize the raw elemental data (A.Giang_XRF_e.csv) to generate the summarized dataset (A.Giang_XRF_m.csv) and subsequently to analyze the elemental data and generate all statistical figures.

Filename: A.Giang_MSc_RCode.Rmd